UNIVERSITÀ
DEGLI STUDI
FIRENZE

DOTTORATO DI RICERCA IN SCIENZE DELLA TERRA

CICLO XXIX

COORDINATORE Prof. LORENZO ROOK

Analisi Integrata dei parametri geofisici registrati a Stromboli durante le fasi di instabilità eruttiva ed eventi anomali

---

Integrated geophysical analysis during phases of eruptive activity at Stromboli volcano

Settore Scientifico Disciplinare GEO/11

Dottorando
Dott. *Genco Riccardo*

Tutore
Prof. *Maurizio Ripepe*

Coordinatore
Prof. Lorenzo Rook

Anni 2013/2016

To the technicians.
Because research
is written by scientists,
but crafted by them.

To my parents and sons.
They don't mind what I do,
but they love who I am.

Riassunto Il presente lavoro si pone come obiettivo lo studio delle dinamiche di condotto, superficiali e sub-superficiali, associate all'attivitá Stromboliana, con particolare riguardo alle fasi di attivitá, esplosiva e effusiva, considerate "anomale" (crisi effusive, trabocchi, parossismi ed esplosioni maggiori). Queste infatti sono caratterizzate dalla rapida evoluzione dei parametri geofisici monitorati, e rappresentano pertanto un momento ideale per la comprensione delle dinamiche del sistema superficiale. La rete di monitoraggio geofisico integrato (sismico, infrasonico, termico e clinometrico), installata a Stromboli da oltre tredici anni, fornisce un dataset oltremodo completo, che include 3 crisi effusive, 2 parossismi, 33 esplosioni maggiori e oltre 40 trabocchi. Inoltre l'utilizzo di telecamere ad alta velocitá e di tecniche di interferometria radar, durante campagne di misura apposite, ha permesso di arricchire il data-set con misure inedite del campo di deformazione e della propagazione delle onde acustiche nelle immediate vicinanze dei crateri attivi. I parametri relativi alle dinamiche superficiali di rilascio di gas (pressioni infrasoniche e immagini termiche) sono stati messi in relazione con quelli che indagano i processi interni (deformazioni del suolo e tremore sismico), allo scopo di seguire i cambiamenti di pressione del sistema in consequenza dei processi di vescicolazione, segregazione e risalita del gas nelle porzioni superficiali del condotto. I risultati ottenuti indicano che, il rilascio di gas in sovrappressione durante eventi parossistici e maggiori, é preceduto da una fase, della durata di oltre 500 secondi, di iflazione del condotto. Entrambe i fenomeni, maggiori e parossismi, condividono lo stesso andamento deformativo, suggerendo quindi una dinamica comune, probabilmente legata alla rapida risalita nel sistema superficiale di una piccola quantitá di magma ricco in gas. Per quanto riguarda l'attivitá effusiva, i parametri geofisici mostrano che gli eventi di trabocco sono associati ad un'attivitá di degassamento sostenuto e spattering, evidenziando ruolo chiave dei processi di degassamento nella generazione di tali episodi. Al contrario, le crisi effusive sono legate allo svuotamento del systema superficiale in seguito all'apertura di una bocca laterale. I risultati ottenuti evidenziano la capacitá dell'analisi geofisica integrata nello studio dei processi che governano l'attivitá Stromboliana.

Abstract In this work, conduit dynamics of Strombolian activity are studied, from surface to sub-surface processes. Special attention is addressed to anomalous explosive and effusive activity, namely paroxysmal and major explosions, effusive crises and overflow episodes. These are in fact characterized by a rapid evolution of the geophysical parameters, thus representing privileged periods to understand the shallow system dynamics. The thirteen-years-long records from the integrated geophysical network (i.e., seismic, infrasonic, thermal and ground deformation data), permanently operated at Stromboli, provides an exceptional data set which includes 3 effusive crises, 2 paroxysms, 34 major explosions and over 40 overflows. In addition, temporary experiments using high-speed imagery and radar interferometry were specifically designed to provide unprecedented imaging of crater deformation and acoustic waves propagation during explosive activity. The parameters related with the surface gas release dynamics (i.e., infrasound pressures and thermal images) are compared with those investigating the sub-surface processes (i.e., ground deformation and seismic tremor), thus tracking the changes of system pressure conditions controlled by vesiculation, segregation and migration of gas into the shallow magmatic system. The results indicate that over-pressured gas release accompanying the paroxysmal and major explosive events, is preceded by a 500-seconds-long phase of pressure growth inside the conduit. Both events share the same ground deformation pattern, suggesting common source dynamics, likely related to the fast rise of gas-rich magma batches into the shallow conduit. Concerning effusive activity, geophysical data-set shows that the overflow episodes are associated to sustained degassing and spattering activity, revealing the driving role of magma degassing processes. On the contrary, major effusive crises can be interpreted as the gravity-driven drainage of the shallow magmatic system following the opening of a lateral vent. The results obtained in this study, highlight the capability of the integrated geophysical approach to shed a light on the processes driving the Strombolian activity.

Contents

Chapter 1

Introduction

1.1 Introduction

The investigation of the explosive dynamics represents one of the most exciting and fascinating field of study of modern volcanology. Volcanic explosions, often considered as stochastic and unpredictable events, rather represent the obvious result of the exsolution, storage and release of gas from the shallower portion of the magmatic system. The sudden ejection of gas and tephra on the surface is in fact preceded and accompanied by a series of phenomena which can be observed and recorded using the proper techniques.
This work attempts to study the interactions between surface and sub-surface processes by a geophysical approach, with the aim of characterizing the conduit dynamics involved in Strombolian explosivity. A particular focus is directed to the short-term variations (minutes-hours-days) of explosive parameters during the phases of "instability" of the system, such as paroxysmal events, major explosions and effusive phases. This goal is particularly effective in the risk assessment and mitigation procedures regarding volcanic explosive activity.
In this framework, the geophysical data-set collected during the last decade on Stromboli Volcano from the integrated geophysical network of the Laboratorio di Geofisica Sperimentale (LGS) of the Dip. of Earth Sciences of The University of Firenze have been carefully analyzed with particular emphasis on the "anomalous" phases and events occurred during the typically steady Strombolian activity. Those are in fact characterized by a rapid evolution of monitored parameters, thus representing privileged periods for the investigation and understanding of the shallow system dynamics. In detail, the on-surface parameters (infrasound pressures and thermal images), strictly related with the gas release dynamics, are compared and linked with those referring to sub-surface processes (ground deformation and seismic tremor) revealing the changes of system pressure acted by vesiculation, segregation and accumulation of gas into the shallow magmatic system.

The processes of gas vesiculation, segregation and release represent one of the most studied volcanic topics. Gas exsolution represents the driving force of volcanic explosive activity. Prodigious Plinian eruption, able to sustain a few tens of kilometers high eruptive column, violent Hawaiian lava fountains, projecting magma for hundreds of meters, and mild Strombolian activity, are all sharing a common process called *magmatic fragmentation* [105]. The fragmentation process is responsible for the transition of magma from a multiphase fluid, containing gas bubbles and solid crystals to a gaseous fluid with dispersed drops of liquid and solid fragments [18]. The gas exsolution, accompanying the magma rise from the deeper part of the magmatic system to the shallower part strongly affects its rheology, thence the dynamic behavior of the shallower portion of the magmatic conduit and ultimately the eruptive style as well as the large majority of phenomena observed and measured on surface.
A primary contribution to the understanding of those processes acting on this shallow zone arises from the geophysical techniques, such as seismic analysis [121], thermal imagery [43] and Infrasound [51]. However these techniques are relatively young and often data-set are incomplete and, apart from a few cases, not able to cover long time series. Moreover, the unstable behavior of several active volcanoes, often alternating long quiescent phases to discrete, short-lasting, intense eruptive crises,

represents a further obstacle to the collection of representative data-sets for explosive volcanism.
Under this point of view, the open-conduit volcanoes, with their persistent degassing activity from the eruptive vents, represent a privileged setting for the investigation of degassing processes and conduit dynamics. Amongst those, Stromboli volcano has largely become the most studied. The Strombolian activity is characterized by mild discrete explosions occurring with a rate of a few events per hour and superimposed to continuous over pressured degassing (puffing). This ordinary activity is seldom interrupted by effusive phases and paroxysms and punctuated by sporadic large explosive events named "major explosions" [6].
During the last decade, the multidisciplinary integration of geophysical data [45] allowed a robust investigation of the shallow system of the Stromboli volcano. The collected seismic, infrasonic and thermal data concurred to suggest an extremely shallow position for the source of the explosive events (e.g. [90, 23, 61, 92, 30]). Also the ground deformation analysis contributed to highlight the key role of the shallow conduit to the explosive dynamic. The obtained results indicate that the release of over-pressured gas accompanying the explosive events, is preceded by a phase of pressure growth inside the conduit [38] thus implying a mechanism of gas/magma storage into the shallow portion of the magmatic system.
The capability of the integrated geophysical approach, able to casting the light on the processes that take place into the shallow magmatic system and drive the Strombolian activity, are even more evident when considering these phases of transition from regular to effusive activity [93]. Rapid changes of the monitored parameters are observed. The study of these "anomalies" represents a key topic for the research and a condition for the use of the geophysical parameters to monitoring the explosive volcanic activity.

1.2 Anomalous phases and events recorded during Strombolian activity

Stromboli volcano has been characterized by open-vent conditions, as reported since the 7th century A.D. [104]. In such an open-conduit condition, the gas is released by passive degassing [12], mild explosive activity [45] and lava effusions.
The explosive activity is controlled by the balance between magma supply, outgassing and eruptive rates, mainly characterized by low-intensity, regular Strombolian explosions [86]. However more violent explosive eruptions may suddenly occur with not obvious evidences of any precursors. These events are named "Major explosions" or "Paroxysms", depending on their intensity [6].
The persistent Strombolian activity is sometime interrupted or accompanied by periods of effusive activity. Major effusive crises, lasting several weeks to months, with total effusive volumes in the order of millions of cubic meters and and small, short-living overflow episodes with much smaller volumes involved are distinguished. Effusive crises occur every 5-15 years [6] while there is no clear statistic about overflows. The exact (or at least reasonably exact!) definition for these particular phases or events is left unsolved here, as will be treated in details in the proper chapters, along

with a detailed description and analysis.
During the thirteen-years-long period between 2003 and 2015, when the *LGS* integrated geophysical network was continuously operated, 3 main eruptive crises, 2 paroxysms, 44 minor overflow events, and more than 33 major explosions were recorded (Fig. 1.1).

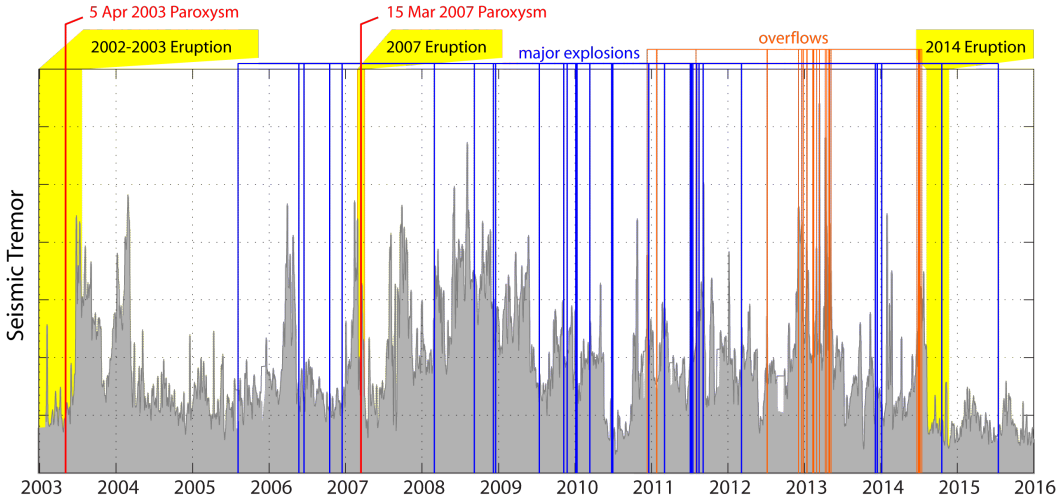

Figure 1.1: Thirteen-years-long (2003 -2015) seismic tremor amplitude time series (gray). Effusive crises are highlighted with yellow patches, paroxysms, major explosions and overflow episodes are marked with vertical lines colored in red, blue and orange, respectively.

1.3 Aims of the thesis

The purpose of this thesis is to study, with an integrated geophysical approach, the dynamic processes driving the Strombolian activity during its effusive phases or single violent explosive events.
The rich data-set introduced in the last section is used as the starting point for this project. These peculiar phases of activity, commonly considered as "anomalous" respect to the most typical Strombolian activity, are characterized by relevant and abrupt changes of the monitored parameters. These evident variations are suggesting a rapid evolution of the shallow conduit dynamics to adapt to the rapidly changing flow conditions. The idea at the base of this PhD project was to compare the geophysical parameters relative to the external dynamics, occurring at the magma/surface interface, such as infrasound data ant thermal imagery, with those providing information on the processes acting in the shallow est portion of the conduit, namely seismic signals and ground deformations. This integration allowed to depict a clear image of the phenomena and their source dynamics indicating that the, so called "anomalous" events may provide an interpretative key to disclose, an finally understand the shallow conduit dynamics responsible for the Strombolian activity.

1.4 Thesis overview

During the last decades, geophysical methodologies proved to be able to cast the light on the processes which take place into the shallow magmatic system and drive the Strombolian activity. In **Chapter 2** the geophysical parameters used to monitor volcanic explosive and effusive activity at Stromboli volcano (and worldwide) are introduced. The Integrated Geophysical Network, permanently operated by the Laboratorio di Geofisica Sperimentale (LGS) of the Department of Earth Sciences of the University of Firenze is presented. This monitoring network provided, during the last twelve years, a dense, multiparametric geophysical data-set. This resource was searched to individuate and extract the main events defined as "anomalous" with respect to the regular Strombolian mild explosive activity. Paroxysms, Major explosions, lava flows and overflows belong to this category, whit the aim of studying the short-term variation of eruptive activity.
Amongst the numerous parameters and techniques useful to investigate volcanic phenomena, seismic tremor, infrasound array analysis, ground deformations and thermal imagery are introduced and discussed. The knowledge and understanding of instruments and techniques is vital to correctly processing and interpreting the geophysical data, and is a key part of the toolbox of every geophysicist.
In due awareness two experiments conducted on Stromboli volcano are presented in **Chapter 3** as "case studies". Although apparently completely different, both share te same wish of observe volcanic processes "as closely as possible". The first experiment, consists in the use of an high-speed, high-resolution camera to investigate the source of infrasound signals. The developed methodology allows to use every pixel of the image as a virtual pressure sensor. Using this technique, the infrasonic pressure wave-field around the exploding vent, was reconstructed. The obtained data suggested a possible super-sonic dynamic during violent Strombolian activity. Results of this experiment has been already published in *Geophysical Research Letters* in 2014.
The second experiment, still unpublished, involves the use of a ground-based interferometric radar to measure the deformation field in the close proximity of the active vents. The radar was temporary installed on the volcano and used to "observe" the ordinary explosive activity. Collected data revealed a significant ground displacement at the crater, consistent with the dilatation of the vent a few seconds before the explosion, followed by a contraction during the ejection phase.
The radar-derived ground deformations have been compared with tilt, seismic and thermal data provided by the Integrated Geophysical Network. Results seems to suggest a very shallow source position for VLP events, in contrast with the commonly accepted model. In **Chapter 4** the Strombolian explosive activity is explored. A phenomenological description of Paroxysmal and major events is followed by an exhaustive geophysical characterization and a proposal of classification. The peculiarities of the single Major events are first presented, discussed and finally reduced to a common pattern of ground deformations.
A similar approach is used for Paroxysms. The main limit of our tilt data-set, confined to a single event (Mar. 15, 2007), is overcame by the use of seismic-derived tilt data, which allow to extend retrieve reliable ground deformation data for to the Apr. 5 2003 paroxysm. Despite the different magnitude, both paroxysmal and major

explosions are proved to share the same pattern of about 500 seconds long inflation phase preceding the explosive onset. This signal is interpreted as the evidence of a common dynamic process. This conclusion is also supported by petrographical evidences, which highlight the importance of fast-rising, gas-rich LP magma batches as the driving force of extraordinarily violent Strombolian explosive events.
The effusive activity recorded at Stromboli between 2003 and 2015 is described and analyzed in **Chapter 5**. Three major effusive crises, consisting in long-lasting lava flow from newly opened lateral vents, and characterized by intense variations of geophysical parameters, have occurred in the past 12 years. The different chronological evolution of these phenomena does not hide the common mechanism driving those effusive events. The Gravity-Driven model, recently proposed by *Ripepe et al.*, 2015, (R.G. is listed as co-author), is presented and the implications are discussed. The model succeeded in explaining all the geophysical observations and provide a key to interpret these effusive crises as the result of passive drainage process. In this picture, a deep magma input is not required to explain the effusion although it possibly plays a role in the opening of a new, lower, vent on the *Sciara del Fuoco*. Further in the chapter also minor effusive events (overflows) are considered. For these events a sort of "geophysical signature" is delineated on the base of the integration of all the available parameters. Differently from major effusive crises, the short-lived overflow episodes appear as "active" phenomena. The sustained magma degassing recorded by infrasound array and the continuous spattering from the active crater observed from thermal imagery, indicate that gas exsolution and release at the surface is the driving force of the overflow activity.
For each treated argument, results are discussed in an apposite section along with relative conclusions. In **Chapter 6** all the single argument conclusions are summarized together as final remarks of this PhD project.

The results presented here are the outcome of the work done by R.G. during his PhD project. However, the large contribution from all members of *LGS* group cannot be neglected. The collection of a 13-years-long, valuable and rather unique geophysical data-set for Strombolian activity is in fact the product of the continuous, yet indefatigable, work of several PhD students, research-fellows and PostDocs, bravely captained by M. Ripepe. No data would have been collected, nor analysis carried out, without the (also physical) efforts spent by the whole group. Amongst the thousands lines of code, appositely written to process the data presented in the following chapters, a relevant part is inherited from the dedication of the ones who preceded and accompanied me.

Chapter 2

Instruments and Methods

2.1 The Integrated Geophysical Network at Stromboli

The permanent, integrated geophysical monitoring network deployed and continuously operated by the Laboratorio di Geofisica Sperimentale (*LGS*) of the University of Firenze (UniFi) commenced in January 2003 and it has been in continuous expansion ever since ([98, 95, 97, 93]). As shown in Fig. 2.1, it consists of 4 seismo-acoustic stations located in the upper part of the volcanic edifice (STR, SCI, ROC, PZZ), each equipped with a three-component broad-band seismic sensor (Guralp CMG-40T) and an infrasonic pressure sensor (ITEM Prs-1) with a sensitivity range of 0.01-300 Hz and a sampling rate of 100 Hz. An infrasound array (EAR), composed of 5 pressure sensors in a L-shaped configuration with an internal spacing of 100 m, operates at a distance of ∼450 m from the active craters in order to track the source position of excess pressure gas release. Two thermal IR cameras (FLIR A20) are installed at 750 m a.s.l. (ROC) and 190 m a.s.l. (GST) to monitoring both the summit craters and the *Sciara del fuoco* slope, respectively, with a sampling rate of 1 sps. Three borehole tiltmeters (OHO, LSC and LFS) are installed around the crater area, each at about 5 m depth, to record the inflation or deflation of the edifice with a sampling rate of 1 sps. In front of the westernmost corner of the *Sciara del fuoco*, an ondametric gauge (PDC) is installed to monitor possible tsunami waves produced by large landslide events which might occur on the *Sciara* slope. In addition, thermal imagery using remote sensing from a MODIS (Moderate Resolution Imaging Spectroradiometer) sensor is performed in collaboration with the University of Torino (UniTo) [27]. All data are continuously recorded and transmitted in real-time via radio-link to the monitoring center (COA), operated on Stromboli island by the Dipartimento di Protezione Civile. The data are then collected, processed and published in real-time on the web (*http://lgs.geo.unifi.it/Stromboli/str.php*).

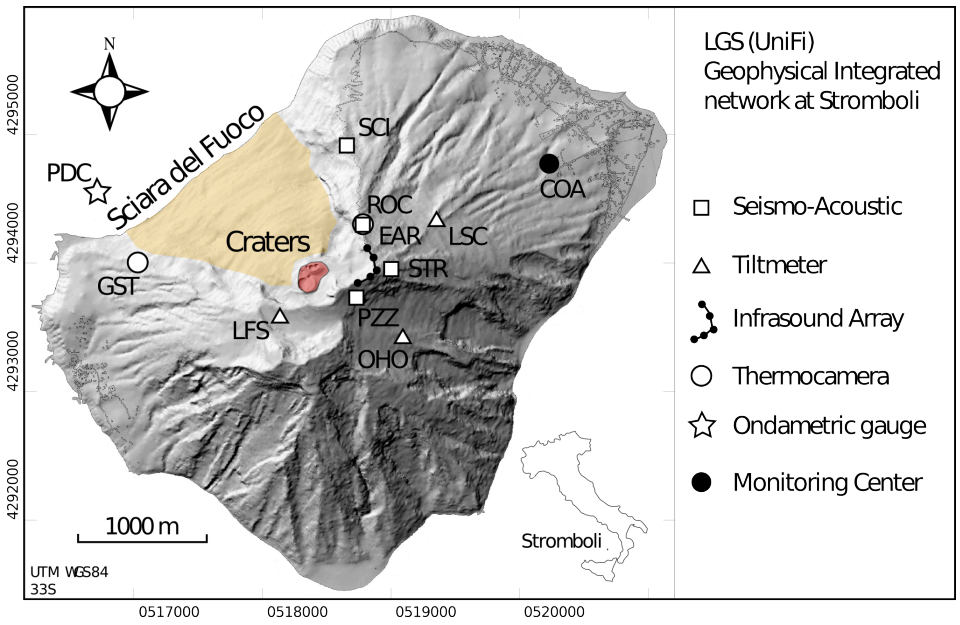

Figure 2.1: Map of Stromboli island with position of the station of the Geophysical Integrated Network operated by the Laboratorio di Geofisica Sperimentale (*LGS - UniFi*)

2.2 Monitored geophysical parameters

The real-time acquisition and processing of the geophysical parameters allows to provide a relevant amount of information on the eruptive activity of the volcano and its intensity. As a consequence, the evolution of these parameters can be perceived tracking the transitions from explosive to effusive and vice-versa [111, 98, 93]. The main geophysical parameters analyzed to monitor the volcanic activity are the following:

- ***Seismic tremor***. The amplitude of seismic tremor at Stromboli is one of the key parameters used to define the level of the volcanic activity. It is calculated as the root-mean-squared-amplitude (RMSA) of the velocity traces, band-pass filtered in the 0.9-8 Hz frequency band. At Stromboli, it is strongly related to the over-pressured degassing activity of the magmatic system (puffing), suggesting that it could result from the elastic response of the magma column to the continuous gas bubble coalescence, rise and burst [94]. The ten year long records of this parameter led to the definition of four different threshold levels for tremor amplitude: low ($< 1\times10^{-6}m/s$), medium (1×10^{-6} to $4\times10^{-6}m/s$), high (4×10^{-6} to $8 \times 10^{-6}m/s$), and very-high ($> 8 \times 10^{-6}m/s$). It has been observed that before paroxysms, effusive crises or other relevant changes that destabilize Stromboli's ordinary activity, the tremor amplitudes increase to high or very-high levels [98], suggesting therefore an increase in the gas flux.

- ***Seismic displacement in the VLP (Very-long-period) band***. Explosions at Stromboli produce low frequency signals followed by a higher frequency phase. Although the source mechanism is still a matter of debate, it is generally accepted that the low frequency component is related to the rise of a gas slug within the magma column, whereas the high frequency component is related to the bursting of the slug at the free-surface (e.g. [72, 90, 23, 45]). The rate and the amplitude of VLP provide information on the intensity of the explosive activity of the volcano. Over the years, the following thresholds have been established to describe the rate of VLP: low ($<$ 5 events/hour), medium (5-12 events/hour), high (12-20 events/hour), and very-high ($>$20 events/hour). In addition the source position of the VLP can be determined from the analysis of the polarization of their waveforms [61]. The dip angle is calculated as the angle between the horizontal plane and the wave propagation direction. The source depth of VLP signals during the regular activity is remarkably stable and located at $\sim$220-300 m beneath the active vents [23]; [61]. Following periods of effusive activity however, the source depth increases, as observed in 2003, 2007 and 2014 [91, 111].

- ***Infrasound activity***. Infrasound waves are generated by volcanic activity from excess pressure release of gas into the atmosphere, evidencing overpressure condition of the gas in the magma column [112, 88]. At Stromboli, the infrasonic activity is characterized by two distinct permanent features: (a) discrete energetic transients associated with Strombolian explosions; (b) low-amplitude pulses, repeating at interval of 1-2 seconds, and associated with persistent active degassing (puffing) [96]. The rate and the amplitude of this

infrasonic activity is fundamental for monitoring purposes as a proxy to measure the state of pressurization of the volcanic system. Moreover, tracking the source location of those two signals provides information on how and where the system is evacuating this over-pressured gas. Several years of infrasound monitoring have showed that puffing is predominantly originated from the Central crater, with pressures typically <0.5 bar, while explosions are mainly concentrated at the SW and NE craters, with pressures ranging from 1 to >3 bar.

- ***Ground deformation***. During the phases of regular explosive activity, Inflation/Deflation cycles are recorded by the tiltmeters in relation to each explosion produced at the craters. These very small amplitude ($< 0.1\mu rad$)tilt changes, with a duration of a few tens of seconds are thought to be associated with the process of gas recharge (i.e inflation) and discharge (i.e. deflation) within the magma conduit [38]. Nonetheless, deflation events of larger amplitude and duration (i.e. from $0.1\mu rad$ to $15\mu rad$), lasting hours to days, are concomitants with the emission of large volumes of magma such as during effusive phases, either from the summit craters or from newly open vents [60, 91, 111].

- ***Thermal activity***. Ground-based thermal monitoring is achieved from termal cameras and radiometers, which enable close imaging of volcanic emissions at high frame rate and high spatial resolution. Processing of the data allows to retrieve exit velocities and bulk solid emission volumes in real-time [30]. In addition, it allows tracking the long-term crater-terrace growth and collapse, as well as the activity source region [91]. Satellite-based thermal monitoring, on the other hand, is achieved from the MODIS sensor onboard the *Terra/Acqua* satellites. It has a low spatial and temporal resolution (2 images per day with 1 km resolution). The automated processing of images is performed in near-real-time by MIROVA (Middle InfraRed Observation of Volcanic Activity: http://www.mirovaweb.it), a system dedicated to volcanic hot-spot detection and monitoring, which is developed by the University of Torino in collaboration with *LGS*. *Volcanic Radiative Power* is calculated using MIR method [118] and used to measure the intensity of volcanic thermal emissions. Typically, the ordinary Strombolian activity is characterized by low thermal emissions, whereas very-high emissions are recorded during periods of overflow or lava effusion.

Integrated together, these geophysical parameters provide an exceptional set of information to understand and characterize the internal dynamics and eruptive behavior of the volcano. The provided data are interpreted and synthesized as daily reports, which are delivered to the Italian Civil Protection and contribute to the risk level assessment of the Stromboli volcano.

2.3 Instruments and data processing

The parameters mentioned in the preceding section are obtained from processing of a great amount of data. Most of them are obtained by the specifically written Matlab

code developed at the LGS during the last ten years. A complete discussion of these procedures will be verbose and not inherent to the presented work, so that will here be only briefly introduced and limited to the data-sets and techniques which are used to process the data presented in the following chapters. A particular emphasis will be tributed to the ground tilt, due to its primary role in the following chapters. More specific methodologies will be introduced when needed to explain particular data-sets or elaborations.

2.3.1 Seismo-Acoustic stations

Four seismo-acoustic stations are installed at an elevation $>$ 400 m a.s.l., up to the summit area of the edifice. Each station is equipped with a three component Guralp GMT-40 broad-band seismic sensor with a corner frequency of 0.033 or 0.025 and an infrasound pressure sensor. Since 2014, the data are acquired by a Guralp CMG-DM24 digitizer at 100 Hz with the timing adjusted by GPS. Earlier the data were converted by a properly designed 16bit A/D converter and then streamed to the COA recording center. There were acquired and stored by an appositely written recording software. Relative timing of the data-set was hence guaranteed by synchronous co-registration of all the stations on the same machine while absolute timing was achieved using NTP network server. For this reason the comparison of different data-sets can be tricky when highly precise and reliable timing is required. Seismic signal recorded at Stromboli is characterized by 10-20 s lasting transients that outcrop from the noise. The associated spectrum shows a broad frequency content between 0.03 to 8 Hz.

2.3.2 Clinometric stations

Ground tilt is defined as the spatial derivative of vertical ground displacement, and can be produced by several different natural (or even human) sources, with periods spanning from DC to several hundreds of Hz. For modern volcanology, ground deformation represents one of the main indicators of pressure changes in the magmatic systems and its measure and modeling is used to discriminate deep or shallow sources as well as to determine their shape and volume/pressure changes [32]. Among the numerous techniques available for ground deformation measure, clinometers represent one of the oldest but yet more used instruments. Clinometers are specifically designed to measure variations of the ground tilt angle [1]. Modern instruments are mainly based on bubble sensors, which are, roughly speaking, the high precision version of a carpenter bubble [22]. A modern tiltmeter based on this kind of sensors allows to record ground deformation with amplitudes in the order of nanoradiants. This means that, considering a completely rigid, 1000 km long horizontal board, a sensor placed on one side of it will be able to detect the inclination produced by the lowering of 1 mm of the other side of the board.
The clinometric network installed at Stromboli was deployed between October 2004 and August 2008. Three borehole Pinnacle series T5000 tiltmeters were installed at a depth of $\sim$5 meters at *Liscione* (LSC), *Rina Grande* (OHO), and *La Fossetta* (LFS) sites. The three sites were chosen to achieve the best coverage on the tilt source, assumed to be coincident with the crater area or below it, as suggested by the results of previous campaigns from *Wielandt and Forbriger, 1999* and *Kirchdörfer, 1999*

[115, 54]. Pinnacle T5000 tiltmeters are equipped with two high-precision bubble-based clinometric sensors, perpendicularly mounted on a self-leveling platform. This allow to measure two dimensional variations of tilt angle with a nominal resolution of 1 nanometer and up to a maximum of several thousands of microradiants. The borehole installation allows to partially remove the effects of temperature and atmospheric pressure changes. Moreover the instrument is equipped with an embedded temperature sensor which provides accurate record of temperature changes around and inside the instrument. Due to this setup and the high sensitivity, these instruments are able to record earth-tide oscillations with amplitudes of a few hundreds of nanoradiants, as well as the tiny transients related to the ordinary explosive activity, with amplitude up to $\sim$0.2 microradians [38]. Tilt data are collected at 1 Hz. Due to their setup and position, OHO and LFS stations seem to better record the transients related to the regular Strombolian activity. OHO station was installed almost three years before LFS, so that its record is significantly longer. For this reason OHO tiltmeter will be used as reference station for amplitude computations in the next chapters. Because of their broad frequency content (from DC to nyquist frequency), and due to the wide range of phenomena that can be recorded, the automatic analysis of tilt data is rather difficult and limited to the detection of "well known" signals (or easily recognizable for their characteristic shape and parametrized). Nonetheless, an automatic Early-Warning system for paroxysmal events has been designed and implemented. The analysis of tilt data is mostly done manually using an appositely written Matlab code able to perform common procedures such as band-pass filtering, trend removal, running average etc. Particular analysis will be introduced and discussed in detail on the occurrence, if needed. Nonetheless, in the following paragraph, a discussion on the retrieval of tilt signals from seismic records will be briefly introduced, as it represents a non-conventional procedure allowing to expand the clinometric network over its formal extension.

2.3.2.1 Displacement from tiltmeter and tilt from seismometers

Due to their particular sensor design, tiltmeters are able (or rather forced!) to record ground displacement as well as real tilt [101]. However, the pendulum-based seismic sensors are also sensitive to both ground accelerations and tilts [70]. Such as the case of the common broad-band seismometers. While this behavior prevents from clearly discriminate tilt from displacement, and thus leading to possible misunderstandings, on the other hand it allows to compare the records of both instruments on the overlapping frequency band and, more interestingly, to retrieve tilt from seismic records [114, 5, 38]. This procedure has been successfully applied to ordinary Strombolian activity by *Genco and Ripepe (2010)* [38], demonstrating the possibility of recovering reliable tilt signal from seismic station of the LGS permanent network. The full theory and technical procedure followed to extract tilt signal from broad-band seismometers is described exhaustively in appendix 1.

2.3.3 Infrasound array

Since 2003, a permanent infrasound array constituted by 5 differential pressure sensors (ITEM PRS) deployed in an L-shaped configuration with an internal spacing of 100 m is installed on the summit of Stromboli volcano [100], at a distance of $\sim$ 400

m from the active vents. The array allow to i) obtain the best azimuthal coverage of the active vents, ii) record coherent infrasound waves in the 0.01 - 20 Hz frequency band, and iii) discriminate infrasonic onsets of explosive events. The 5 sensors are connected to the central acquisition system by optical fiber cable. Due to the 400 m array aperture, which is comparable with the distance from the source, the assumption of planar front for waves propagating across the array is not valid. So an automatic detection of coherent infrasound signals in spherical front conditions is obtained using an appositely written algorithm [97]. The algorithm is based on a grid search procedure that, with the minimum computing time, allows the highest resolution and the best coverage of the whole crater terrace. The system provides reliable source localization for both, the continuous puffing activity and the explosive events.

2.3.3.1 Infrasonic analysis of explosive activity

Explosive activity at Stromboli is generally explained as large gas slug that, reaching the uppermost portion of the conduit, explode when the internal pressure is not anymore compensated by the external pressure. This burst generates two different clusters of infrasonic transients [88, 113], reflecting the two end-members of the explosive activity [99], [96]. The first group is represented by either short infrasound pulses (2-5 s) of high amplitude (up to 2 bar at 10 m from the source) that are commonly recorded during explosions or long-lasting (10-20 s) small amplitude ($<$1 bar at 10 m from the source) transients that are produced by sustained gas and ash emissions [96]. The second cluster is characterized by intermittent infrasound pulses associated to the bursting of small gas pockets at the magma surface. This intermittent gas discharge generates small infrasonic pulses ($<$0.1 bar) [94] and occurs regularly every 1-2 seconds, reflecting a sustained, stationary process called puffing. The distribution of mean daily amplitude of puffing during the 2003-2006 interval, show a mean value of $\sim 2.2 \pm 1.2$ Pa, which can be assumed as the typical amplitude during the mild Strombolian degassing activity [110].Such a persistent degassing activity, related to a persistent over-pressurized bubbly flow regime, is thought to be responsible for $\sim$ 45% of the total gas budget of Stromboli volcano [45]. On volcanoes like Stromboli, where several vents can be active at the same time, showing different styles of activity, monitoring the back-azimuth direction of infrasound is a powerful tool to track and visualize changes of activity in the crater area [97]. Infrasound localization indicates that the puffing process is commonly active in one vent at once. Puffing is stable in a single vent over hours-to-days periods, and it can shift from vent to vent, with either smooth or abrupt transition. A behavior suggesting that the over-pressured gas bubble flow tends to follow a preferential segment of the feeding conduit at once. This gas-flow character seems to be consistent with experimental and numerical studies about the partitioning of particles and drops in pipe bifurcations, that usually follow the trajectories coinciding with the highest gas flux [93]. More recent studies have investigated changes in magma vesicularity [21] and glass composition of scorias [57] showing that active degassing can be considered as representative of the pressure perturbation regime inside the shallow conduit system.

2.3.4 Thermal cameras and Infrared thermometer

While infrasound is directly related to the emission of over-pressurized gas, and thus solely reflects the plume emission, both plume emission and ascent can be detected thermally. Hence the two data-sets together provide a complete description of the plume dynamics [63]. Since 2005, at Stromboli, a thermal camera (FLIR A-20) was installed at ROC site, in front of the NE crater. Images are collected at 4 Hz frequency. Placed on the NE flank of the volcanic edifice, on the rim of the *Sciara del Fuoco*, the camera allows to fully visualize the thermal activity of the NE and Central craters and partially the SW crater. Following *Thermal decomposition Image Processing* method developed by Delle Donne and Ripepe (2012) [30], it is possible to retrieve information on height (h), velocity (U) and volume (V). The thermal image analysis leads distinguishing a gas-thrust phase from a buoyancy phase. The former being dominant during the early stage of the explosive event, when over-pressurized gas is released and drives the cloud rapidly upwards, the latter where velocity decelerates to constant buoyant velocity, resulting in a slower convective motion of hot gas and mixture [117], [30]. Besides, the thermal cameras also provide the timing and qualitative observation of the effusive events. Mainly for this purpose a second thermal camera (FLIR A-20) was installed (Aug. 2011) on the opposite side of the *Sciara del Fuoco* at GST site (Fig. 2.1). This second observation point allows to cover the westernmost side of the Sciara, which was not monitored before. The two cameras also provide valuable information on the development of overflows from both SW and NE crater areas. Before the installation of the first FLIR thermal camera, an infrared thermometer pointing at the NE side of the crater terrace was installed at ROC. The thermometer has an aperture of 30deg and resolution of 0.1°C, which is provided by an uncooled microbolometer sensor with 7.5-13 μm spectral interval sensitivity. This thermal sensor was transferring the data at 50Hz to the digitizer of the ROC seismic station, and was operative until 2014. The infrared thermometer provides an integrated value of temperature for its field of view.

2.3.5 Volcanic Radiative Power (satellite-based)

Satellite-based thermal monitoring is achieved from the MODIS sensor onboard the Terra/Aqua satellites. It allows large scale imaging of the volcanic activity but at low spatial and temporal resolution (2 images per day, 1 km resolution). Automated processing of the images is performed in near real-time by MIROVA (Middle InfraRed Observation of Volcanic Activity, www.mirovaweb.it), a system dedicated to volcanic hot-spot detection developed in collaboration with the University of Torino [26]. The Volcanic Radiative Power (VRP) is calculated using the MIR method [118], and is used to measure the intensity of volcanic thermal emissions, which are subdivided into 5 distinct levels: low (<107 Watt), medium (107-108 Watt), high (108-109 Watt), and very high (>109 Watt). Typically, normal Strombolian activity is characterized by low/medium thermal emissions, whereas high/very high emissions are recorded during periods of crater overflow and lava effusion [28, 27].

Chapter 3

Approaching the source: two case studies

3.1 Introducing new techniques at Stromboli volcano

During the last decades, geophysical methodologies proved to be able to cast the light on the processes which take place into the shallow magmatic system and drive the Strombolian activity [45]. The use of precise and different kinds of instruments instead of simple human observations has led towards a more detailed and quantitative investigation of the phenomena. Cameras, seismic sensors, acoustic pressure sensors, clinometers, etc. promise to substitute, improve and extend our senses. Even more, the understanding of the explosive dynamics is strictly connected with the evolution of the geophysical techniques. The introduction of new methods or instruments has been always followed by a step forward in the knowledge and understanding of the natural phenomena. In due awareness, two experiments have been conducted on Stromboli and will be here introduced as "case studies". Despite the completely different instruments used, both share the same wish of moving as close as possible to the source of the phenomena we wanted to observe. Each one of those represent in fact an original attempt to measure a determined parameter in the close proximity of its source by using a non conventional approach. Data and results we obtained were valuable and, even more noticeably, confirmed or slightly changed our understanding of the data-set collected in the past years with different instruments.

In the following sections the two experiments will be separately introduced and discussed. The results of the first case have been already published. So that the relative paper is here reported as published. Simply the format is changed accordingly with the rest of the thesis. On the contrary, the second case is still an unpublished matter and will be treated more in detail (and will be published soon!).

3.2 Flashing Arcs: how sound becomes visible

Published as: Genco R., Ripepe M., Marchetti E., Bonadonna C., and Biass S., 2014, Acoustic wavefield and Mach wave radiation of flashing arcs in strombolian explosion measured by image luminance. Geophysical Research Letters, 41, 7135-7142.

Abstract Explosive activity often generates visible flashing arcs in the volcanic plume considered as the evidence of the shock-front propagation induced by supersonic dynamics. High-speed image processing is used to visualize the pressure wavefield associated with flashing arcs observed in strombolian explosions. Image luminance is converted in virtual acoustic signal compatible with the signal recorded by pressure transducer. Luminance variations are moving with a spherical front at a 344.7 m/s velocity. Flashing arcs travel at the sound speed already 10 m above the vent and are not necessarily the evidence of a supersonic explosive dynamics. However, seconds later, the velocity of small fragments is increasing and the spherical acousto-luminance wavefront becomes planar recalling the Mach wave radiation generated by large scale turbulence in high-speed jet. This planar wavefront forms a Mach angle of 55° with the explosive jet axis, suggesting an explosive dynamics moving at Mo=1.22 Mach number.

3.2.1 Flashing arcs: how sound becomes visible

Flashing arcs, commonly considered as the visible evidence of shock-front propagation [71], are sometimes observed during violent volcanic explosions. This phenomenon has been first noticed by Perret [82] during the eruption of Vesuvius and Etna in 1906 and 1910, respectively, and described as *"thin, luminous arc flashed upward and outward from the crater rim"*. Flashing arcs were explained as induced by the change of the air refraction index caused by the compression-rarefraction pressure front [**?**]. A similar phenomenon observed during the 1975 Ngauruhoe volcano eruption has been explained in terms of condensation cloud induced by the propagation of shock waves in the atmosphere causing the sudden change of the water phase, similarly to what observed during nuclear-test explosions [71]. Sometimes in eruptive clouds, weak shock waves can be also generated as a result of the local change of the ash-rich plume density, as during the 1975 Tolbatchik eruption [59]. Despite the increased interest in the acoustic pressure generated by volcanic activity [e.g., [51]; [34]], flashing arcs associated to shock waves have only been sporadically reported in scientific literature. Due to strong attenuation effects, shock waves rapidly decay into acoustic waves, often in the order of a few tens of meter from the source [53], making the measurements of a supersonic moving front practically impossible. Direct measurement of shock-waves velocity using pressure sensor in field is then rare and only confined to large explosive events. Therefore, the measurement of propagation velocities at the vent represents a straightforward but difficult to achieve evidence to demonstrate the validity of the linear acoustics assumption. Measurements reported in the literature almost entirely refer to indirect evidence related to the analysis of the image luminance [119]. Image analysis of flashing arcs thus represents the only method to measure the velocity of the pressure front in the immediate proximity of the source. Image processing of ash-laden plumes at Aso

and Sakurajima volcanoes allowed to track the moving luminance front in subsequent frames and to estimate the speed of the associated pressure wave in the range between 342 ± 28 and 574 ± 21 m/s [120, 119]. More recently, propagation velocity of 372 ± 31 m/s in the pressure-induced thermal front of violent explosive eruption has been measured at Yasur volcano (Vanuatu) using thermal camera images [62]. In this paper we present data collected by high-speed camera on Stromboli volcano coupled with infrasonic pressure transducer which allowed the reconstruction of the full acoustic wavefield around the source. As far as we know, this is the first attempt to reconstruct full pressure waveforms by image analysis.

3.2.2 Instrument Setup and Configuration

Explosive activity at Stromboli volcano was recorded by a high-speed, high-resolution Phantom v10 camera and by infrasonic pressure sensor with a sensitivity of 0.025 V/Pa in the 0.0-300 Hz band. Infrasonic data are acquired at 24 bits with 500 Hz sampling rate, while the camera was configured for manual trigger acquisition. The synchronization between camera and the pressure transducer has been realized by recording the analog trigger of the camera in the acquisition system used for the infrasonic sensor, and it has hence the precision of the sampling interval (±2 ms). The Phantom v10 camera works with 2400 × 1800 pixels wide, 14 bit depth, CMOS sensor. At full resolution, camera can record up to 480 frames per second (fps) storing data on an internal circular buffer of 12GB DRAM memory. In our experiment we set HD resolution (1920 × 1080 pixels) at 500 fps and 900 μs of exposure. According to this configuration the maximum recording time was of ∼7 s, and we set the start time 3 s before the trigger. Thus, memory size allowed up to 3402 frames of recording, 1500 of which before the trigger and 1902 after it. The camera was looking at the SW side of the crater terrace from the *Pizzo Sopra la Fossa* ridge, with a dipping angle of 32° below the horizontal. A line of sight distance of 266 m was measured using a laser telemeter from the camera to the SW crater rim (Figure 3.1a). Assuming the field of view (FOV) being a planar surface perpendicular to the line of sight and neglecting distortion and projection errors, the used lens provided a pixel angular size of 2×10^{-4} radians, resulting in a video resolution of 0.053 m per pixel. This gives a full frame size of circa 102 by 57 m, with the SW vent in the lower right corner of the frame and allowing the observation of almost 50 m above the vent (Figure 3.1b). The long time required for transferring data from the camera to the external disk (15-20 min for each acquisition run) was the main limit during the acquisition campaign. This limited our data set to few significant explosive events. We focus here our analysis to the best recorded explosive event occurred at 11:43 GMT on 26 May 2011.

3.2.3 High-Speed Image Luminance Processing

The analyzed explosive event consists of a ∼9 s long-lasting, gas-rich emission with a few ballistics, producing a well collimated jet from the SW vent, exiting with an angle of ∼ 25° respect to the vertical (Figure 3.1b). The associated infrasonic signal is characterized by an impulsive onset of 12 Pa (peak-to-peak) at ∼6.5 Hz, followed by a high-frequency coda ranging between 15 and 100 Hz, with maximum amplitude of 20 Pa at ∼24 Hz and a duration consistent with the duration of the explosion

(Figure 3.2b). Several flashing arcs were visible by eyes and evident also on the video as luminance disturbances traveling across the vapor plume partially masking the crater area (Movie01.avi in the supporting information). According to the common interpretation [e.g., Yokoo and Ishihara, 2007], when a positive compressive pressure front ($Wave_{(x,y,t)}$) moves across the over-saturated vapor plume it causes the sudden evaporation of water droplets, which decreases the local plume density and makes the vapor layer "thinner". In contrast during the rarefaction phase, the rapid vapor condensation causes an increase in the plume density and the vapor layer becomes "thicker". This decrease and increase in plume density are recorded by camera as luminance variation L which is a function of time and of the 2D FOV space $L = f_{(x,y,t)}$. Considering each frame as a multilayer composited image, luminance depends on the static contribution of the FOV background layer $Bkgr_{(x,y,t)}$ blending on the distribution of the vapor plume $Plume_{(x,y,t)}$ in the image. That is, the vapor plume is a second foreground layer of the image, which is masking (blending) the static background scenario. As the pressure wave $Wave_{(x,y,t)}$ propagates across the plume, the pixel luminance is perturbed such as $L_{(x,y,t)} = Bkgr_{(x,y,t)} \bullet [Plume_{(x,y,t)} + Wave_{(x,y,t)}]$, where the symbol ($\bullet$) represents the blend operation acting on the two layer compositing [58]. To enhance the fluctuations produced by the propagation of the pressure wave $Wave_{(x,y,t)}$, we high-pass filter luminance $L_{(x,y,t)}$ in space. Filter eliminates the permanent static offset of the background $Bkgr_{(x,y,t)}$ and the slow ($<$10 m/s) movement of the vapor plume $Plume_{(x,y,t)}$ produced by the wind and/or by the buoyancy. A 2-D gaussian blur filter (5×5 pixel matrix, with $\sigma = 0.5$) is applied to reduce noise and spatial aliasing in each image, followed by the pixels decimation via bi-cubic interpolation. The original (1920×1080) pixel frame is thus reduced to 192×108 pixels, each representing the average contribution of 10×10 2D filtered grid. Finally, luminance of each processed pixel during the 7 s long record is filtered in time using a one-way Butterworth band-pass filter of 3th order in the 1-50 Hz frequency band. The choice of the appropriate filter bandwidth depends on the frequency content of the luminance oscillations, and it must be tuned to maximize the signal-to-noise ratio (SNR). The theoretical frequency limits for this method depend on the camera setup (frame interval and pixel size), propagation velocity, and wavelength of the pressure signal, which in our case is $\sim$250 Hz.

3.2.4 Image Luminace Wavefronts

This image processing acts both on the spatial and temporal context, removing the long-term variations due to the continuous evolution of the vapor plume $Plume_{(x,y,t)}$ and the permanent offset $Bkgr_{(x,y,t)}$ associated with the background scenario. While decimation after the gaussian filter is increasing the spatial SNR, the filter enhances the temporal oscillation of the luminance in the selected frequency range. The result of this processing is a new movie (Movie02.avi in supporting information) of the acoustic-luminance wavefield associated with the flashing arcs. The video shows a first spherical-shaped luminance wavefront (frame 1020), with a wavelength of $\sim$52 m (Figure 3.1c) originating from the vent and followed, after only 0.03 s (frame 1035), by the first visible evidence of gas emission. This single, 52 m long luminance wave, is followed by a series of shorter ($\sim$17 m long) fronts, associated to the continuous emission of gas and fragments from the vent during the explosion (Figures

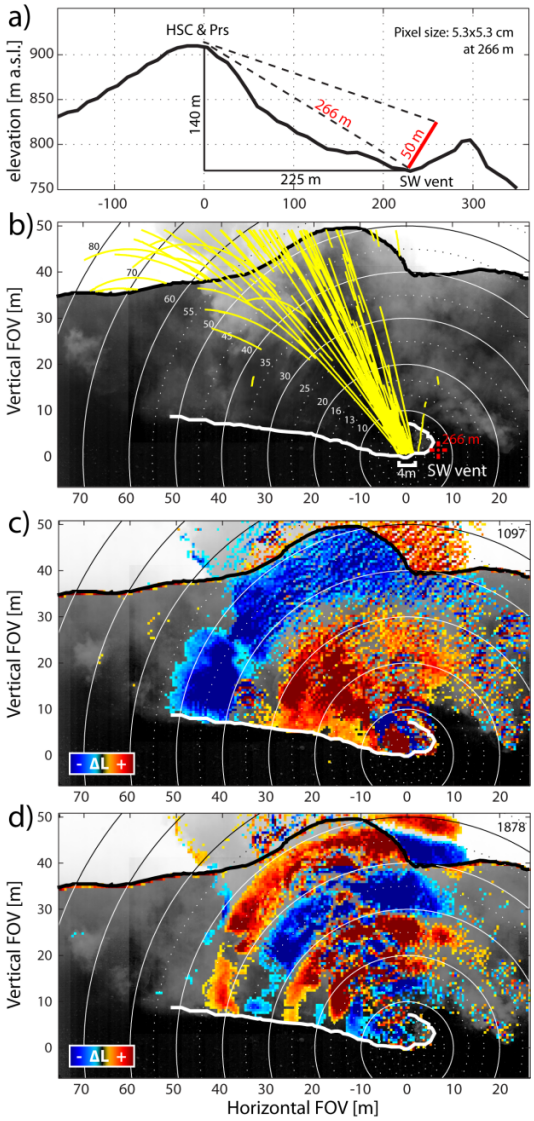

Figure 3.1: (a) Topographic profile of the Stromboli crater including the position of the camera (HSC), the pressure sensor (PRS), and the SW vent. Focal plane is indicated by the red line. (b) Coordinates of the scene are centered in the SW vent. The trajectories of the lava particles (yellow lines) are used to calculate inclination of the explosive jet and the dimension of the vent (2 m). White circles indicate the radial distance from the vent in meter. (c,d) Two frames of the luminance wavefield obtained by image processing show the acousto-luminance long wavelength (∼52 m) onset followed by shorter wavelength (∼17 m) waves during the sustained jet-like explosion. Colors indicate the wave polarity with red and blue for the high and low luminance, respectively. Note the polarity reversal at the ground-sky border in both frames (see text for explanation).

3.1c and 3.1d). It is worth noting that luminance fronts are well defined only within the contour of the vapor plume layer and are clearer where the plume is denser. The polarity of luminance reverts (from blue to red in Figures 3.1c and 3.1d) on crossing the ground-to-sky border line. This observation has strong implication on the physical origin of luminance. In fact, the increase of pressure in adiabatic conditions

implies a relative increase in air temperature, which in a plume saturated of water vapor, will cause the partial evaporation of water droplets and hence the decrease of the plume density. Because luminance depends on the combined contribution of the background ($Bbkg$) and of the plume ($Plume$), the decrease of this second term will result in a relative increase of the background contribution on the total luminance. Since the FOV of the camera includes both the crater terrace and the open sky above the rim, when plume becomes thinner by the passage of a compressive positive front, luminance L(x,y,t) will decrease (blue in Figure 1c) on the dark crater floor background, and will increase (red in Figure 3.1c) on the bright background sky. In conclusion, acousto-luminance and pressure wave will have reverse polarity on a dark background but will have the same polarity on the brighter background sky.

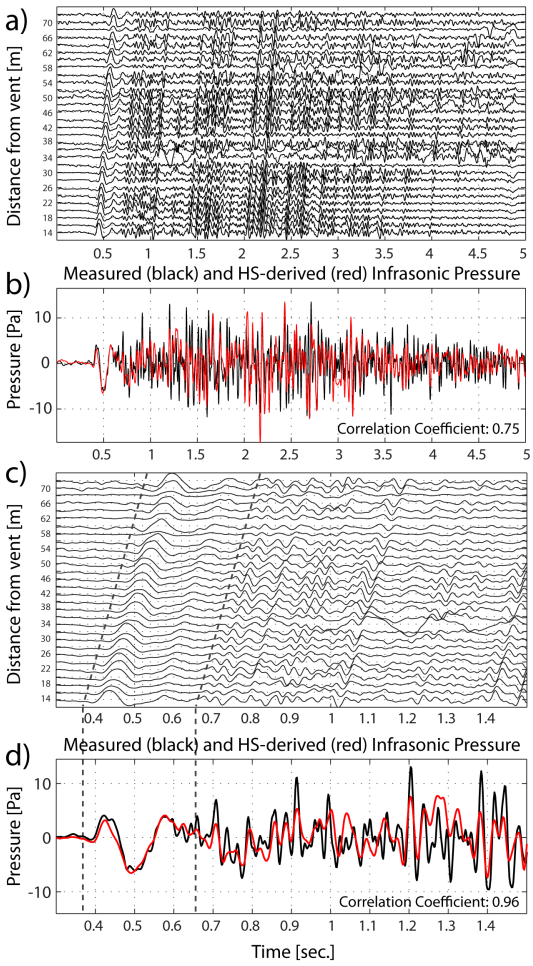

Figure 3.2: (a,c) Acousto-luminance waveforms in the 14-72 m range from the vent. Time series refer to individual 10 × 10 pixel subdomains band-pass filtered in the 1-50 Hz range. (b,d) Comparison between measured infrasonic pressure (black) and the acousto-luminance waveform (red) obtained by stacking 4585 time series. Acousto-luminance amplitude is normalized to the low-frequency initial acoustic waveform. Dashed lines in Figures 3.2c and 3.2d indicate the portion of the signal used in the processing of 3.3.

3.2.5 Luminance-Derived Virtual Infrasonic Waveform

The output of our image processing is a set of 20,736 traces representing the virtual pressure signal derived from the luminance variation measured in each pixel of the FOV. Our processing is thus transforming the image in a surrogate network of pressure sensors deployed around the source. Each pixel is recording pseudo-acoustic luminance-derived signal, which nicely correlates to the acoustic pressure detected at the PRS sensor (Figure 3.2a). The correlation increases when the acousto-luminance signals are shifted for the time lag, normalized, and stacked together (red line in Figures 3.2b and 3.2d). Comparison between stacked luminance-derived acoustic pressure and the infrasonic signal (Figures 3.2b and 3.2d) shows a correlation coefficient of R = 0.96 for the low-frequency initial onset, becoming lower (R = 0.75) for the high-frequency second phase (Figure 3.2d). The relative amplitude of the luminance is also comparable to the measured acoustic amplitude, which demonstrate that changes in luminance are generated by the moving front of pressure waves and that acoustic waves can be successfully derived by image processing. Besides, the wavelength (52 m) measured on the image (Figure 3.1c) and the frequency (6.6 Hz) of the infrasonic onset indicate that acousto-luminance waves are moving at a velocity of 343 m/s corresponding to the sound velocity at the ambient temperature of 18°C at 900 m asl and 100% of humidity.

3.2.6 At-the-Source Acousto-Luminance Propagation Speed

This dense distribution of virtual sensors allows the detailed analysis of possible velocity changes of the acousto-luminance wavefront in the proximity of the source. Propagation speed of the luminance is explored through a full-frame analysis of the 20,736 time histories. In order to avoid any a priori constrain on the luminance propagation, we calculate the delay time between pixels as the time difference with the pixel that contains the signal with the highest correlation coefficient with the larger number of traces. Two different matrices representing both the spatial distribution of the cross-correlation coefficients (Figure 3.3a) and the corresponding time delays (Figure 3.3b) are calculated. Distances between pixels are reduced to the vent position, derived from the analysis of the particle trajectories (Figure 3.1b). Propagation speed is calculated as the ratio between distances and delay times only for the 4585 signals with correlation coefficient larger than 0.9 (Figure 3c). These 4585 independent propagation velocities show a gaussian distribution around 336.7 m/s with a standard deviation of ±9.2 m/s. This uncertainty in the velocity corresponds to an error of 2.7% in the conversion of the frame dimension into meter as possible consequence of underestimating of only ∼7 m the slant distance. However, in spite of the possible uncertainty, delay times show a linear trend with the distance compatible with a propagation velocity of 344.7 m/s (Figure 3.3c). This velocity is consistent with the expected sound speed in air (at 20°C, 900 m asl, 100% humidity) and with the wavelength (52 m) and the frequency (6.6 Hz) of the acousto-luminance wavefield. No evidence of possible change in slope in the traveltime distribution is visible. This suggests that the flashing arcs observed during the strombolian explosion were, at least in our field of view and already after 14 m above the vent, propagating at the sound speed and that are not necessarily related to the propagation of shock-wave fronts.

3.2.7 Mach Wave Radiation and Mach Number

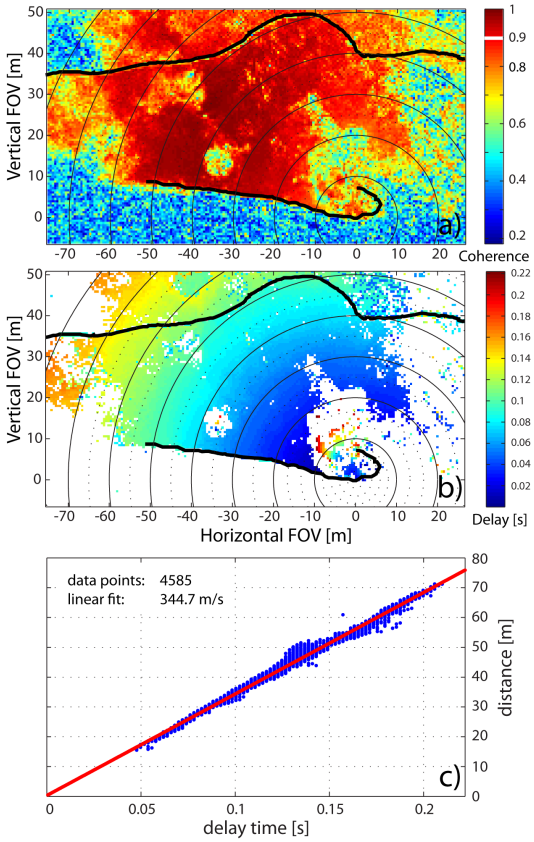

Figure 3.3: (a) Map distribution of the cross correlation between the 20,736 acousto-luminance signals with the reference pixel (read text for details). (b) Time delays between the 4585 acousto-luminance signal showing correlation values >0.9 are reported to the pixel closer (black dot) to the vent position (see Figure 3.1b). (c) Delay time distribution for 4585 acousto-luminance signals show a very good ($R^2 > 0.9$) linear fit (red line) indicating a propagation velocity of 344.7 m/s.

Acousto-luminance wavefronts originate at the vent and spherically propagate across the FOV with a velocity compatible with the sound speed in ambient condition. However, during the short wavelength acousto-luminance phase, occasionally wavefronts deviate from their spherical shape and assume a planar-like front. This could be generated by the increasing of the sound speed induced by the change of ambient temperature moving toward the hot jet. However, persistency of the spherical shape of the luminance wavefront does not suggest large temperature effect on the sound speed in the vapor plume, but rather is more consistent with a uniform temperature distribution. Actually, plane wavefront moving downstream of the explosive jet closely resembles the Mach wave radiation pattern described for high-speed jets [[108] and references therein]. Mach wave radiation is believed to be generated by large scale instability of the jet traveling with supersonic speed with respect to the ambient sound speed and dominates in the far field with respect to the fine scale turbulence effects. Mach wave radiation fronts propagate at the speed

of sound forming in the near-field the characteristic Mach angle (γ) with the jet direction:

$$\sin(\gamma) = 1/M_o, \tag{3.1}$$

where the Oertel Mach number (M_o) [73]; [77] is related to the velocity (u_j) of the gas in the jet:

$$u_i = M_o c_a + c_j(M_o - 1), \tag{3.2}$$

where c_j and c_a are the speed of sound in the jet and in the surrounding atmosphere, respectively. The Mach angle can be directly measured on the image and, in our case, is $\gamma = 55°$ (Figure 3.4b), which corresponds to an Oertel Mach number M o = 1.22. For low Mach number, the contribution of the sound speed in the jet c_j is small (equation 3.2), and jet velocity mainly depends on the sound speed in the ambient atmosphere ($u_j \sim M_o ca$). We thus calculate that the expected minimum jet velocity to generate the observed Mach wave radiation should have been u_j =∼417 m/s. Mach wave radiation pattern is not always visible during the explosive event suggesting that the gas exit velocity was probably not stable but rather oscillated around sonic and supersonic conditions. From high-speed camera imagery it is not possible to measure the velocity of the gas but only the velocity of the lava fragments transported in the jet, which indirectly allows inferring on changes in the jet velocity.

3.2.8 Particles Velocimetry and Infrasonic Energy

Particle velocity is calculated by using an algorithm adapted from the track.pro code [29], which identifies particles larger than few centimeters in two successive frames. Consistency of the result is stated for trajectories with at least 30 points and confirmed by visual inspection. A total of 147 reliable trajectories for 16,713 instantaneous velocity values are hence obtained (Figure 3.4c). The first particle is observed 0.268 s after the gas (frame 1169 in the Movie01.avi supporting information) and 0.8 s after the infrasonic onset. Particle velocities reach 227 m/s soon after the onset and decrease after 1 s down to ∼90 m/s. However, velocity of the particle increases again after 2.25 s reaching ∼247 m/s. After that, the general trend of the particle velocity is decreasing, but still some particles are detected to move at a velocity of 250 m/s. These high particle velocities have already been observed [30]; [44] also few seconds after the onset [107] and are all confined in the central part of the explosive column along the gas-jet major axis. Energy variation of the acoustic signal is following the same trend of the particle velocity (Figure 3.4c). When acoustic energy increases also particle velocity increases reaching the higher values ∼2 s after the explosion onset. Consistently, Mach waves are observed during this high particle velocity and high infrasonic energy phase suggesting that gas thrust can accelerate also after the explosion onset to supersonic velocity. This result supports the supersonic dynamics of volcanic jets [65] inferred by the waveform skewness of wide-band acoustic signal measured also during strombolian explosion [40]. While the first low-frequency (6.6 Hz) infrasonic onset is induced by the deformation of the magma surface during the fragmentation, the higher frequency (>20 Hz) content is linked to the eruptive jet dynamics.

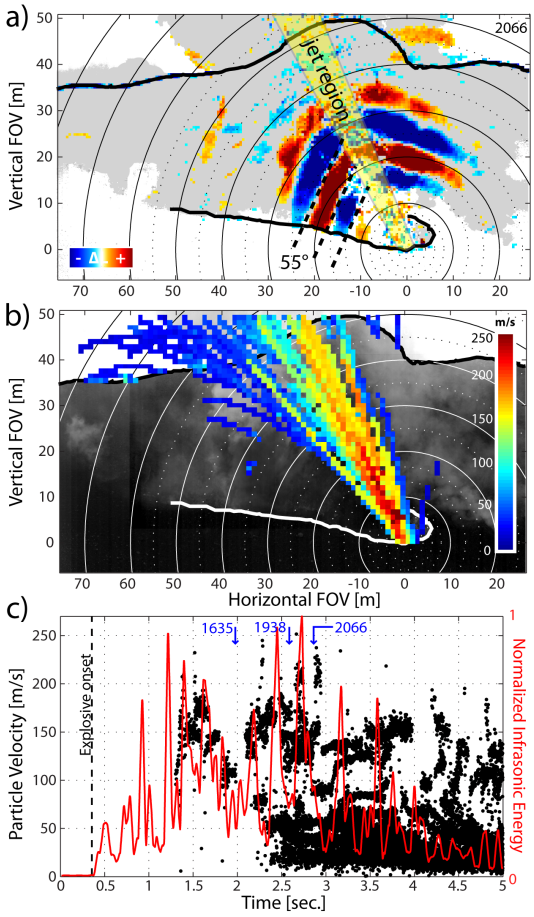

Figure 3.4: (a) Planar wavefront of the luminance wavefield forms a 55° Mach angle with the explosive jet. Shaded in gray the area covered by the vapor plume. (b) Map of the peak velocity distribution for the 147 particles tracked during the explosion shows velocities >150 m/s concentrated in the center of the jet. The map is calculated by considering in each frame the highest measured particle velocity in an area 2 × 2 m large. (c) Distribution of 16,713 instantaneous velocities (black dots) shows particles with a velocity of 227 m/s at the explosion onset, reaching the maximum velocity of 250 m/s after ∼2 s. Infrasonic energy (red line) is following the same trend of the particle velocity. Blue arrows indicate the frame number where Mach wave radiation patterns become visible (Movie02.avi in supporting information).

3.2.9 Summary and Conclusions

Pressure waves generated by volcanic explosions traveling in the open air, water clouds, or volcanic plume may become visible as flashing arcs, generally explained as the evidence of non-linear acoustics generated by a supersonic dynamics. This has strong implication on the interpretation of the pressure waves in terms of explosive source dynamics. Since shock waves quickly decay to sound waves already at short distance from the source [67], the direct measurement of supersonic propagation front can be hardly achieved on a volcano. Our image processing allows deriving the full acoustic wavefield from the luminance induced by the propagation of pressure fronts generated by explosive dynamics. Processing fully preserves the spatial dis-

tribution of the pressure transient and allows calculating wavelength and frequency content of the acousto-luminance wave. Each pixel of the high-speed frame is used to measure how the pressure wavefield moves around the source, providing a reliable reconstruction of the acousto-luminance waveform in the proximity of the vent. We showed that flashing arcs observed during strombolian explosions are generated by pressure waves moving at the speed of sound (344.7 m/s) with a spherical wavefront centered at the vent. Flashing arcs are not reported in literature for waves propagating at sonic speed, and our record constitutes the first evidence of such phenomenon in linear acoustic conditions. However, soon after the explosive onset the infrasonic amplitude increases, the frequency content becomes higher and the wavelength of acousto-luminance shorter (Figures 3.1d and 3.2b). Exit velocity of lava fragments also increases, suggesting that jet velocity is increasing after the explosive onset. This is associated with planar luminance wavefronts moving at the speed of sound downstream of the explosive jet and closely recalling Mach waves produced by a gas jet moving at Mach number $M_o = 1.22$. The presence of Mach waves $\sim$2 s after the explosive onset, indicates that gas also during small explosive event can experience further sharp accelerations forcing the jet to move at supersonic velocity. This is consistent with the supersonic dynamics inferred from the asymmetry of the sound waveform recorded during gas-dominated explosion at Stromboli [40]. We suggest that the first infrasonic pulse could represent the pressure front originated by the sudden doming of the magma column due to the over-pressured gas, while the successive higher frequency component is linked to the turbulence of the gas leaving the conduit with supersonic velocity. The origin of the acceleration in the gas jet dynamics has not been explained yet and could have strong implication in our understanding of the explosive dynamics as well as of the acoustic source process.

3.3 Radar Interferometry: observing displacements

Abstract In May 2014, an interferometric Radar (IBIS-S) was experimentally tested on the Stromboli volcano. With the aim to detect small ground displacements associated with the explosive activity, the instrument was deployed at the summit peak (*Pizzo sopra la Fossa*) pointing downward into the crater terrace. The collected data clearly show a significant displacement with amplitudes up to a few millimeters. Its spatial pattern is consistent with the dilatation of the vent, starting a few seconds before the visible onset of the explosion, and the subsequent contraction during the ejection phase. The comparison of radar data with other geophysical measures from the permanent monitoring network or from other temporary installed instruments reveals that the deformations observed at the vent are consistent with those provided by seismic and clinometric data in terms of shape and timing. However, their amplitude and spatial distributions are in opposition with what is deduced from previous studies of the source mechanism and position. This seems to suggest that the source of deformation responsible for VLP signals could actually be much shallower that what was generally accepted.

3.3.1 Radar interferometry

The Radar (*RAdio Detecting and Ranging*) is an active sensor designed to detect targets in his field of view and measure relative distances using a beam of radio waves. It transmits radio waves in a certain frequency band and measuring the echoes generated by the targets. Objects placed at different distances will be resolved based on their different delay time. The field of view of the radar system depends on the transmitted energy, sensitivity and type of antennas. On the radar side, the observed scenario appears as a mono-dimensional range of distances. Each range will receive the contribution of all the targets (reflectors) placed at the same distance from the sensor. The thickness of these ranges represents the range resolution of the system, where the azimuth is limited by the antenna configuration (Fig. 3.5). A radar echo signal contains a dual information, *amplitude*, which is dependent on the characteristics of the target, such as shape, dimension, orientation, material etc.; and *phase*, that is related to the distance between sensor and target. A so called *coherent* system is able to resolve both components, so that the changes in phase of the target over time can resolve the changes in distance of the object. This technique, known as *radar interferometry*, is widely used for the remote sensing of small displacements with an accuracy of a few millimeters.

3.3.1.1 The IBIS-S interferometric Radar

The *IBIS-S* radar interferometer, produced and distributed by *IDS Ingegneria Di Sistemi S.p.A.*, is a compact, transportable, ground-based Microwave interferometer with 1-D imaging capabilities for remote measurements of displacements (Fig. 3.6). The radar system works in the microwave band (10 GHz) in *Stepped Frequency Continuous Wave (SFCW)* mode. This means that the signal is continuously transmitted over time and its frequency is slightly, monotonically changed by discrete steps $f_n = f_0 + N\delta f$, in a cyclic pattern. The single cycle is called *sweep*. At the

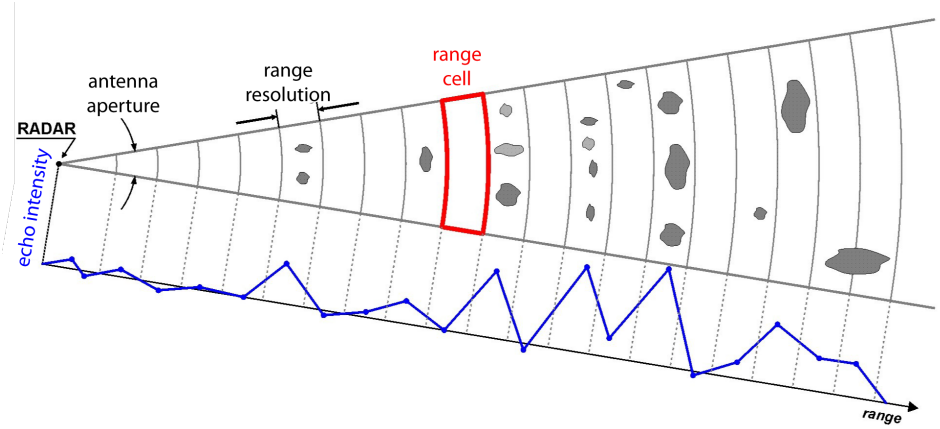

Figure 3.5: Sketch of a 2-D scenario with ranges and targets as will appear under the radar point of view, as a 1-D range of distances. To each range of distance, a value of amplitude depending on the amount of reflected energy, will be associated.

end of a sweep, the system has acquired a vector of complex numbers that corresponds to a frequency sampling of the observed scenario. This vector is processed via IDFT (Inverse Discrete Fourier Transform) to translate the frequencies to ranges (i.e. distances). Exploiting this technique the IBIS system build a one dimensional image, called *Range Profile*, where the targets in the illuminated scenario are resolved with a range resolution independent from distance. Every sample of every range is characterized by both amplitude and phase information. Differential interferometric analysis allows to evaluate target displacement between each measure. The range resolution of the IBIS-S instrument is ≥ 0.5 m and varies according to the maximum distance (up to 2 km) and the rate of sampling. The nominal accuracy of the measured displacement is < 0.1 mm. The sampling rate also depends on how the other parameters are configured, but can go up to 100 Hz.

3.3.1.2 Limits and uncertainties

The displacement measured with radar interferometry is affected by several limitations which have to be taken into account when interpreting the data. In the following sections these limitations will be briefly introduced.

- ***Single component measurement*** The interferometric technique is based on the comparison of two measures of phase relative to distinct times. The measured displacement represents the variation of distance along the line of sight between the instrument and the target. This means that the instrument is only able to detect the component of displacement projected on this line. Hence the position of the instrument with respect to the target area and the expected direction of movement is a key choice in order to maximize the capabilities of the instrument. Moreover this factor has to be always taken into account when reporting the observed displacements to avoid misleading interpretations.

- ***Phase ambiguity*** The phase of an electro-magnetic wave is an angular phys-

Figure 3.6: IBIS-S interferometric radar, produced by *IDS - Ingegneria Dei Sistemi*

ical quantity scaling in the $[0 - 2\pi]$ interval. Considering that the distance between the radar and the target is many times larger than the wavelength of the signal, the phase will cyclically change and the Radar sensor will only reveal the fractionary part of this phase shift. This implies a phase ambiguity which can only be resolved assuming that the displacement of the object is smaller than $\pm 1/4$ of the wavelength (λ). For the IBIS-S instruments this corresponds to $\pm 4.38mm$ (Fig. 3.7). This means that the displacement between two consecutive measures cannot exceed this value whereas it does not imply any direct limit for the cumulative displacement that is recovered using *phase unwrapping*.

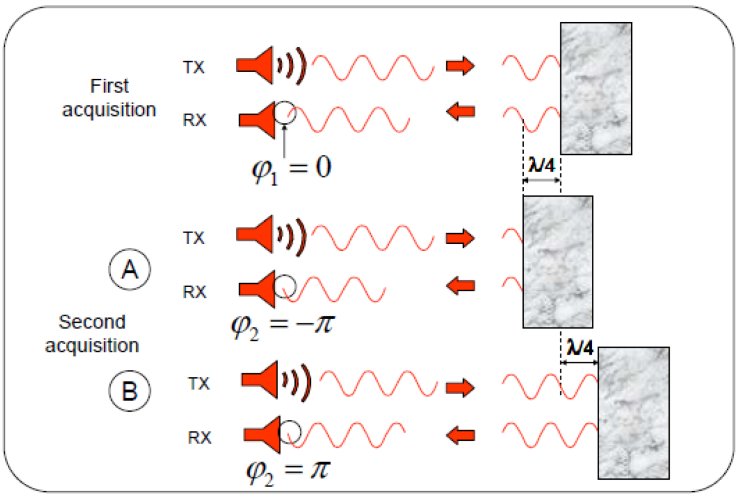

Figure 3.7: Phase ambiguity bounds the maximum displacement measurable between two consecutive acquisition to $\pm\lambda/4$. For the IBIS-S system this value is equal to $\pm 4.38mm$.

- ***Coherency*** The signal returned from each range-bin represents the cumulative, averaged, information of all reflectors within the same distance range from the sensor. The contribution of each reflector will be proportional to the amount of energy reflected. The interferometry will only works when the displacements occurring in a range-bin are "coherent". Coherency is a measure of how much the scenario is maintaining its appearance over time. The higher is coherency the more the displacement is consistent over the full range, and then representative. The coherency is computed using the amplitude information of each range. When the change in the observed scenario is larger than a certain coherency threshold it *"decorrelates"*, causing a loose of meaning of the displacement measure in that interval of time for that range bin.

- ***Atmospheric effects*** The transmitted signal propagates across the atmosphere with a speed which depends on the properties of the medium. Relative humidity, temperature and pressure are in particular the more effective. Due to the fact that distance measurement is basically a delay-time measure, a change of the speed of propagation over time will appear as a change of distance of the observed scenario. Usually, atmospheric effects are negligible for short acquisition or over reduced distances, whereas they might be significant for slow displacement and long-range measurements. A cloud crossing the field of view, as an example, could notably affect the measurement, resulting in an apparent movement of the objects behind it.

3.3.1.3 Accuracy of the interferometric measurement

Considering the instrument characteristics and the limitations due to the actual scenario and experimental setup, the accuracy and reliability of interferometric measurements can differ from the nominal ones. As discussed in the previous section, the effect of limits and its uncertainties can be partially reduced by a proper setup and configuration of the instrument. However, in common environmental condition, where the observed scenario is constituted by rocky solid ground or buildings, and at a distance of a few hundreds of meters, the accuracy of the instrument is maintained to $0.1 - 0.2$ mm, at least when short-term displacement, occurring in a few seconds to tens of seconds, are considered.

3.3.1.4 Data Timing

The accurate timing of the interferometric data-set represented a struggling problem for its use at Stromboli. While the internal clock of the instrument guarantees the sampling frequency, the absolute time of the samples only rely on the internal clock of the recording computer. The lack of absolute timing prevent any possibility of reliable correlation with the other geophysical parameters acquired by the various instruments. The system clock of a laptop in fact, without a synchronization with an external clock, is not stable over time. Moreover a possible sync of the system clock with an external source may produce time vector anomalies when not directly controlled. The solution was found writing a specific piece of software connecting it to an external GPS unit and keeping track of time difference between the internal

computer clock and the absolute UTC time. Interferometric data timing is thus obtained by time correction during the post-processing phase.

3.3.2 The May 2014 experiment

On May 2014, a temporary experiment was designed to test the capabilities of the interferometric radar to detect ground displacements associated to the ordinary explosive activity of Stromboli volcano. The radar measurements were integrated by thermal imagery, infrasound records ans seismic measures provided by temporally installed stations in addition to the permanent network. Due to the limited battery life of the laptop used to acquire radar and thermal camera, each acquisition run lasted 2-4 hours. The experiment was repeated for three days, from slightly different sites and pointing at different vents, on May 21th, 23th, and 25th. The explosive activity was mainly concentrated to the NE crater area and characterized by gas rich explosions, lasting a few seconds. The usually monitored geophysical parameters (seimsic tremor, infrasound acoustic pressure, thermal activity etc.) were all in the medium ranges of the ordinary Strombolian activity.

3.3.2.1 Instrumental setup

The installation of the instrument is composed of a radar head (Fig. 3.6), sitting on a robust tripod which allows the pointing with the help of a gunsight, and a laptop, designated to collect and pre-process radar data using a proprietary software from *IDS*. While the laptop is powered by its internal battery, the radar head needs to be connected to external 12V batteries. In a temporary deployment the main limiting factor to the duration of the acquisition is then represented by the laptop battery. In regular conditions this allows 3-4 hours of continuous record. However, due to the fact that a possible software crash implicates the lost of data, it was preferred to stop and restart the acquisition every 15-30 minutes.
The particular topographic setting of Stromboli volcano is rather favorable to such radar measurements. In fact, the crater terrace, with its active vents, lies $\sim 150m$ below the *Pizzo sopra la Fossa* top, at an horizontal distance of $200 - 300m$. This allows to directly observe the vents from a convenient point of view. Radar was alternatively pointed towards the NE and SW areas of the crater terrace. The antenna aperture of 15° on the horizontal plane and 13° on the vertical, leads focusing on a single vents or at least discrete portions of the crater area (Fig. 3.8). Acquisition parameters were tuned to maximize the time and space resolution. The best equilibrium was found using a sampling rate of $40Hz$ with a range resolution of 0.5 m and a full range of 400 m.
A thermal camera (*FLIR SC660*) was acquired at a frame rate of 10 samples per second. The camera was co-located with the radar and pointed to the same crater. The syncronization of the camera was also obtained using the same method described for the radar. Seismic broad-band sensor (*Guralp CMG-40T*) and infrasound pressure sensor were installed close to the radar site and acquired for the whole duration of the experiment at $100Hz$. Timing of seismic and infrasound data was guaranteed via GPS sync from the digitizer (*GURALP CMG-DM24*).

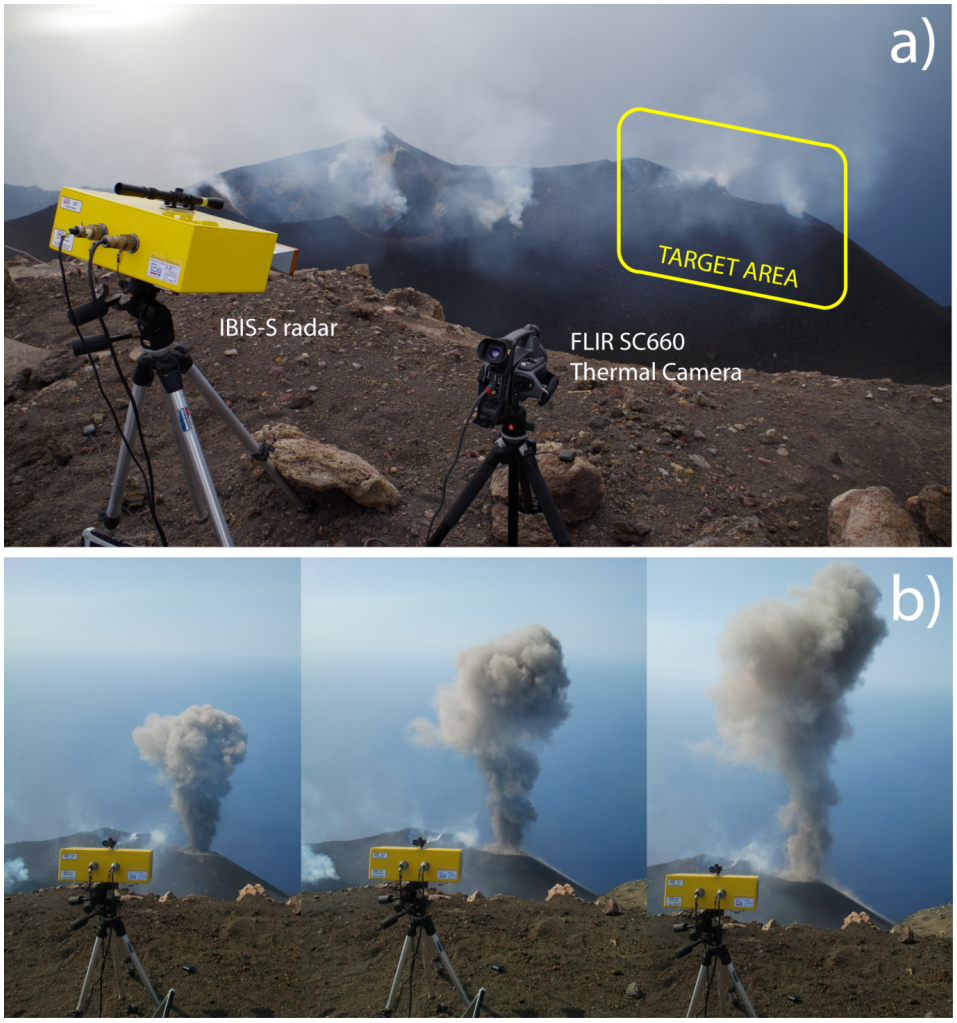

Figure 3.8: (a),IBIS-S radar and FLIR SC660 thermal camera setup during the May 2014 experiment. The approximate target area is there evidenced. (b), Sample images of an ash-rich explosive event from the NE vent recorded in succession.

3.3.2.2 Data analysis

A first pre-processing of the radar raw data is performed directly in the field by the software designed for the acquisition. The main interferometric processing is done using the appropriate software *IBISDV (Image By Interferometric Survey-Data Viewer)*, released by *IDS*. The software return a displacement trace for each selected range-bin. The software allows to select the traces based on the amount of energy reflected. However we preferred to follow the more conservative approach, the full range of bins was exported and than "cleaned" during the post-processing phase. Post-processing was implemented in MATLAB® using appositely written code. Procedure was iteratively ameliorated during the data analysis, finally reaching a sort of standard. Once imported, displacement data were first filtered using an *a priori* discrimination threshold based on specific parameters and finally "cleaned" with some *a posteriori* defined parameters to enhancing detected signal. Here, those parameters not dependent on the individuation of a particular signal, but rather depending on the implicit characteristics of the data, are defined as *a priori*, while the *a posteriori* parameters are only defined after the individuation and characterization of signals considered as more significant.

- ***noise standard deviation (a priori)***. The standard deviation of the noise level, computed individually for each displacement time series, was used as a parameter to evaluate the quality of the data. More "noisy" range-bins are assumed to represent areas characterized by a less coherent movement of the reflectors. For this reason they are rejected during the post-processing.

- ***spatial coherency (a priori)***. Traces relative to contiguous ranges should record similar displacements. Such a simplicistic assumption, relies on the fact that the area observed, considering the ground topography, is close enough to a continuum of monotonically increasing distances. Real ground deformations are expected to be coherent over a certain area.

- ***decorrelation (a priori)***. During the explosive event, a large amount of gas and fragments is injected into the atmosphere, changing the acquisition conditions of the radar. Moreover, after the eruption, new material is deposed on the ground in the proximity of the vent. This results in large step-like changes in some range-bin during and after the event. Such a displacement should not be considered as real, even if the displacements recorded between two steps could be reliable.

- ***semblance (a posteriori)***. Once a representative explosive trace is extracted, semblance can be used to refine the data-set by removing those traces which do not show similar waveforms with respect to the reference one. This last method was only used to produce better shaped plots and reference waveforms by signal stack. Despite the fact that is based on numerical computation of cross correlation between traces, yet it is rather subjective about the choice of a representative waveform.

After post-processing the radar data-set is pruned by all the spurious traces and clearly reveals the detected "deformation field" (Fig. 3.9). Correctly speaking,

this pattern is actually the 1-D projection of the 3-D footprint of radar beam on the ground. As already discussed, each range-bin collects the contributions of all the reflectors placed at a similar distance from the radar antennas. For each time interval, a vector expressing the component of ground displacement along the line-of-sight for a profile starting from the center of the antennas and crossing the crater terrace is produced. A positive displacement means the increase of distance between radar and target, while a negative displacement refers to a decrease of this distance.

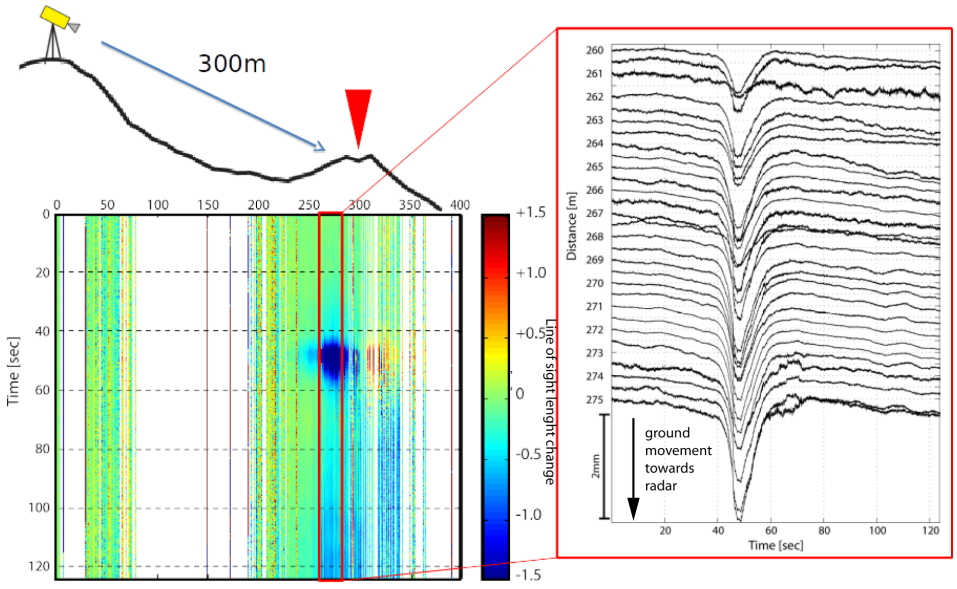

Figure 3.9: Pattern of deformation as observed from the radar during an explosive event. On the left, a sketch of the instrument setting with the displacement pattern is reported. Colors indicate direction and magnitude of the displacement according to the colorbar. On the right, individual traces extracted from the pattern are plotted. Note the self-similarity of the time series at different ranges

3.3.2.3 Results

In figure 3.9 ∼120 seconds of full range post-processed radar data are reported. At nearly 40 to 60 seconds from the beginning of the measure an explosive event is recorded as a significant change of distance (displacement) with a characteristic shape. The blue color represent negative displacement, such as experienced when the target is moving towards the radar. The red color indicate instead an increase of the radar-target distance. The individual time series reported on the left shows a negative displacement of 1-2 mm. It is worth noting that this displacement increases in magnitude approaching a certain range (around 300 m far from the radar) and suddenly reverses its polarity after this distance. This phenomenon is better evidenced in figure 3.10. The 300 m distance is consistent with the position of the exploding vent. The polarity and the spatial distribution of the displacement are coherent with the expansion and successive contraction of the explosive vent. The records associated with range-bins at distances greater than the vent position are relatively worst in term of signal-to-noise ratio. As already discussed in the previ-

ous section, those ranges are strongly affected by the explosive event. Traces from

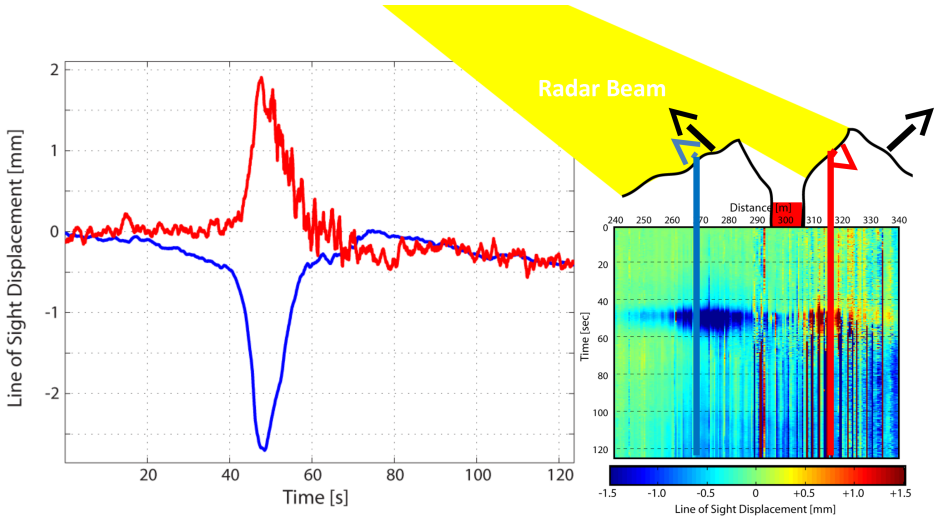

Figure 3.10: Sketch of the crater area where the deformation profile is sampled for two time series. The observed ground displacement represented on the right, is compatible with the dilation and following contraction of the conduit during the explosive event

different explosive events have been collected and compared, revealing that all the recorded events show a similar pattern of displacement (Fig. 3.11a). If traces are scaled and aligned for their maximum, is clearly visible that the inflation phase is almost identical for all the events (Fig. 3.11b), while the contraction phase is less similar and its duration more variable. The expansion phase is lasting ∼5 s.

3.3.2.4 Comparison with other data-set

The Radar data quite meaningfully reveal an expansion and contraction of the vent when explosive events do occur. However, a more comprehensive understanding of the observed displacement arise from the comparison with the other available geophysical parameters such as seismic displacement in the VLP band, ground tilt and thermal derived pseudo-volume (Fig. 3.12). Ground displacement in VLP band is derived from the seismic records filtering and integrating the velocity on the U/D trace, in the 0.05 - 0.5 Hz frequency band. Ground tilt is provided from the OHO station of the permanent network. Thermal pseudo-volume is computed adapting the thermal decomposition method established in *Delle Donne and Ripepe, 2012* [30]. This method allows to calculate the 2-D size of the plume based on different thermal thresholds from the records of the thermal camera installed during our experiment.
Once all data-sets are aligned, the visible onset of the explosive activity can be easily established using the thermal camera records. This allows to notice that the vent dilation observed by means of the radar is actually taking place before the explosive events and reverting to contraction as soon as the ejection starts. The duration of this contraction phase is comparable with the duration of the emission, as evidenced by the thermal pseudo-volume trends.
Interestingly enough, the ground displacement recorded from the radar differs from

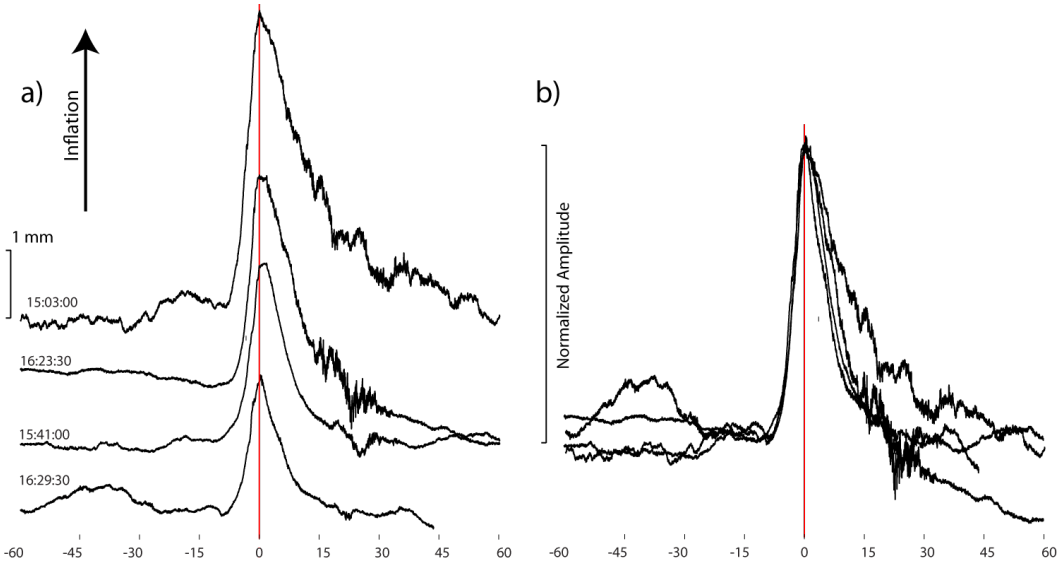

Figure 3.11: (a) Comparison of different explosive events from the same crater and (b) same traces normalized to show the self similarity of the signals

the ground displacement detected by seismic sensors and ground tilt measured from tiltmeters. As evidenced in figure 3.13, the tilt signal is much more smoothed, and the inflation (detected by tiltmeters) reach a maximum about 20 seconds later than the onset of the explosion detected by radar. This may suggest that the two phenomena are not located at the same source directly and tilt could register a pressure change in the deeper part of the conduit.

3.3.3 Discussion and Conclusions

The earlier reported experimentation provided clear evidences that ground displacement produced by the Strombolian activity can be successfully detected and measured using ground-based fast-sampling radar interferometry. Displacements in the order of a few millimeters, reversing their polarity across the exploding vent, were recorded for every explosive event. The observed pattern of deformation revealed the rapid inflation of the upper part of the conduit followed by a progressive contraction. The comparison with the thermal imagery revealed that the ground inflation starts a few seconds before the onset of the explosion and culminates just before of it. The contraction phase in instead accompanying the release of gas and fragments from the conduit and consistent with a pressure decrease into the shallowest section of the conduit. However, the more interesting results arise from the comparison of ground deformation related measures (seismic VLP displacement and tilt). Compared to the displacement resulted from the seismic sensors, that are characterized by a lower corner frequency and a flat response in a limited frequency band, the radar displacement is theoretically able to record from DC to nyquist ($\frac{1}{2}sps$). Hence, to be compared with the seismic VLP, the radar-derived displacement was filtered in the same frequency band. Once this is done, the two waveforms show quite a similar shape (Fig. 3.14) and phase agreement. Also the tilt signals, when coherently filtered, resemble the VLP sesmic signal. This is not surprising as tilt-

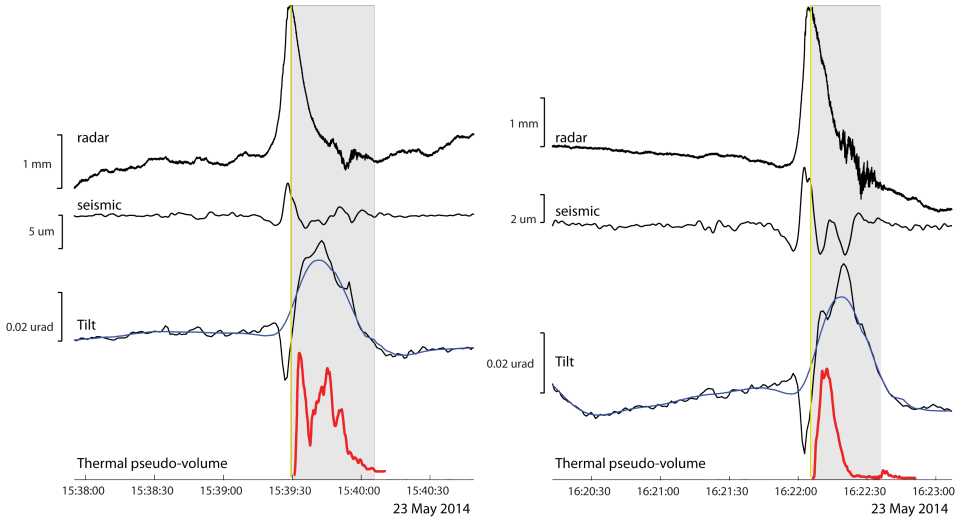

Figure 3.12: Synoptic view of radar, seismic displacement in the 0.05-0.5 Hz frequency band, ground tilt (raw in black and low-pass filtered below 0.05 Hz in blue) and thermal data for two distinct explosive events. All data are aligned by absolute time reference. Yellow lines mark the visible onset of explosive events.

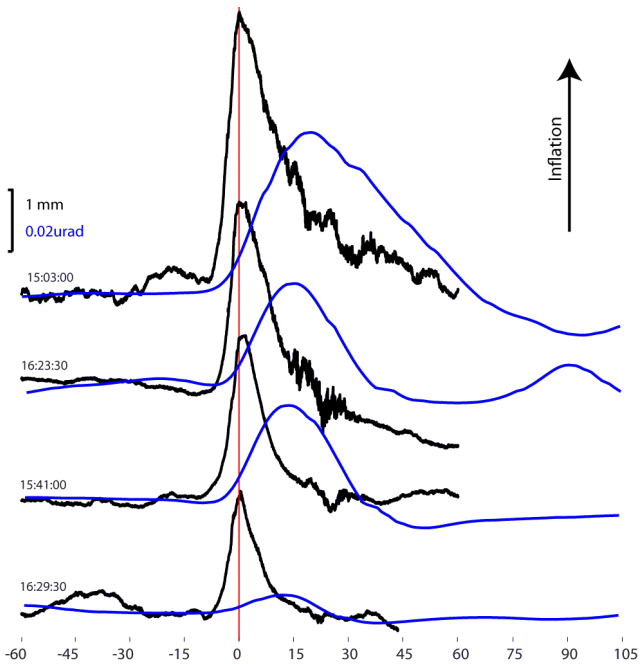

Figure 3.13: Comparison between radar derived displacement (black) and ground tilt from clinometer (blue). Four different events are reported. Tilt signal is low-pass filtered below 0.05 Hz. Note how radar-based ground displacement and tilt scales accordingly in amplitude.

meters are also sensitive to displacement. However when amplitude of the seismic VLP displacement and radar-derived displacement are compared, the radar signals show a magnitude ∼250 times larger than the seismic. (Fig. 3.14). Even under the hypothesis of a large local effect, such a difference in amplitude could hardly be explained assuming a source position located 200 m below the surface [23] [61]. In this case, in fact, the distance between the source and the vent, or between the source and the seimic sensor will be in the same order of magnitude (200 m vs. 400 m). On the contrary this difference will not be unexplainable if we assume a source position coincident with craters and we consider the geometrical attenuation $\frac{1}{r^2}$. This conclusion is also supported by the fact that the VLP signals related to the activity of the SW vent are not detected by the radar when illuminating the NE side of the terrace (while those are clearly visible on the seismic and tilt traces). Only a very local source could produce such a deformation pattern, forcing to conclude that the deformation recorded by the radar is produced by a very local source which is almost coincident with the vent position.

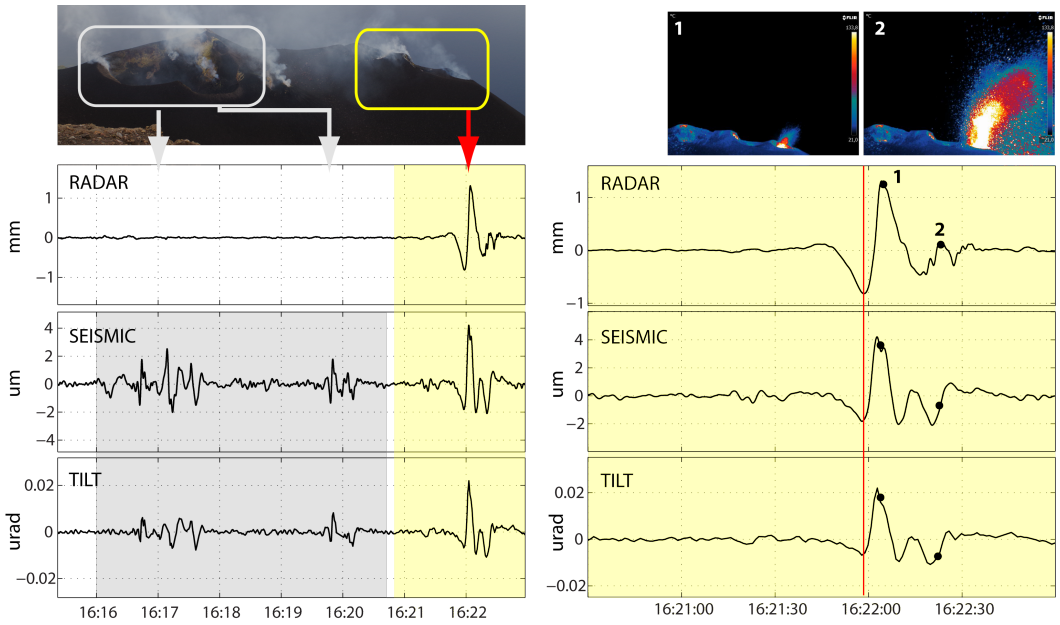

Figure 3.14: Comparison between radar-derived displacement, seismic displacement and ground tilt, all band-pass filtered in the 0.033 - 0.5 Hz VLP frequency band. On top are also reported an image of crater terrace with highlighted sectors and a two thermal frames. Timing of frames is marked by black numbered dots on the traces on the right. Red line marks the onset of the explosive event. Note the similarity of the traces and the perfect synchronization. Magnitude of displacement and tilt is reported on the scales in millimeters (radar) micrometers (seismic) and microradiants (tilt), respectively.

Chapter 4

Explosive activity

4.1 Strombolian explosive activity

The explosive activity of basaltic volcanoes commonly consists of Strombolian-type explosive activity or, more rarely, fire fountains. However steadily erupting basaltic volcanoes (open-vent), also produce occasional paroxysmal explosions (from violent Strombolian to sub-Plinian) representing a major hazard because of their sudden occurrence and larger impact area [102]. Stromboli volcano has been characterized by open-vent conditions, as reported since the 7th century A.D. [104]. In such an open-conduit condition, the gas is released by passive degassing [12], mild explosive activity [45] and lava effusions.
The explosive activity is controlled by the balance between magma supply, outgassing and eruptive rates, mainly characterized by low-intensity, regular Strombolian explosions [86]. However more violent explosive eruptions may suddenly occur without obvious evidences of any precursor. These events, named "Major explosions" or "Paroxysms", depending on their magnitude, have significantly larger intensities (up to $> 10^7$kg of mass ejected for paroxysmal eruptions [86]) relative to ordinary explosions (10^3kg [45]).

- ***Ordinary***. Normal Strombolian activity is described as repeated explosions lasting a few tens of seconds and involving emission of jets of gas and incandescent magma fragments to heights of 100-200 m [6, 45]. Although this activity is persistent, its intensity may significantly vary over time [6].

- ***Major***. Major explosions are powerful enough to eject blocks and bombs at distances up to 1.5 km [6]. Major events last for a few tens of second and form ash and lapilli charged plumes reaching eights up to a few hundreds of meters. There is no robust statistics about occurrences of Major events and their definition is not intrinsically precise. In the last years an average of 2-3 events/year was reported [7, 86].

- ***Paroxysmal***. Paroxysms represent the most powerful explosive event for Stromboli and are characterized by large amounts of ejecta associated with the development of a plume rising up to some kilometers [6]. Occasionally, associated pyroclastic flows are described, and ballistics bombs and tephra may reach the inhabited areas of the island [47]. In the last centuries 27 paroxysmal events have been reported in literature [6]. In the last decades a paroxysmal explosion every 5-7 years has occurred [104]. The last two Paroxysms, both occurred during major effusive crisis, on April 5, 2003 [16, 103] and March 15, 2007 [93], were powerful enough to reshape the summit crater terrace.

4.1.1 Petrographical and geochemical Characters

Composition, crystallinity and vesicularity of tephra ejected during Ordinary, Major or Paroxysmal explosions show fundamental differences in their characteristics, which suggest that these eruption types are generated by distinct sources [86]. Two main types of products are erupted during the explosive activity [35, 9]: a high-porphyritic (HP) magma, consisting in degassed scorias with high crystal content (>45 vol.%) and a low-porphyritic (LP) magma, with crystal <10 vol.%, and a relatively higher volatile content.

Francalanci et al. (1999,2004) have shown that HP magma is derived from LP magma through a continuous process of plagioclase, clinopyroxene and olivine crystallization. The two magmas have in fact the same bulk composition but different crystal content and groundmass composition [37, 36]. All HP products erupted from Stromboli in the past decades have a virtually constant basaltic (shoshonitic) composition associated with poorly variable crystal content ($45-55wt\%$) [57] and small volatile content $< 1wt.\%$ [56]. The HP magma, feeding the normal Strombolian activity, resides in a shallow degassed reservoir, located within the volcano edifice [69, 68, 36].
The knowledge of the characteristics and dynamics of the feeding system significantly increased during the last decade trough the study of the products erupted during paroxysms [56, 69, 68, 36, 35]. Paroxysmal and major explosions show content evidences of low-porphyritic magma (LP) coming up from the lower part of the feeding system, mingled with high-porphyritic (HP) magma resident in the shallow part of the magmatic system (Fig. 4.1). The LP magma resides in a ponding zone vertically extended between 11 and 7 km below sea level whereas HP magma is mostly confined in the upper part of the feeding system, basically coincident with the volcanic edifice base. Both reservoirs are thought to be separated by a cumulative body (crystal mush), the evidences of which are represented by xenocrysts recording complex zoning and dissolution surfaces related to repeated interaction with the ascending LP magma [68]. To date, magmas with intermediate characteristics in

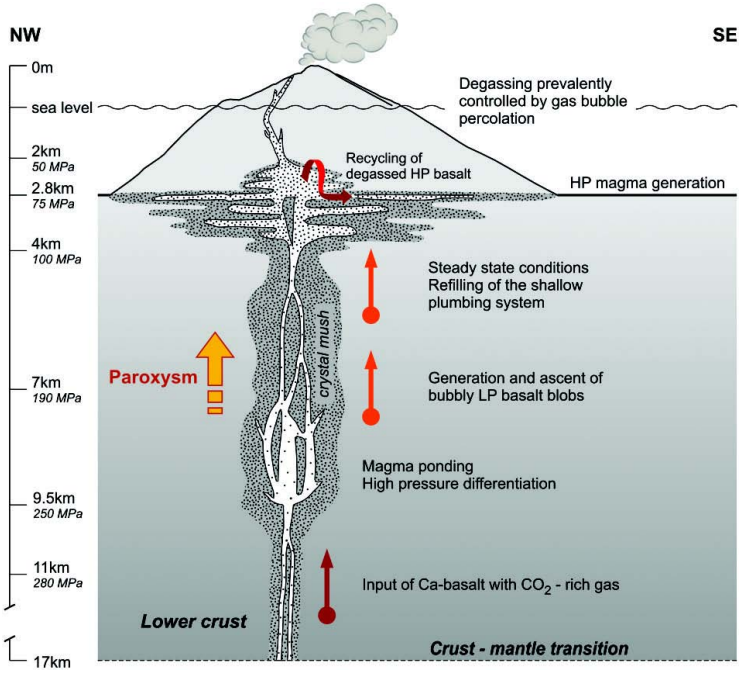

Figure 4.1: Interpretative model of the plumbing system of Stromboli volcano, from Métrich et al, 2010 [68]

term of crystal content and/or matrix composition have been only rarely found in the erupted products. These products seem to be a prerogative in Major explosions [56] and their characteristics prove a very rapid interaction between the two mag-

mas. Recently *Pioli et al., 2014* [86] analyzed several products from Paroxysmal and Major explosions showing that, in general, the intensity of eruptions seems to be related to the content of LP magma, thus suggesting that this kind of magma plays a role in the fragmentation mechanism for these phenomena, while the HP magma erupted during major and paroxysmal events is mostly passively ejected.

4.1.2 Explosion source mechanism

Two different models have been proposed to explain the dynamics of Strombolian explosions: the *rise-speed dependent model* and the *collapsing foam model* [78]. Both involve generation, rise, and burst of a large, conduit-filling, gas slug. In the rise speed-dependent model, first proposed by *Wilson* (1980), the slug formation is generated by the diffusive growth and cohalescence of bubbles due to the low rise-rate of the magma [116, 79]. The foam-collapse model instead requires a sort of restriction of the conduit where the bubbles are trapped and, after a certain volume is reached, collapse forming the slug [49, 50]. In the last two decades the two models have been examined and tested from geophysical records trying to find consistent explanations for their field observations. A first geophysical evidence for the rising-slug process, common to both models, was found after the introduction of the STS-1 broad-band seismometers [33], as they revealed the presence of a previously unobserved signal related to the explosive events at frequencies below 0.3 Hz. These Very Long Period signals seemed to be consistent with the generation and rise of a gas slug inside the upper conduit [90, 23]. The VLPs, due to their very long wave-lenght and a polarization pointing to the source, allow a precise source location [72, 54, 23, 61]. The VLP source position, relatively stable over time, shows two main clusters of locations, associated with the activity of the SW and NE craters, respectively [23, 61]. The high frequency component of the explosive-related seismic signals is instead well coupled with the infrasonic records [89, 90], and thus explainable as generated by the bursting of the slug at the free surface [112, 113]. The over-pressured gas slug breaking at the free surface of magma column, produces the force needed to eject magma into the atmosphere. Photoballistic approach was used at first to measure velocities of ejecta [19, 99]. More recently, thermal cameras [81, 30] and high-speed camera [107, 39] allowed a more accurate tracking of particles and gas ejecting velocities promoting the understanding of the explosive dynamics.
Finally, the ground tilt recorded during ordinary phases, reveals that the explosive process is accompanied by a persistent deformation of the ground detected as small inflation-deflation cycles associated with the constant process of gas recharge and discharge of the magma conduit, thus suggesting a process of accumulation and release of gas acting into the shallow magmatic system [38].
To date, the integrated geophysical approach [45] seems to represent the most promising way to further exploring shallow conduit dynamics and the mechanisms at the base of the explosive activity.

4.2 Scale of explosive activity

The classification of Strombolian explosive activity in Ordinary, Major and Paroxysmal explosions has been mainly based on the magnitude of the events and par-

ticularly for the possible impact on hazard assessment for the inhabitants [6]. The term "small-scale" was also introduced by *Metrich et al. (2001)* [69] and *Landi et al. (2011)* [57] to discriminate between Major and Paroxysmal explosions, always in relation to their possible impact on regularly inhabited places on the island.
A more quantitative approach is based on the mass ejected. As already discussed, the three types of explosive events differs by the amount of the erupted gas/magma. The ejected masses may vary from 10^3 kg for ordinary explosions to 10^7 kg for Paroxysms, with intermediate values of $10^4 - 10^5$ kg for Major events. According to *Pioli et al. (2014)*, during the period 2003-2013, the Stromboli erupted $3.3 \times 10^9 kg$ of magma during ordinary explosions, $7.14 \times 10^6 kg$ with Major explosions, and $6.29 \times 10^7 kg$ for Paroxysms (as averaged values) [86]. These values, although indicative, clearly demonstrate the limited volume of magma involved in more energetic events with respect to those in the regular activity.

4.2.1 Towards a geophysical classification

Geophysical observations have been used extensively to evaluate the energy involved in the volcanic explosions [e.g [63, 76]]. It is not surprising that amplitudes of detected signals provide information on the size of the phenomena as well as the "shapes" of the signals disclose the dynamics of the processes. Hence, obviously enough, one may suppose that different volumes involved in the three types of events will produce geophysical signals with different magnitudes and/or durations. *Marchetti et al.* (in preparation), analyzed the geophysical scaling of the Strombolian volcanism in terms of seismic, infrasonic and tilt changes. Here we limit our analysis to the two parameters that better relate to the mass/volume/pressure changes into the magmatic conduit (thus resulting more promising for the geophysical discrimination of the three classes of events): seismic ground displacement (VLP) and ground tilt.
It is worth noting that these two parameters are not fully independent but both outcome from the deformation field produced by one or more sources in the shallow magmatic system. The understanding of these sources, their position, size, and time-history is then essential to the comprehension of the explosive process and to avoid misleading interpretations.

In figure 4.2, the VLP and tilt amplitudes for more than 5000 ordinary explosions, 29 Major events and the March 15, 2007 Paroxysm are plotted together. Blue lines mark the proposed limits between Ordinary and Major explosive events. VLP max amplitude is measured as peak to peak amplitude of VLP displacement in the 0.033-0.8 Hz frequency band. Tilt amplitude is instead referring to the maximum tilt recorded during the event respect to a baseline defined as the mean tilt amplitude trace between 500 and 300 seconds before the event. The Ordinary events were manually picked among a few hundred of thousands that better represented the full amplitude range of the regular activity. Since 2006, the seismic VLP events are in fact manually picked on a daily basis for the compilation of daily reports for the Civil Protection. Stored event times were used to automatically pick the events from seismic and tilt traces. For each event a 1800 seconds-long window, centered on the event, is extracted. Data are integrated to displacement, band-pass filtered, accurately aligned using local-maximum finding procedure, and finally the

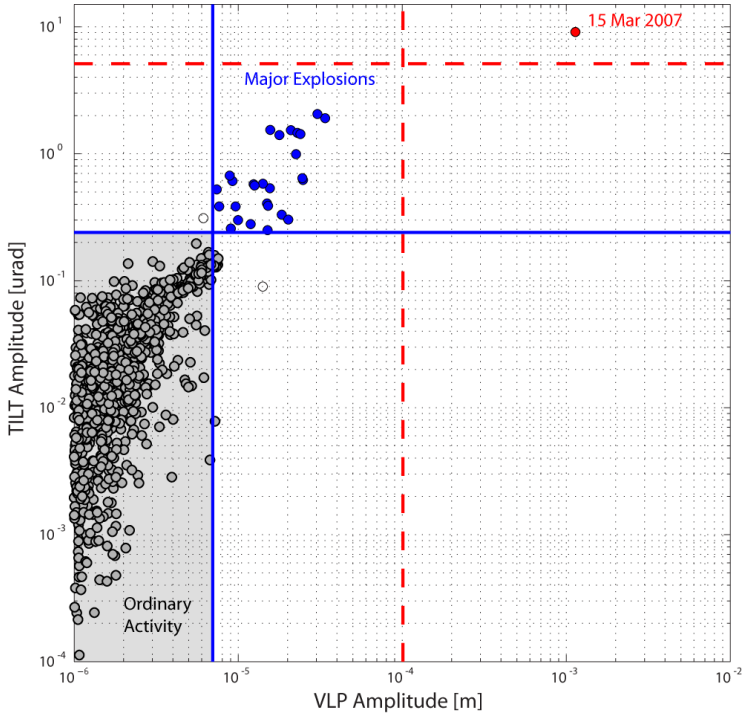

Figure 4.2: Amplitude distribution for ordinary (gray), major (blue) and paroxysmal(red) explosions expressed in terms of seismic VLP displacement and ground tilt. Blue lines define the limits of ordinary explosive activity whereas red dashed lines approximately divide major and paroxysmal.

amplitude is computed, in a 60s window around the center.
Despite that the number of plotted events is relatively small, the limits between ordinary and major activity clearly emerges from the graph. Although there is no energy gap between the two classes, and the choice of a precise threshold could be questioned, the meaning of this graph is to provide a quick and useful way to discriminate the two type of events, based on a minimum number of geophysical parameters. Among the others, ground tilt and displacement have the advantage to be reliable as not affected by weather limitations such as visibility for thermal imagery and wind conditions for infrasound pressure records. Moreover, as already discussed, displacement and tilt both indicate a pressure (or volume) change inside the shallow magmatic conduit [38, 23], which is expected to directly correlate with the amount of gas and magma released.

4.3 2003-2015: paroxysms and major explosions

Since the installation of the LGS permanent geophysical network, in 2003, the volcano experienced three main effusive phases: 2002-2003, 2007, and 2014. The first two were characterized by paroxysmal events, on Apr. 5, 2003 and Mar. 15, 2007. In this several-years-long time window, the regular Strombolian activity, producing $\sim 10^6$ ordinary explosions, was punctuated by sparse Major events (Fig. 4.3). In the following sections all the 33 events recorded since August 2005 (When OHO

tiltmeter become operative) will be analyzed. Before this date, 6 more events described as Major were reported on: Sep. 16, 2004; Dec. 7, 2004; Dec. 9, 2004; Dec. 24, 2004; Jan. 9, 2005; Apr. 9, 2005, respectively. These events will not be analyzed since OHO tiltmeter was not yet installed at that time and we do not have a complete and fully-comparable data-set. The small number of events, specially

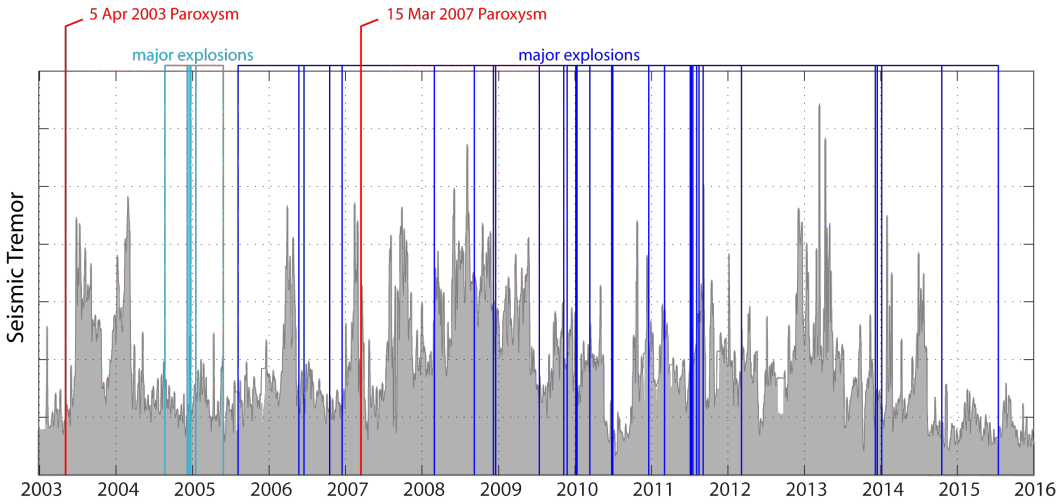

Figure 4.3: Timeline of Paroxysmal and Major events recorded at Stromboli between 2003 and 2015.The red lines mark the Paroxysms while blue lines indicate Major explosions. The events before Aug. 2005, marked in light blue, devoid of the tilt data.

when compared to the regular explosive activity, prevents from a reliable statistical analysis. However, as a purely indicative information, during 13 years (2003-2015), 39 Major explosions and 2 Paroxysms were recorded. This provides a mean ratio of 3 Major events per year and a Paroxysm every 6.5 years. In contrast, several events seem to be clustered in short periods such as in Dec. 2004 - Jan. 2005, Dec. 2008, and Jul-Aug 2011, when the inter-time between event reduces to days/weeks. It is also noticeable that both the two paroxysmal events occurred during major effusive phases. For Stromboli's historic activity at least two patterns of behavior have been recognized: (i) paroxysms followed by lava effusion, and (ii) lava effusion followed by paroxysms [6, 83]. In our recent geophysical record, we only have represented the first pattern.

4.4 Major Explosions

The list of Major events during the analyzed interval (2005-2015) is reported in table 4.4. Beside the occurrence time, also seismic VLP displacement, seismic velocity and tilt amplitudes are there reported. A total of 33 Major explosions, consistent with the proposed geophysical classification, is reported. Far to be an homogeneous group, the Major explosions differ from each other reclaiming an individual process. Similarly to the typical Ordinary explosions, the modality of gas and fragment release from the vent can significantly vary for its duration, intensity, amount of load, exit velocities and source crater.

4.4.1 Events description

Three events among the 33 have been chosen to represent the different styles of ejection observed for Major events. Far to be exhaustive, this choice was motivated with the aim of simplify and clarify. The main difference between two Major events is represented by its time history. While some are characterized by a single "cannon-like" explosion, others rather manifest the occurrence, in a short lapse of time (from seconds to tens of seconds), of multiple gas/fragments emissions. Only in a few cases this activity involve multiple craters. In figure 4.4, a series of frame-shots from ROC thermal camera relative to the Major event of Dec. 06, 2008 is reported. The single frames are spaced in time by 1 second. The explosion, located at the Central crater, consists in a single, violent ejection creating an hemispherical shaped plume, with finger-jets formed behind faster ejecta. The second event (Nov. 9, 2008), depicted in figure 4.5, shows a slightly different pattern. A first violent, ash-rich ejection, as evidenced by the dark colored, relatively cold plume, is shortly followed by a second, more energetic and incandescent magma-rich explosion. Finally, figure 4.6 represent a last type of event (May. 3, 2009), where a first ejection is followed, after $\sim$10 seconds, when the first explosion already developed its plume to buoyancy state, by a secondary, and much larger event with an hemi-spherically shaped incandescent plume. The end of the explosive phase is then accompanied by the formation of a sustained gas jet from the vent. Note that in the last image sequence, the inter-time between successive frames is increased to 2 seconds. All the three events were located at the Central vent and occurred in a relatively short time interval, from November 2008 to May 2009. During this period major changes in the crater terrace topography were not recorded. These events, differing in duration, amplitude and ejection dynamic, were chosen also to demonstrate that the same crater may produce different style of events. Two of the tree events were followed by a long lasting (several minutes) phase of sustained degassing. With minor changes all the events present similar characteristics of duration, intensity and dynamic.

4.4.2 Event location and crater terrace morphology

The crater terrace morphology changed over time by constructive periods, with continuous accumulation of new material, or destructive events, such as paroxysmal explosions and crater collapses. Three distinct zones, however, have been always maintained, a SW, a Central and a NE one. Each zone presents one or more vents that may produce similar or different types of Ordinary explosions and/or over-pressured continuous degassing (puffing). Degassing, can be stable at a single vent or temporary shifting to another vent. Moreover, it is also occasionally observed at two vents simultaneously. Over the years the "typical" style of each crater repeatedly change, preventing from a decidec definition for a reference type of activity. Apparently, during the analyzed period, Major events were observed at all the three craters.

Major explosions were accurately located using thermal images acquired by ROC and GST *FLIR A-20* cameras and the infrasonic array locations, allowing distinguishing which crater was active. Such source vent positions, are reported in table 4.4. In figure 4.7 the vent distribution for 32 over 33 major events is displayed. For two events (Aug. 5, 2005 and Dec. 17, 2008) the source is not accurately deter-

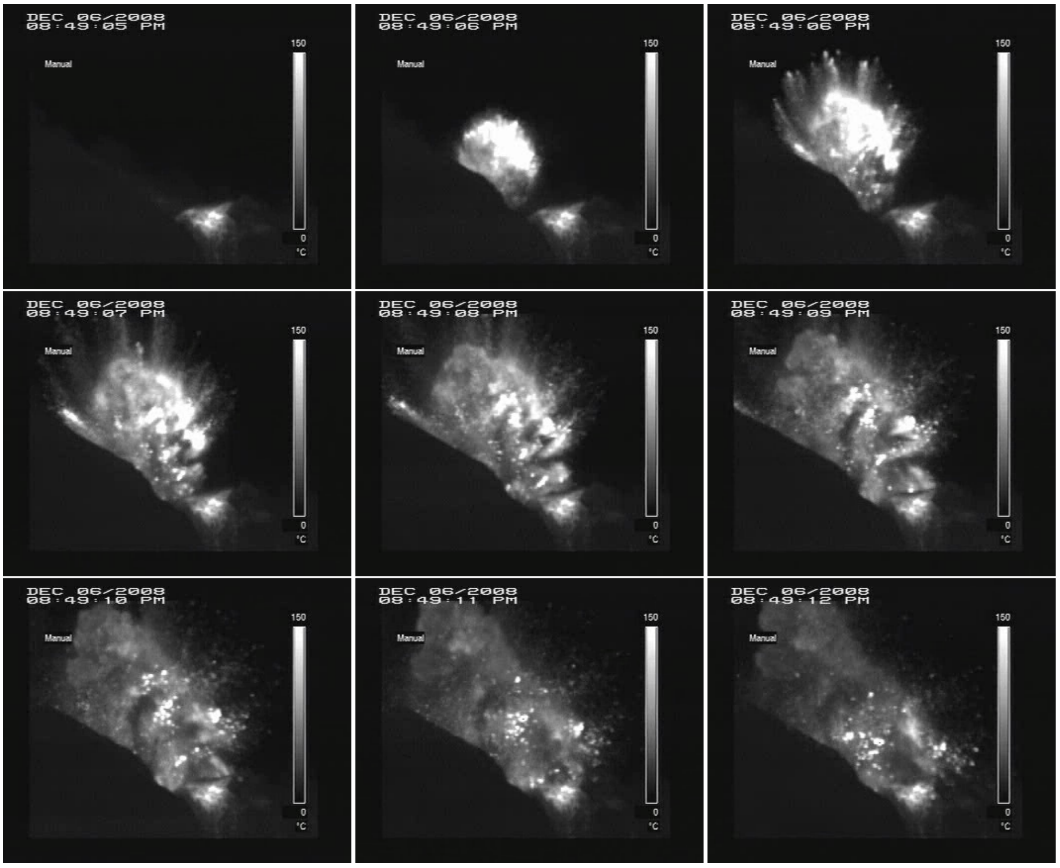

Figure 4.4: Major event of Dec. 6, 2008. Frame-shots from ROC (FLIR A20) thermal camera. Each frame is separated by 1s. First frame (left-high corner) shows the crater profile less than 1s before the event. Note the hot material around NE crater vent. Event consists in a single violent, round shaped plume emission from Central crater. Note high-velocity ejecta with finger-jets formation.

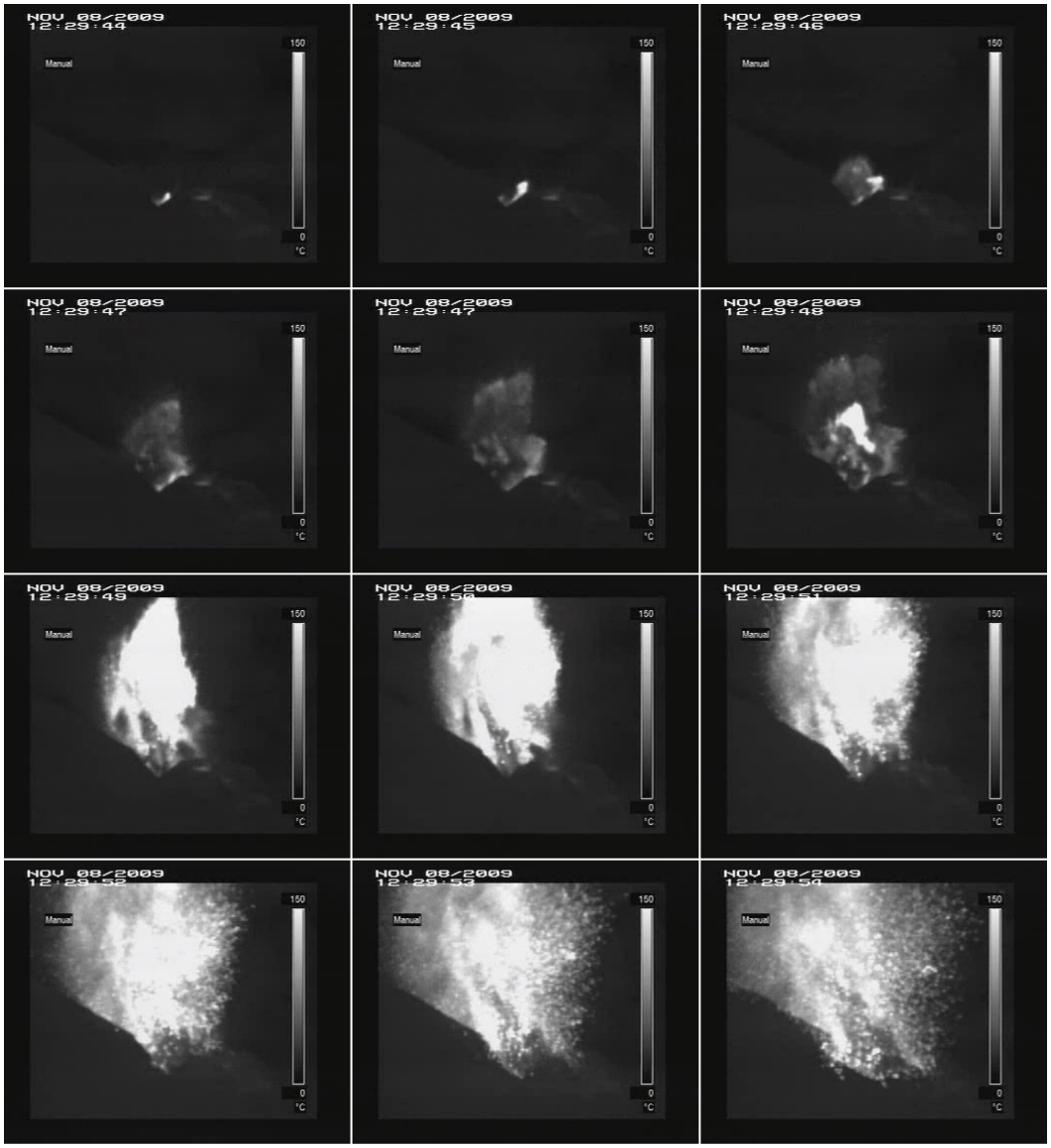

Figure 4.5: Major event of Nov. 8, 2009. Frame-shots from ROC (FLIR A20) thermal camera. Each frame is separated by 1s. The first ash-rich emission from Central crater is shortly followed by a second, more violent explosion with incandescent material

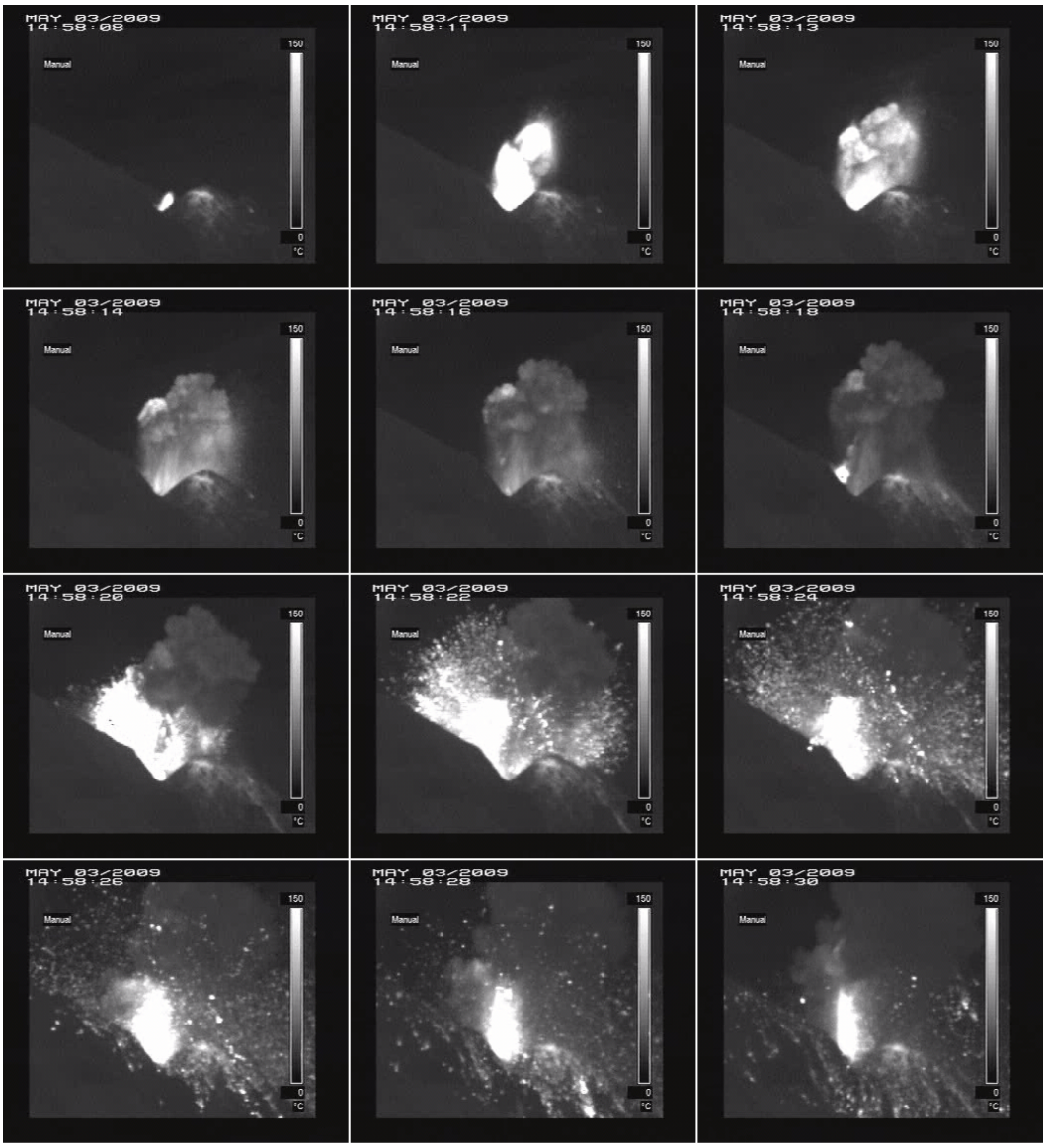

Figure 4.6: Major event of May. 3, 2009. Frame-shots from ROC (FLIR A20) thermal camera. Each frame is separated by 2s. A first violent emission is followed, after a few second (Note the formation of buoyant and the ash-fall) by a second more energetic and magma-rich emission, both from central crater. Finally a long lasting phase of sustained gas emission is developing (last two frames)

mined. Those events are removed from graph. The histogram of eruption for each

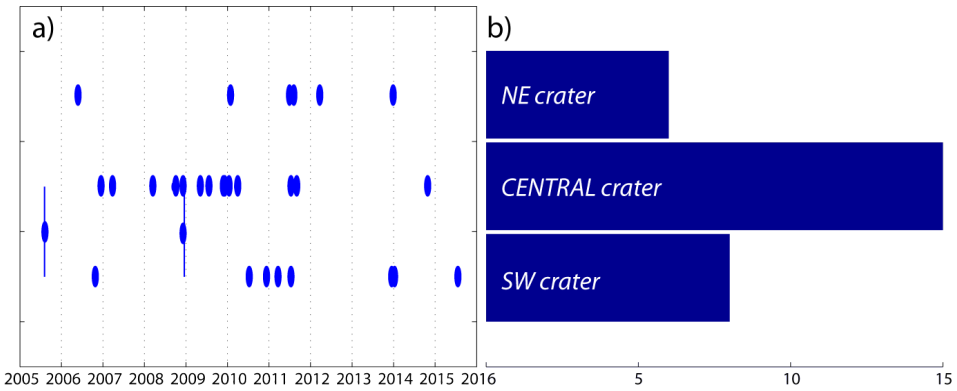

Figure 4.7: Source vent location of major events recorded in 2005-2015 period. Time distribution is reported in (a). The two events on Aug. 5, 2005 and Dec. 17, 2008 are marked with line due to the not precise vent location. In (b) the vent distribution is shown. The two not well constrained event are not counted.

crater (Fig. 4.7b) shows how the Central crater dominates amongst the three, producing alone more than the total number of events recorded on both the SW and NE craters. The time distribution of the events (Fig 4.7a) however, evidences how this privileged activity of the Central crater as source of Major explosions was mostly dominant in the 2008-2010 period, when almost all the events were confined to this position. It is worth noting that this location is also consistent with the position of the dominant source of puffing during the 2005-2009 period, as reported from *Landi et al.* (2011) [57]. On the contrary, during the preceding and following periods, the major activity spans from side to side of the crater terrace. The analysis of the infrasonic degassing activity did not evidenced clear correlation between the source crater of major explosions and the dominant puffing source.

4.4.3 Geophysical characterization

The effectiveness of seismic VLP and tilt data to discriminate between Ordinary and Major/Paroxysmal explosions has been already introduced. However more information can be retrieved from geophysical data (Fig. 4.8). In figure 4.9, 20 samples traces from STR U/D component are reported. Traces are 1800 seconds long and centered on Major events. The misalignment between traces is appositely set to provide better legibility. Differences in amplitude, duration and shape are easily observed. The occasional presence of a long coda indicates the occurrence of a long-lasting degassing phase after the end of the explosive event. When seismic velocity amplitudes and VLP displacement amplitude are compared (Fig. 4.10), the two parameters do not always show good agreement. This is probably due to the fact that the seismic velocity signal, or *explosion quake*, is more sensitive to the ejection dynamics than the VLP component. This is also consistent with the high variability retrieved in infrasound pressure values associated to Major events. Infrasonic data, in fact, show that the over-pressure at the vent can vary significantly, sometime even not exceeding the typical values or ordinary activity. Infrasound data are not discussed in this work. The infrasonic network was continuously developed over the

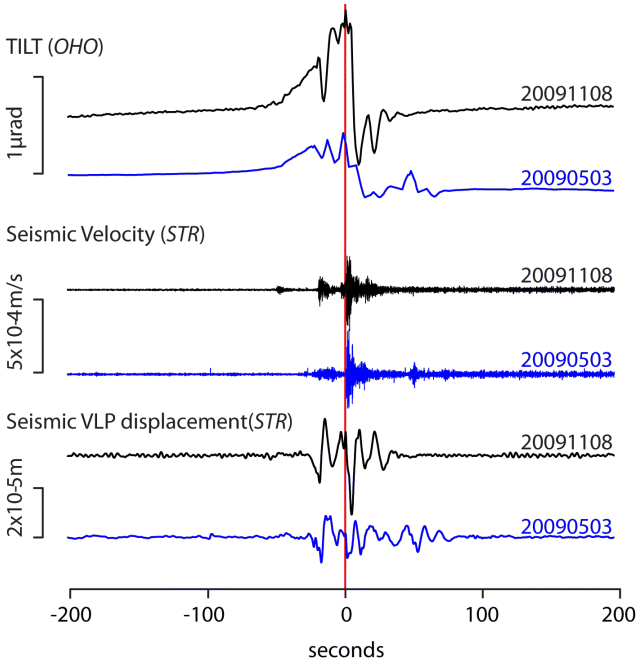

Figure 4.8: Tilt, seismic U/D velocity and seismic U/D VLP displacement, 400 seconds long traces for two Major explosive events. Tilt and seismic traces are extracted from OHO and STR station, respectively. Red line marks the onset of explosive event.

last years, and sensors often changed during an uninterrupted improvement process, which makes harder the comparison between events recorded during different periods. Tilt data (fig. 4.11) reveal an inflation phase preceding each Major explosion. The ground inflation, starting up to 300 seconds before the onset of the ejection, and with amplitude largely contributing to the total signal amplitude is one of the most significant characteristics of Major events.

4.4.4 A simple pattern for complex events

The inflation phase preceding the onset of the explosive events is probably the most representative geophysical signature for this class of events. Clearly rising from the background level of ground deformation related to the regular explosive activity, it reveals a progressive increase of pressure into the shallow magmatic conduit. Despite the complexity of the explosive phase, presented in the precedent paragraph, tilt signal seems to always follow a well shaped pattern differentiating only in the last tens of seconds. A few hundreds of seconds before any visible sign of the explosion, tilt gradually increases, constantly accelerating over time. If traces from different events are aligned according to the explosive onset (Fig. 4.12), the self similarity of the inflation phase becomes clearly evident. All the recorded events, in fact, follow the same inflation pattern. The stacked trace, resulting from the averaged pattern of original traces better evidence the duration of tilt inflation (Fig. 4.12b), starting at least 500 seconds before the visible explosive onset, whatever the size of the explosion is. The similarity of tilt traces indicates that, despite the different pattern observed for the at-the-surface explosive phase, the preparatory stage of

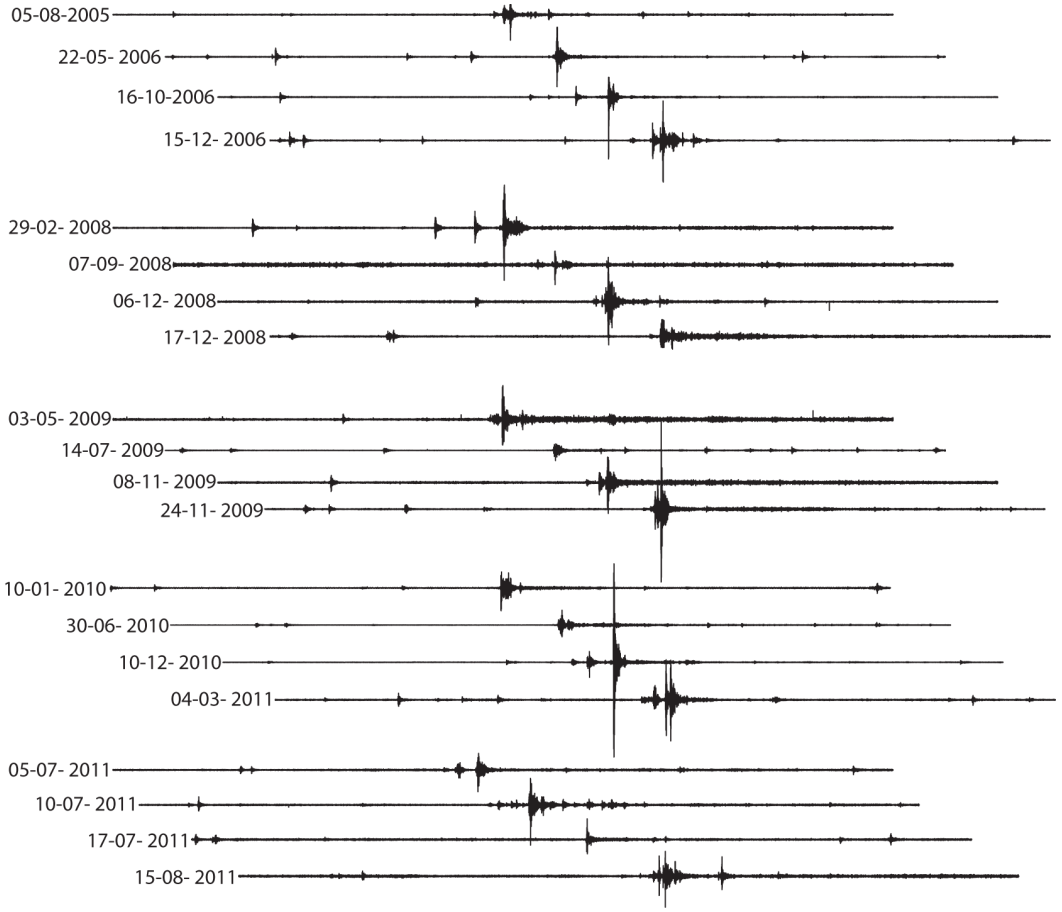

Figure 4.9: Sample of 1800 seconds-long seismic velocity raw traces (U/D component) for 20 major events. Relative amplitude is maintained. Traces are appositely misaligned to better distinguish the events.

Major events is instead dominated by a common dynamic process of accelerating ground inflation (Fig. 4.12). The unfiltered signal 4.8, include the complexity of emission phase as VLP signals. When low-pass filtered (below 20s), these VLP components are reduced in amplitude while the long-lasting inflation phase remains unaltered with respect to raw trace.
This process, continuously evolving over hundreds of seconds, leads to its mandatory conclusion, represented by a violent gas and magma emission at the surface, that is then recorded as infrasound pressure transient, seimsic explosion-quake and thermal plume evolution. The explosive onset is followed by a sharp decompression of the system, lasting 10-30 seconds and associated to the ejection phase.

4.5 Paroxysms

Two paroxysmal explosions have been recorded since the installation of the LGS integrated geophysical network: the first event on April 5, 2003 and a second one on March 15, 2007 (Fig. 4.3). Both the events have been described and analyzed in details in literature for the temporal evolution of phenomena, geophysical data,

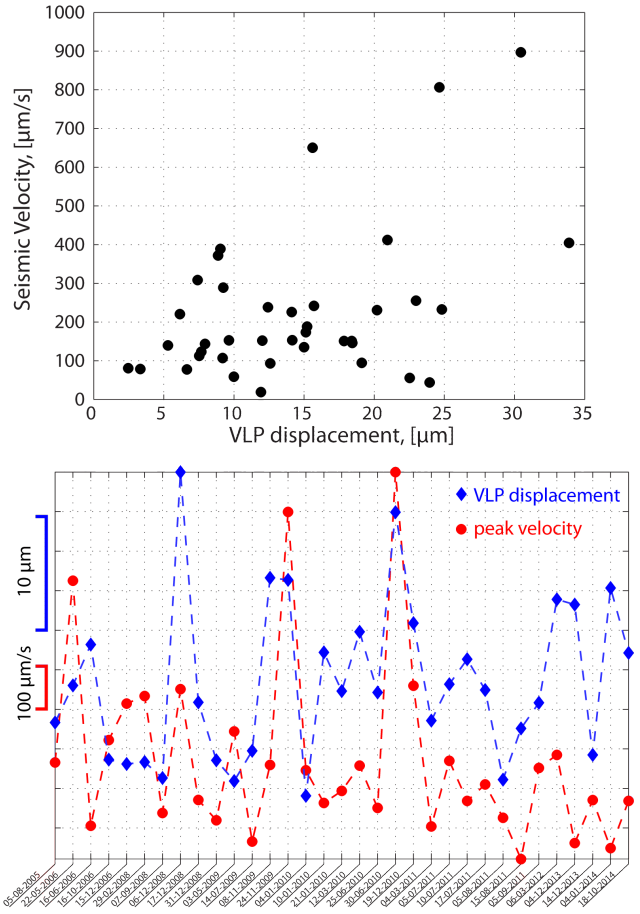

Figure 4.10: Comparison between seismic peak velocity and seismic VLP displacement (0.033-0.8 Hz, see text for details) as reciprocal plot (up) and normalized (down).

products and source modeling (e.g. [84, 2, 103, 16, 87]). Here the analysis will be limited to those parameters not discussed yet in the previous works. Along with a brief introduction of the two events and the related geophysical data-set, a qualitative analysis of the ground deformation data will be introduced. As evidenced by Major events analysis, the ground deformation pattern can in fact disclose new insights on the dynamical processes preceding and accompanying the event to its epilogue.

The geophysical data-set provided by the LGS network is not identical for the two events. Between the two eruptive crises in fact, the configuration of the network, in terms of number and type of instruments, significantly changed. At the time of the first paroxysms, the clinometric network was not yet deployed, while on 2007, two of the three stations (LSC and OHO) were already operative. Another important difference was about thermal data. The first thermal camera (at ROC station) was only installed on 2005. Pressure sensors used for the detection of infrasound waves also improved over time from simple electret microphones (before 2007) to differential pressure sensor. For all these reasons, the data-set of the two events significantly differs by completeness. In figure 4.13, a sample integrated data-set for the two paroxysmal events is shown. Note how the strong ground motion saturated

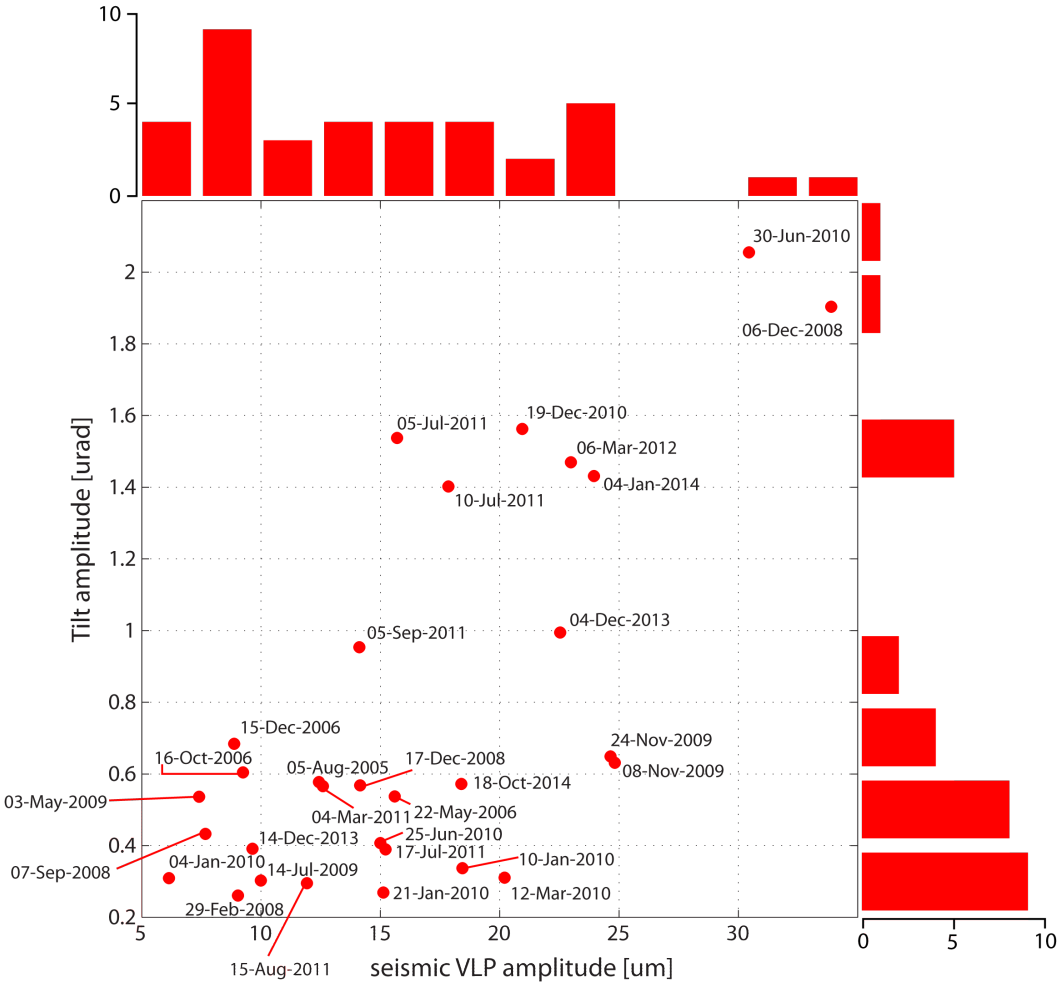

Figure 4.11: Reciprocal plot of Tilt amplitude vs. VLP displacement amplitude. Dates of events are also displayed. The two histograms on top and on the right represent the frequency distribution of amplitude of tilt and VLP.

the seismic traces. Even if thermal camera was not yet installed in 2003, an infrared thermometer was already placed at ROC, allowing the collection of the thermal integrated data displayed in figure 4.13. Thermal records are included in the displayed data-set as they provide the easiest way to mark the explosive onset.

The April 5, 2003 Paroxysmal event The Apr. 5, 2003 paroxysm has been described in detail by *Rosi et al.* (2006) [103]. From the examination of visual records, the authors split the event in four phases: *i) eruption onset, ii) climatic explosion, iii) pyroclastic flow and smaller explosion, and iv) terminating ash explosions*. The explosion began at 07:13:07 GMT with a relatively weak emission of red ash from Central and SW vents (phase i), shortly followed (07:13:19 GMT) by the ejection of a fast growing, dark colored ash plume and a few seconds later by a second violent emission with blocks and multiple jets (phase ii). Plume is estimated to rise ∼4 km above the summit [16, 103]. About 250 seconds after the onset of the eruption, a strong degassing activity with several smaller explosions started, lasting until the

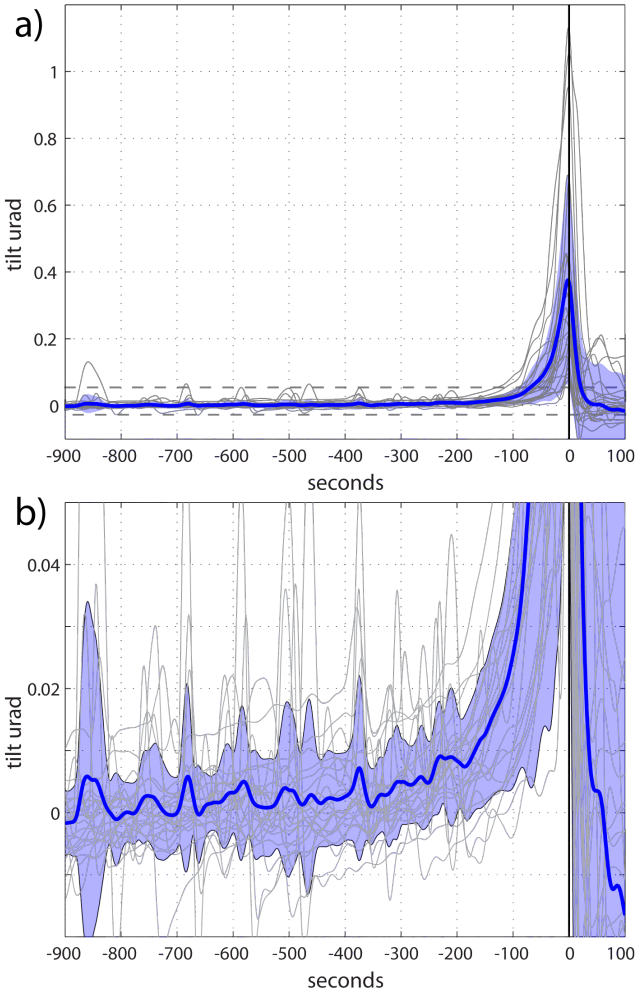

Figure 4.12: 1000 seconds long tilt traces for all recorded tilt signal during Major explosive events (a,b). Traces are aligned with explosive onset based on thermal imagery and infrasound detections. Gray colored lines represents single events. Blue line is the stacked trace and light blue patch is the standard deviation respect to mean stacked trace. Amplitude scale is maintained. All traces are low-pass filtered below 10 seconds. Dashed lines in (a) mark the vertical extension of sub-plot (b). Black vertical lines indicate onset time of explosive events.

end of the explosive phase at 07:20:54 GMT [103]. In total the eruption lasted about 8 minutes, producing 1.1-1.4 $\times 10^8$kg of fall-out mass [86].

The March 15, 2007 Paroxysmal event The paroxysmal eruption of March 15, 2007 started at 20:38:14 GMT and lasted about 5 minutes. The eruption generated a densely loaded ash plume rising up to 3 km above the craters. Activity can be divided in three distinct phases. i) a first pulse started at 20:38:14 GMT with a fast-rising jet of hot material and blocks from the NE sector; ii) a second vertical jet observed at 20:38:36, lasting about 12 seconds, generating a 3 km high plume; iii) a final phase, after 20:41:33 GMT, of intense but low pressure sustained degassing [87]. The deposit of the explosive event indicates a total erupted mass of 2.2-2.7

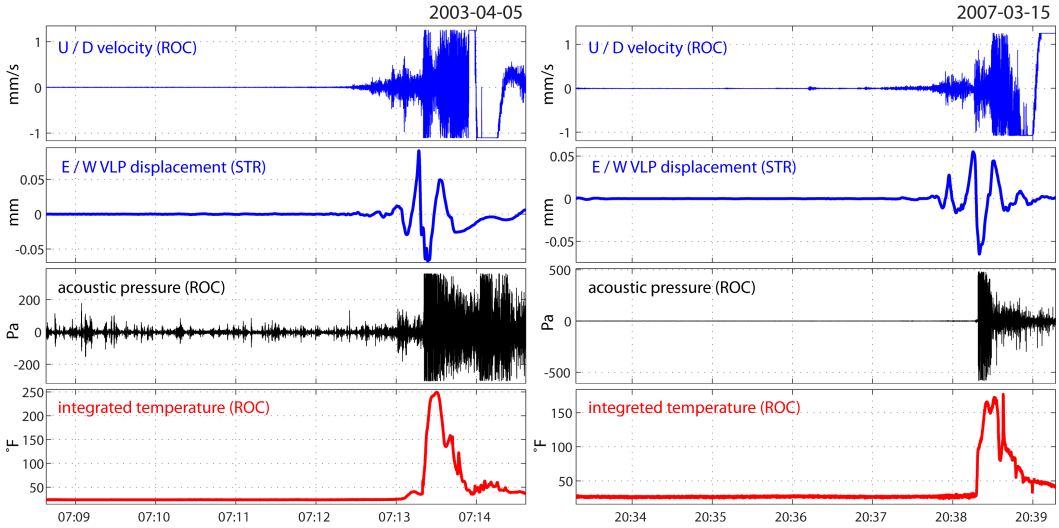

Figure 4.13: Comparison between Apr. 5, 2003 and Mar. 15, 2007 paroxysmal explosion data-sets. Seismic velocity, VLP displacement, infrasonic pressure, and integrated temperature are reported. Seismic traces are saturated due to very strong motion exceeding the limited excursion of the 16bit digitizer.

$\times 10^7$ kg [86].

These two paroxysmal events, partially different for their intensity, duration and erupted mass, also show a relatively different evolution over time. In any case, for both of them multiple pulses can be distinguished and summarized: a first phase constituted by the ejection of large blocks, followed by the main ejection phase with the formation of the main plume; a long-lasting terminal phase characterized by sustained degassing with a few lower amplitude explosive events conclude the eruption. Concerning differences, the Apr. 5 event was heralded by a sustained jet emission from the vents, while the Mar. 15 paroxysms onset was apparently abrupt. This is clearly visible in Fig. 4.13, where infrasound pressure and thermal signals evidence this difference. In general, as in the case of Major explosion, the explosive dynamic observed at the surface seems to show complexities and over-imposition of multiple events and phenomena, each one contributing to the geophysical signature of the event. The integration of geophysical data-set allowed the authors to characterize the event about timing, explosive dynamics and to suggest some inference on the shallow magmatic system and even the source process [84, 16].

4.5.1 Ground deformations

Tilt data are only available for 2007 paroxysm since during 2003 eruptive crisis no tiltmeter was yet installed on the summit region of Stromboli volcano. Tilt data from March 15, 2007 paroxysm have been extracted and processed (Fig. 4.14. The paroxysmal event produced a strong deformation signal which was clearly detected by both the LSC and OHO stations as a first inflation phase suddenly reversing into deflation as the explosive event starts (Fig. 4.14a). The shape of the signal, initially almost identical (except for the amplitude), start to differentiate about 30

seconds before the explosive onset. The inflation phase starts ∼500 seconds before the explosive onset, and reach a peak value of ∼9 μrad at OHO station just before the explosive onset. Four phases can be distinguished on the base of the comparison between OHO and LSC traces and tilt signal polarization: i) first phase, starting ∼500 seconds before the explosive onset (white background in Fig. 4.14a) which is characterized by an analogous inflation signal recorded at both tiltmeters; ii) a second phase, (20:37:51 - 20:38:18) about 30 seconds long (light gray background in 4.14a), where LSC tilt records an abrupt increase of the inflation rate; iii) a third, co-explosive phase (intermediate gray) when signal revert to deflation at OHO station while remains stable at LSC (20:38:18 - 20:38:44); iv) a last phase when both tiltmeters records ground deflation (20:38:44 - 20:40:00). The analysis of the tilt vector polarization (Fig. 4.14b,c,d,e), shows that during this inflation phase (Fig. 4.14b) tilt direction is consistent with a linear source such as the dike modeled by *Marchetti et al.* (2009) [60] for tilt data relative to the 2007 effusive eruption. This parallel polarization is also almost maintained during the second interval (Fig.4.14c), when tilt vectors becomes slightly convergent. The third phase also share the same polarization, but with inverted sign (Fig. 4.14d). The last, deflationary phase in instead characterized by a drastic change of polarization at LSC mainly due to the behavior of its tangential component (Fig. 4.14a) that experience a strong tilt change (40 μrad). At the end of the explosive phase, a permanent tilt step is observed. The scarce number of stations (only two tiltmeters, LSC and OHO), and

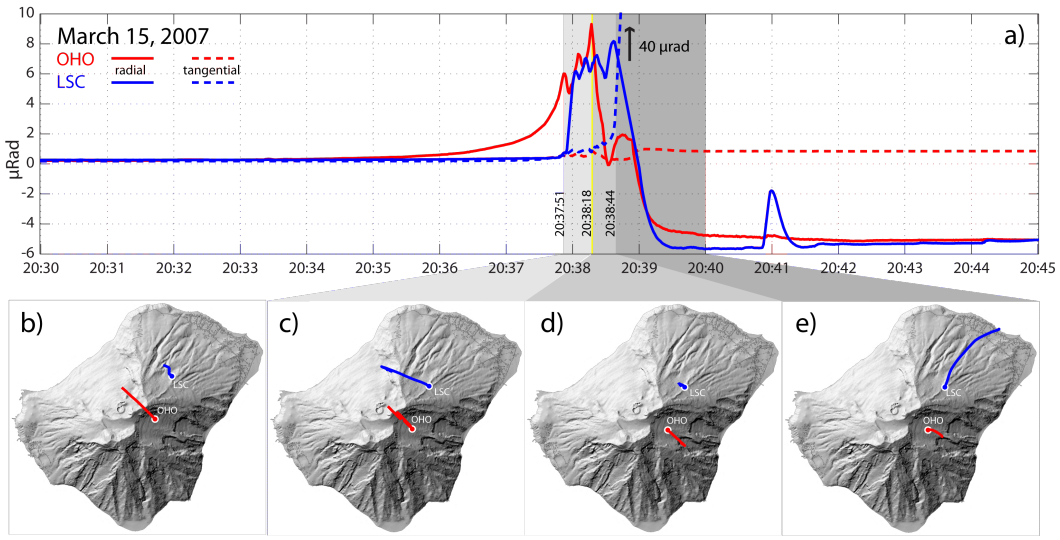

Figure 4.14: a) Tilt traces at LSC (blue) and OHO (red) stations for both radial (continuous) and tangential (dashed) components. Yellow line mark the explosive onset at 20:38:18. b,c,d,e) Maps of Stromboli with tilt station positions (circles) and trajectories indicating tilt vector polarization for the pre-eruptive inflation phases (b,c) and co- and post- eruptive deflation phases (d,e), see text for details.

the complex behavior during this event, prevents from a reliable source inversion. Hence the following observation are limited to qualitative considerations. For a static source, no changes in amplitude ratio between the stations are expected. The observed behavior implies a change in the source position or in the source shape.

The change in amplitude ratio between the two instruments could than reflect the temporal activation of different source regions inside the magmatic conduit. It is worth noting that the pattern starts to diverge about 25 seconds before the explosive onset and terminates 25 seconds after the explosive onset. Tilt recorded at OHO station was about ten times larger than the one recorded at LSC during the first phase, but suddenly LSC increases to a ratio close to 1 at the beginning of the second phase. This ratio was then maintained until the onset of the eruption, when tilt ratio (OHO/LSC)is about 5 for the sudden deflation and finally become unstable due to the large tilt recorded by LSC tangential component (Fig. 4.14a). These oscillations in tilt ratio are here suggested to represent the result of a pressure source migration into the shallower portion of the upper conduit in the very last moments preceding the event. The rapid dramatic inflation recorded at LSC 27 seconds before the explosive onset (second phase) seems to indicate the activation of a different source (or source portion) with respect to the precedent inflation source. Moreover, the delay between OHO station, which show a rapid deflation suddenly after the onset of the explosion, and LSC which starts its deflation only later, could depend on the different elevation of the two sites (third phase). While OHO is in fact at 570 m a.s.l. LSC station is instead placed at 520 m a.s.l. (crater terrace is about 750 m a.s.l.). The deflation recorded at OHO station as the eruption starts, is probably associated with the pressure decrease into the conduit due to the sudden ejection of gas and magma. As the fragmentation front descend into the deeper part of the conduit, also the lower station starts recording a deflation. While tilt data (or rather my personal capabilities!) are maybe not enough to explore in detail the emerging complexities of the source dynamics of this paroxysmal event, *Mattia et al.* (2004) [66] succeeded to model the rather complex behavior of the shallow plumbing system of Stromboli during the Apr. 5, 2003 Paroxysm, using high sample (1Hz) GPS data. Their results show how the explosive event was activating different portions of the system during its development.

4.5.1.1 Seismic-derived tilt data of April 5, 2003 event

While there were no tilt installed at the time of the 2003 Paroxysm, the LGS broadband seismic network was already fully operative. This provide a shortcut to retrieve some delayed information concerning ground deformations. Following *Genco and Ripepe* (2010), (see appendix A for details), tilt data have been extracted from seismic stations. At the time of the paroxysmal explosion, four broadband seismic station were operative (SCI, ROC, STR, and PZZ). Unfortunately, due to the very strong seismic signal, and the 16bit resolution of digitizers, the waveforms recorded are clipped (Fig. 4.13) at all the sites. This affects the procedure of tilt retrieval under two points of view: i) amplitude of tilt signal retrieved from seismic trace cannot be considered as representative of real amplitude of event; ii) the waveform of recovered signal is probably not fully consistent with the real one. These two limitations can be partially avoided if we only limit our observations to the part of the signal which precede the saturated part, discarding the following portion of time series. Since the velocity traces before the onset are not saturated we consider as reasonably representative the data-set until this point. Tilt signals derived from horizontal components of ROC and STR stations are drawn in figure 4.15. At

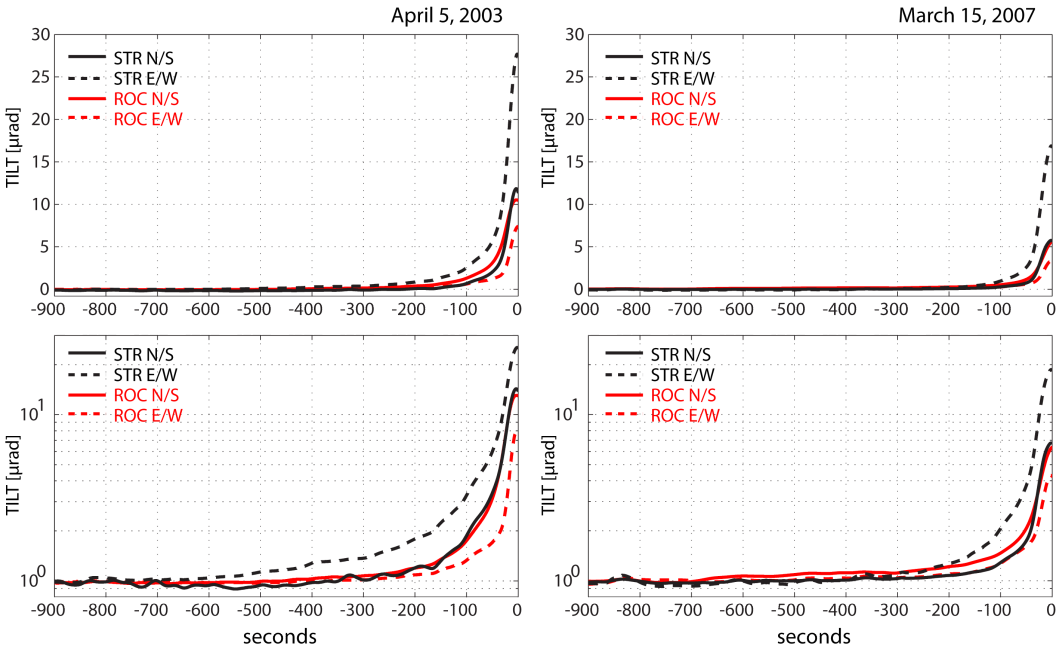

Figure 4.15: Tilt traces as derived from seismic sensors at STR and ROC sites for the two paroxysmal events on Apr. 5, 2003 and (left) and Mar. 15, 2007 (right). E/W component are represented with dashed line. Upper plots show the amplitude in linear scale while lower plots vertical axes are logaritmic to enhance the tilt inflation rate.

the two other stations (SCI and PZZ) traces are too noisy or too saturated to be successfully used in tilt retrieval procedure. The amplitude of tilt confirm Apr. 5, 2003 event as more energetic also in terms of ground deformations. Based on the linear regression of the four components amplitude, a tilt ratio of 1.5 between 2003 and 2007 paroxysms can be estimated (Fig. 4.16). According to this value, a tilt of 13.5 μrad at would have been expected at OHO site for the April 5, 2003 Paroxysms.

4.5.2 Ground deformation and erupted volume correlation

Retrieved tilt amplitude is only relative to the inflation phase which precedes the explosive event. It is reasonable to assume that ground deformation should be roughly proportional to the volume of erupted magma. According to *Pioli et al.* (2014) [86], fall-out mass for the two events are 1.1-1.4$\times 10^8$ kg and 2.2-2.7$\times 10^7$ kg for the 2003 and 2007 events, respectively. This give a ratio of $\sim$5 between 2003 and 2007 deposits. However, when only LP erupted mass is considered (5.0-10.0$\times 10^6$ kg and 5.05-8.20$\times 10^6$ kg) respectively, the ratio decreases to 1.1-1.2. These values are close enough to the 1.5 ratio found for tilt amplitude. Since LP magma decompression can be considered as the driving force of paroxysmal explosions, the ratio of LP erupted magma can be considered as more representative of the expanding/pressurizing volume responsible for ground inflation observed before the eruption. The substantial agreement between estimated LP mass ratio and recovered tilt amplitude seems to suggest that ground deformation observed before Paroxysmal explosions are representative of the volume of the rising LP magma batch.

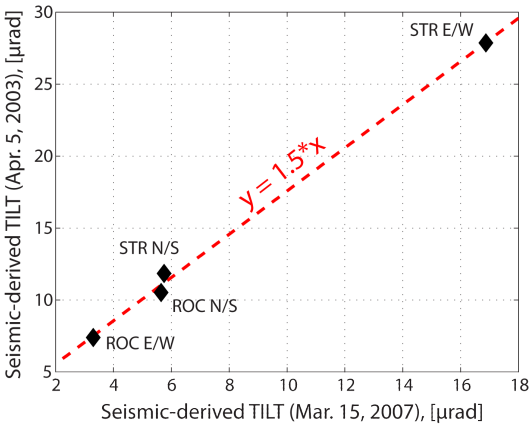

Figure 4.16: Seismic-derived tilt amplitudes from the E/W and N/S components of STR and ROC stations as recorded during 2003 and 2007 paroxysms. Red dashed line represent the result of linear regression.

4.6 Major and Paroxysmal explosions: A common dynamic process?

When ground deformation of paroxysmal and major explosions are compared, all the events reveal the same, common pattern of tilt inflation (Fig. 4.17). This common pattern, scalable in amplitude, is indicating a gradually increasing rate of pressure growth inside the magmatic conduit. Initial phase of pressure change can be detected at least 500 seconds before the explosive onset. This long-lasting precursory phase is evident in the case of Paroxysms. In the case of Major explosions is instead clearly enhanced from multiple signals stacking procedure (Fig 4.12). Each signal of our data-set, however, show an inflation phase which became evident (i.e. emerge from noise) at least 200-300 seconds before the explosive onset (Fig. 4.12b). Apart from the possible implications for Early-Warning systems design, this proves that tiltmeters are capable to investigate processes occurring in a previously almost undisclosed temporary window.
Following the common interpretation of these phenomena, involving the fast rise of a LP batch of magma inside the shallow conduit [68], we should conclude that we are now observing the final stage of this process. *Burton et al.* (2007) [11], "demonstrates", using spectroscopic measurements, that the slugs which are driving the ordinary explosive activity, form at depth of ∼3 km (below the summit). Accepting their conclusions, and according to *Kawaguchi and Nishimura* (2015) [52], who modeled the deformation associated to a gas-slug rising in the upper conduit of Stromboli using the slug-rise model from *James et al.* (2008) [48], the bottom of a gas slug ascends with a constant velocity U_s. This velocity depends on the conduit radius a and dimensionless Froude number F_r and can be espressed as:

$$U_s = F_r\sqrt{2ga}. \tag{4.1}$$

where g is acceleration due to gravity force. Froude number depends on the viscosity of melt (η) and the density of melt (ρ). Density of gas is assumed to be negligibly small compared to density of melt. Using reasonable parameter values (a=3 m,

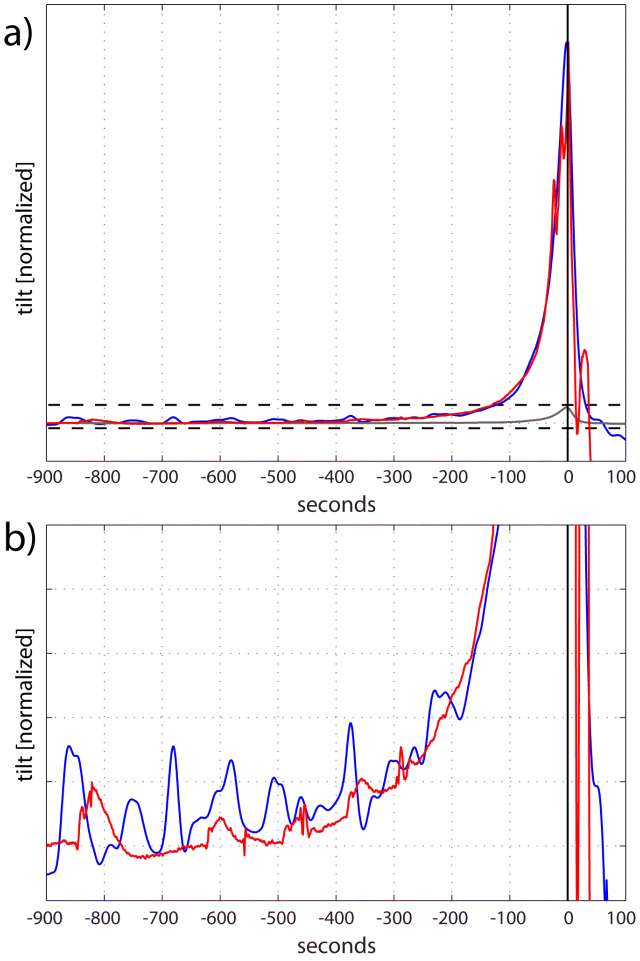

Figure 4.17: a) Comparison between normalized tilt signal of Mar. 5, 2007 paroxysm (red) and stacked trace of major events (blue) at OHO station. Gray line is the same as blue but scaled with respect to paroxysm. b) Same as in (a) but with expanded vertical scale to better show the initial phase of the tilt inflation. Traces are aligned using explosion onset.

$\eta = 10^3$ Pa, ρ=2600 kg/m^3) [52], a velocity of $\sim$ 2.5 m/s is obtained. A slug rising in the conduit, is supposed to only accelerate in the very last portion of the conduit [?], so this value can be considered as stationary to describe the deeper part of its rise. Considering the 500 seconds-long tilt inflation, a starting depth of about 1250 m below the crater terrace is found. While this value cannot be accepted as a prove of the starting point of the slug position, is rather considerable as the limit at which the effects of the slug-rise can be observed with our surface network configuration. By contrast, the results of *Kawaguchi and Nishimura* (2015) are indeed confuting this explanation. When the temporal changes of tilt associated to the gas slug ascent are considered, both for a flat or more realistic conical shape, the expected tilt shows in fact a deflation signal which is generated by a contraction source into the conduit. The pressure drop is due to the decreasing average density of the conduit caused from the expansion of the slug and the traction force on the conduit walls [52], [75]. To date, ground deformation recorded at Stromboli during major and paroxysmal events seems to be not explained by the common slug-rise model. However the

interaction dynamics between the gas, liquid and solid are complex and an accurate description of these dynamics will need to include also the effects of pressure changes related to the diffusive growth of gas bubbles [74], [75] on the LP magma batch while ascending into the shallow feeding system.

4.7 Conclusions

Major explosions and Paroxysms represent the most energetic explosive manifestation of Strombolian activity. When individually observed, explosive dynamics seem to show complexities and over-imposition of multiple events and phenomena, each one contributing to the characteristic geophysical signature of each event. The synergetic integration of different geophysical data-set allowed characterizing the event about timing [103], [87], explosive dynamics and, finally, to extract some inference on the shallow magmatic system and even the source process [84], [2]. The petrographical analysis of ejected magma revealed the substantial involvement of relatively less evolved (LP) magma [86], [9]. This gas-rich magma, never observed during ordinary activity [35], is claimed to act as a driving force in the generation of these violent phenomena [86]. Geochemical [11], [2] and petrographical evidences [68] place the source of violent Strombolian explosions to a deep (5-10 km) source, suddenly releasing a small batch of magma which quickly rise the magmatic system to the surface. Tilt data presented in this work, disclose new insights on this type of events evidencing how, major and paroxysmal event share the same inflation pattern. This geophysical evidence demonstrate a common dynamic process resulting in a common pattern of ground deformation, scalable in amplitude and compatible with pressure increase inside the shallow magmatic conduit prior to the climatic explosion. This pressure increase can be detected at least 500 seconds before the explosive onset. Apart from the obvious implications for Early-Warning systems, these evidences proves once more that tiltmeter are capable to successfully investigate processes occurring in a deeper portion of the magmatic system. Still far to be solved, the quest for a model capable to explain the source mechanism of this violent Strombolian activity, has now to take into account also the contribution of tilt data. To date in fact, it is still missing an exhaustive and comprehensive theory able to couple all the geophysical, geochemical and petrological evidences collected during the past tens years.

Major Explosions (2005 - 2015)

	date	time	tilt (μrad)	VLP (μm)	Vel (μm/s)
1	2005-08-05	11:08:45	0.577	12.42	238
2	2006-05-22	22:38:23	0.537	15.6	650
3	2006-06-16	13:42:02		19.11	94
4	2006-10-16	19:11:33	0.604	9.24	289
5	2006-12-15	12:29:29	0.684	8.87	371
6	2008-02-29	02:17:03	0.26	9.03	388
7	2008-09-07	07:49:09	0.432	7.67	123
8	2008-12-06	20:49:06	1.903	33.89	404
9	2008-12-17	13:39:04	0.568	14.15	153
10	2008-12-31	23:02:34		9.19	107
11	2009-05-03	14:58:00	0.536	7.41	308
12	2009-07-14	13:04:56	0.302	9.99	58
13	2009-11-08	12:29:45	0.631	24.82	232
14	2009-11-24	11:20:49	0.648	24.64	806
15	2010-01-04	19:12:25	0.309	6.14	220
16	2010-01-10	14:48:38	0.337	18.43	146
17	2010-03-12	07:57:58	0.311	20.2	230
18	2010-06-25	06:02:57	0.407	14.99	135
19	2010-06-30	16:34:54	2.055	30.45	896
20	2010-12-19	09:56:09	1.562	20.94	412
21	2011-03-04	12:25:26	0.566	12.59	93
22	2011-07-05	02:45:31	1.537	15.7	241
23	2011-07-10	15:21:02	1.402	17.85	150
24	2011-07-17	20:45:11	0.389	15.21	188
25	2011-08-05	07:15:00			112
26	2011-08-15	19:33:43	0.295		19
27	2011-09-05	03:52:23	0.953	7.52	225
28	2012-03-06	06:43:45	1.469	22.98	255
29	2013-12-04	23:48:37	0.995	22.53	55
30	2013-12-14	17:07:23	0.391	9.64	152
31	2014-01-04	23:05:39	1.431	23.95	43
32	2014-10-18	17:30:28	0.572	18.39	150
33	2015-07-16	01:03:35	0.43		

Table 4.1: List of Major events recorded between Aug. 2005 and Dec. 2015. Seismic displacement in VLP band, seismic peak velocity and tilt amplitudes are reported. Tilt amplitude is calculated at OHO station. Seismic amplitude at STR station. In the last column sorce vent, as determined from thermal imagery and infrasound array location, is reported. Empty fields indicate missing data for instrumental malfunctioning.

Chapter 5

Effusive activity

5.1 Effusive activity at Stromboli volcano

Although Stromboli volcano is world-wide known for its persistent, mild Strombolian explosive activity, from time to time, its typical Strombolian behavior is interrupted by phases dominated by effusive activity, here referred as *effusive crises*, and minor effusive events called *overflows*. Effusive crises occur every 5-15 years [6] while there is no clear statistic for overflows. Since the formation of the horse-shoe-shaped *Sciara del Fuoco* depression, all the effusive activity has been confined on this flank of the volcanic edifice. Between 1888 and 1986, 26 episodes of major lava flow are reported in literature [6]. During the last 30 years four effusive eruptions occurred on Stromboli volcano in 1985, 2002-2003, 2007, and 2014. Three of those (2002-2003, 2007, and 2014) were recorded by the LGS geophysical network (Fig. 5.1).

While the historical record about major effusive events is reasonably complete,

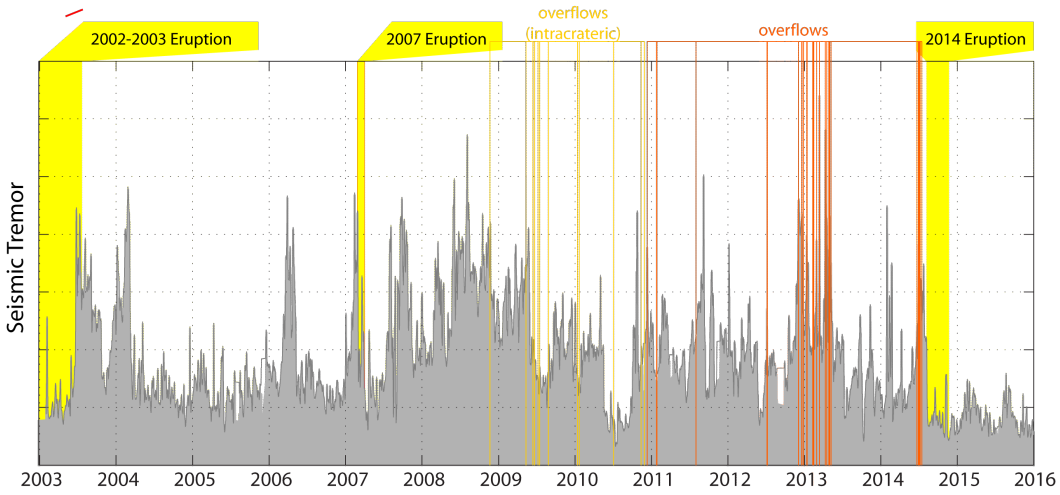

Figure 5.1: Effusive crises (yellow patches) and overflows (orange lines) occurred between 2003 and 2015. Intracrateric overflows dates (light orange) are from *Calvari et. al* (2014) [13]. Gray background represents the seismic tremor level.

due to its relevant impact, long duration (90 days in average [6]) and significant volumes of emitted magma, overflows are almost neglected probably because of the short duration (often only a few hours) and the little amount of magma involved. Moreover overflows are often confined into the crater terrace as intracrateric events. In historical records there are few clear examples of small effusive events and a number of not-well-constrained episodes which are supposed to belong to this class of phenomena [6]. In recent times, between 1990 and 2003, only five overflows are documented [13]. By contrast, in the last decade, at least 41 minor effusive events have been reported. After the complete lack of minor effusive episodes during the 2003 - 2007 inter-eruptive period [13], a much larger number of events is instead reported since November 2008 (Fig. 5.1). A first period (2008-2010) was characterized by intracrateric overflow activity, with several episodes, at least 8 according to *Calvari et al.* (2014). Successively, between Dec. 2010 and Jul. 2012, six scattered events were recorded. Later a period of dense overflow activity was recorded between December 2012 and May 2013. In this period in fact, 19 events were recorded. Finally a second cluster of events, in June-July 2014, shortly preceded the 2014 major effusive crisis

[111].

5.1.1 Observational differences between effusive crises and overflows

Major lava flows and minor overflows, sharing the same effusive nature, differ by distinctive characteristics. Major effusive crises are characterized by conspicuous volumes of emitted magma (10^6 - 10^7 m^3 [31]), resulting in the emplacement of branched lava flows on the *Sciara del Fuoco* and constructing lava deltas causing relevant changes in the topology of the shoreline. By contrast, magma emitted during overflows, even when enplaced on the *Sciara del Fuoco* slope, rarely reaches the sea. Duration of phenomena spans from months (90 days in average according to *Barberi et al.*, 1993) to hours for the short-lasting overflows. Finally, a last difference consists in the source vent position. Large lava flows mainly originate from newly opened vents outside the crater rim or from fissures cutting the crater terrace. On the other hand, during overflows, magma exit from the already active explosive vents, mainly remaining confined in the summital part of the volcano.
Based on the historical documentation, major effusive events, with primary magma output from the crater rim are also reported as well as sea level vent opening [6]. However, at least in the last decades, major effusive events were always associated to the opening of a new vent on the *Sciara del Fuoco* slope, at a lower elevation with respect to the explosive vents. Our 13-years-long data-set (Fig. 5.1) only contains this type of effusive events.

5.2 Lava Flows

In this section the three effusive crises recorded since the installation of LGS network will be introduced. The conspicuous geophysical data-set relative to these eruptions has been already analyzed and published in several works [95, 93, 60, 91, 111]. In the following paragraphs, after a short description of the eruptions, the last interpretative model, proposed by *Ripepe et al.* (2015) [91], and based on an integrated geophysical approach will be introduced and implications will be briefly discussed.

5.2.1 Chronology of the 2002-2003, 2007 and 2014 effusive crises

Since the initial deployment of the LGS integrated geophysical network, three major eruptive crises have occurred at Stromboli volcano. These long lasting lava flows have in common the opening of new effusive vents on the *Sciara del Fuoco* slope, at lower elevation with respect to the crater terrace and the emission of large volumes of magma. Single Paroxysms occurred During two over three effusive phases (2002-2003 and 2007). Here a brief chronological description of these three eruptions is draft. More detailed analysis have been diffusely reported in literature in the past years.

The 2002-2003 eruptive crisis After several months of high intensity activity, on December 28, 2002, an eruptive vent opened on the NE flank of the *Sciara del Fuoco* slope, at 600 m a.s.l. elevation [85]. The emplacement of multiple branched

lava flow on the slope triggered gravitational instability processes with the partial collapse interesting also the rim of the summit crater terrace. About $10\times10^6 m^3$ of infilling deposit were involved [109]. The failure affected also the submerged portion of the *Sciara del Fuoco* producing a Tsunami wave. Several vents, opened at different elevations, were involved in the emission of the lava flow during the first days of the eruption [106]. After a paroxysmal explosion on April 5, 2003, the lava flow finally ceased between July 21 and July 22, 2003. A progressive declining of lava flow emission rate was concomitant with the restart of the normal explosive Strombolian activity [98].

The 2007 eruptive crisis The effusive crisis of 2007 started on February 27, after 13 days of anomalous high intensity explosive activity [93]. The effusive phase started with a very fast-moving lava flow from a fracture opened at the base of the NE vent [93], that rapidly reached the sea. The effusion was preceded by a relevant deformation of the upper part of the *Sciara del Fuoco* [17] resulting in an increase of number of landslide events per hour [60]. After few hours, a second effusive vent opened at an elevation of 400 m a.s.l., on the *Sciara del Fuoco*, accompanied by intense flank deformation [17] and landlide activity [93]. This vent remained stable during the whole effusive period emitting about 9.5 Mm^3 [14]. A few days after magma effusion started, a progressive, partial collapse of crater terrace was observed [87, 64], following the drainage of shallow magmatic system [60, 91].
On March 15, 2007, a paroxysmal explosion was registered (see previous chapter) causing a dramatic change in the crater terrace topology by removing the previously collapsed material [87]. Effusive activity finally stopped on April 2 [14], after 35 days. During the effusive crisis the explosive activity at the surface ceased completely, only recovering few months after the end of the eruption.

The 2014 effusive crisis The onset of effusive phase was marked by the opening of a lateral effusive vent, on August 7, 2014 at 05:00 GMT. The vent opened along the *Sciara del Fuoco*, on its NE side, at an elevation of about 650 m a.s.l. [111] (Fig. 5.2). The main lava flow was preceded by a complex phase, started about 15 hours before with the partial collapse of the external rim of the NE crater. This collapse, registered as a large rockfall from seismic stations, also triggered a small lava flow on August 6th.[111, 26]. This effusive eruption occurred at the end of a two-months-long period of progressively increasing Strombolian activity [111]. During this period several overflow episodes (June-July 2014) also occurred. These conditions suggest a trend of magma level rise inside the upper conduits, which eventually triggered the main effusive crisis. Differently from what experienced during the 2002-2003 and 2007 eruptions, no paroxysmal explosive events occurred at this time. The effusive phase lasted 107 days, producing a total erupted volume of $\sim5.5\times10^6 m^3$, as derived from MODIS observation provided from MIROVA.

5.2.2 Geophysical Characterization of Lava flows

Despite the differences between the chronological development of the three eruptions, some similarities can be found, amongst the peculiarities of each crisis.

Figure 5.2: Picture of the 2014 eruptive vent. Picture is taken from the shelter sited at Q.850, on the eastern rim of the *Sciara del Fuoco*, on Aug. 25, 2014. At that time the lava flow was still alimented at a rate of 1-2 m^3/s. The partially collapsed NE crater is visible in the upper left corner of the image. The effusive vent is about 2-4 meter wide.

- *Vent opening* All the effusive crises started with the opening of one (or more) new vent on the *Sciara del Fuoco* slope.
- *Vent position*The vent opening occurred on the NE side of the *Sciara del Fuoco*, and was associated processes of gravitational instability of the volcanic flank, resulting in rockfalls and landslides along the slope.
- *Precursory phase* The effusive phase apparently followed a period of increased Strombolian explosive activity and intense degassing.
- *Ceasing of Explosive Activity* During the effusive phases no explosive activity from summit craters was observed. After the end of the lava flow the explosive activity was gradually recovered.

These common features are also associated to consistent geophysical observations which allow to describe and characterize this common pattern under a geophysical point of view. The increase of the ordinary explosive activity before the onset of the effusive phases, is clearly observed by the geophysical integrated network as an increase of the monitored parameters such as: seismic tremor, VLP rate, pressure and number of infrasonic transients and thermal activity. In figure 5.3, this general increasing trend of the geophysical parameters for the 2014 eruption is shown as an example. The trend, that reflects an increase of the explosive activity, is consistent with the gradual rise of the magma level inside the upper conduits. This upward movement is associated with an increase of degassing activity, thus suggesting a gentle increase of deep magma input rate. In this scenario, the occurrence of overflows (which was not observed unless in 2014 eruption), indicates that magma column reached the crater terrace elevation and stationed at this level, overcoming this limit from time to time.
The opening of a new vent on the *Sciara del Fuoco* slope was always associated to rockfalls and crater rim failures on the NE side of the crater terrace. In 2007, an

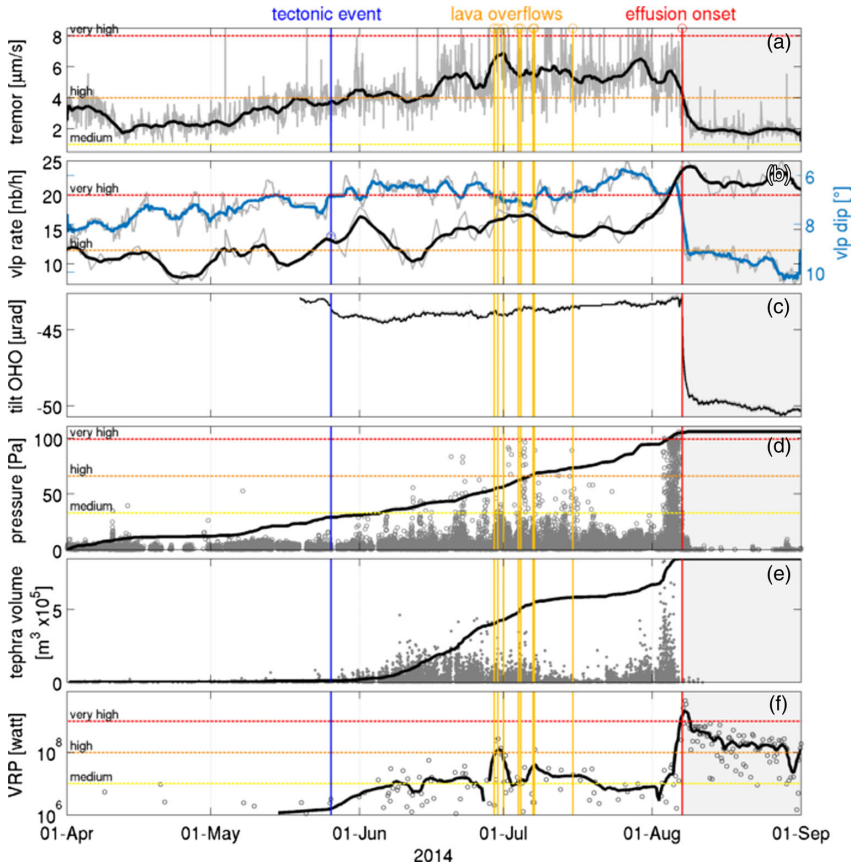

Figure 5.3: Evolution of geophysical parameters between April and September 2014. Effusive event is marked by vertical line as well as the overflows occurred on June-July 2014. A general increase of monitored parameters, preceding the effusive onset on Aug. 7, is recorded by seismic tremor amplitude (a), VLP rate (i.e. number of VLP signals per hour, b), ground deformation from tilt (c), infrasonic pressure associated to explosive and degassing transients (d) and thermal activity, expressed as tephra volume derived from ground-based thermal analysis (e) and thermal radiative power from MODIS data (f). This trend, starting a couple of months before the effusive crisis, increased dramatically in the last week. Figure is from Valade et al. 2016, [111]

increase of the number of landslide events per hour (Fig. 5.4c), was interpreted as the evidence of those instability conditions [60]. Concurrently *Casagli et al.* (2009) measured intense and localized deformation on the *Sciara del Fuoco* using ground-based SAR interferometry tecnique [17]. During the vent opening phase, the seismic tremor amplitude registered a peak. In contrast with the typical behavior of Stromboli, where seismic tremor and infrasound amplitudes commonly modulate together, this peak is not associated to infrasonic activity [93, 111]. This is interpreted as the result of magma migration along the new fractures towards the opening vent, and is consistent with the deflation recorded by the clinometric network [60, 111].

The explosive and puffing activity, which were very high in the last hours pre-

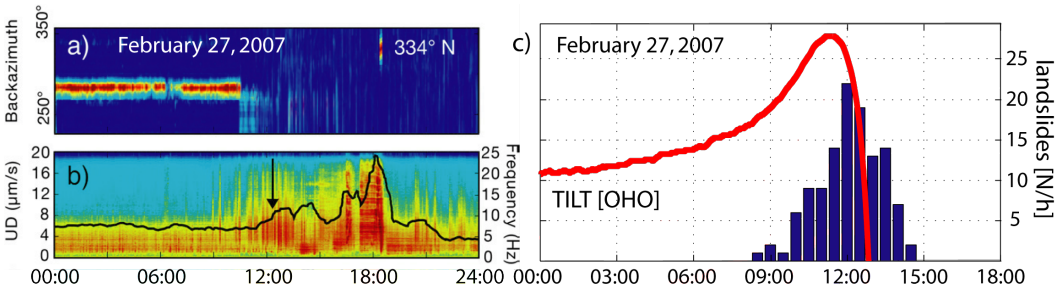

Figure 5.4: Decoupling of infrasonic degassing activity (a) and seismic tremor (b) at the onset phase of the 2007 effusive eruption at Stromboli, From: Ripepe et al. 2009 [93], modified. c) Correlation between ground inflation and number of landslide events per hour, From Marchetti et al. 2009 [60], modified.

ceding the 2002-2003, 2007 and 2014 eruptive onsets, stopped completely when the effusive phase started [93, 111]. This phenomenon is particularly evident from infrasound records (Fig. 5.4a and Fig. 5.3d) and thermal imagery. Also seismic traces show the absence of explosion-quake signals. This evidence is consistent with the sudden magma drainage from upper crater towards the newly opened, and lower, effusive vent. Despite the complete lack of visible explosive activity, VLP events persisted, almost unaffected in waveform and amplitude, but registering a sudden deepening of the source position. This is revealed by signal polarization change (Fig. 5.3b) [91, 111]. Consistently with the out-pouring lava flow, ground deformations recorded a large deflation signal, compatible with the drainage of the shallow magmatic system acted by the ongoing lava flow (Fig. 5.3c). Tilt signal showed a very rapid deflation during the first hours of the effusion and a significantly less intense deflation trend in the following days [4, 60, 111]. Finally thermal radiative power, detected from satellite-based MODIS sensors, allows to track and estimate the volume of emitted magma over time. Obtained data-set indicates that, after a first peak value (> 20 m^3/s), magma effusion rate gradually decreases with exponential decay over a few days/weeks, finally reaching a stable value of 0.2 - 0.4 m^3/s, comparable with the values recorded during the most typical Strombolian activity (0.1 - 0.5 m^3/s) [3, 46, 98, 11].

These geophysical observations have been consistently recorded during all the three most recent effusive crises. Hence, at least according to our limited data-set, should be considered as properly representative of the major lava flow episodes of Stromboli volcano. When integrated together, depict an image rather complete that led

Ripepe et al. (2015) to formulate a new model which proved to be consistently able to include all the reported geophysical observations [91].

5.2.3 Gravity-driven magma discharge model: formulation and implications

The magma emitted during lava flow activity is a crystal-rich (HP) magma, identical to that commonly sustaining normal Strombolian activity [8]. The large volume of magma emitted during these long lasting effusive phases (in the order of 10×10^6 m^3), requires to imagine that this already degassed magma, also emitted during the regular Strombolian activity, has to be stored somewhere in the upper portion of the magmatic feeding system. The sudden arrival of LP magma from the deeper part of the magmatic system trigger pressurize the upper system and trigger the lava effusion. Once the deep input is accommodated into the shallow feeding system the effusive activity stops. This interpretation, although rather straightforward is not fully consistent with the geophysical observations. Recently *Ripepe et al.* (2015) [91], proposed an alternative model to explain the lava flows episodes occurred on Stromboli in the last decades. The model was developed mainly on the base of the 2007 eruption data and then successfully applied also to the 2014 eruption by *Valade et al.* (2016) [111]. The author contributed in both the published paper, mainly about ground deformation data processing and modeling. In the following paragraph the model is introduced, the complete description is published as:
Ripepe M., Delle Donne D., Genco R., Maggio G., Pistolesi M., Marchetti E., Lacanna G., Ulivieri G., and Poggi P., 2015, Volcano seismicity and ground deformation unveil the gravity-driven magma discharge dynamics of a volcanic eruption. Nature Communications, 6:6998. [91].

5.2.3.1 The Gravity-Driven model

Differently from the most common interpretation, where lava effusion represents the result of a deep magma input, *Ripepe et al.* proposed to model the eruption as a gravity-driven drainage of magma stored in the volcanic edifice with only a minor contribution of magma supplied at a steady rate from a deep reservoir [91]. The shallow feeding system of Stromboli volcano can be represented as a shallow cylindrical plumbing system just below the crater terrace recalling its shape: a 300m long and 140m wide ellipse. Hence the reservoir drainage can be modeled as the discharge of the portion vertically extending between the crater terrace and the new effusive vent (Fig. 5.5). The velocity of magma flow from the output vent u, can be modeled as a Poiseuille flow, which is:

$$u(t) = \frac{a^2}{4\eta L}\Delta P(t), \tag{5.1}$$

where a is the effusive vent radius, η is the magma viscosity, L is the dyke length and ΔP_h is the differential pressure between the magma-static pressure at the vent elevation (P_h) and the atmospheric pressure at the vent (P_{atm}). Magma-static pressure can be expressed as $P_h(t) = \rho g h(t)(1-\Phi)$, where ρ and Φ are the DRE magma density and vesicularity, respectively, and h is the magma height with respect to the

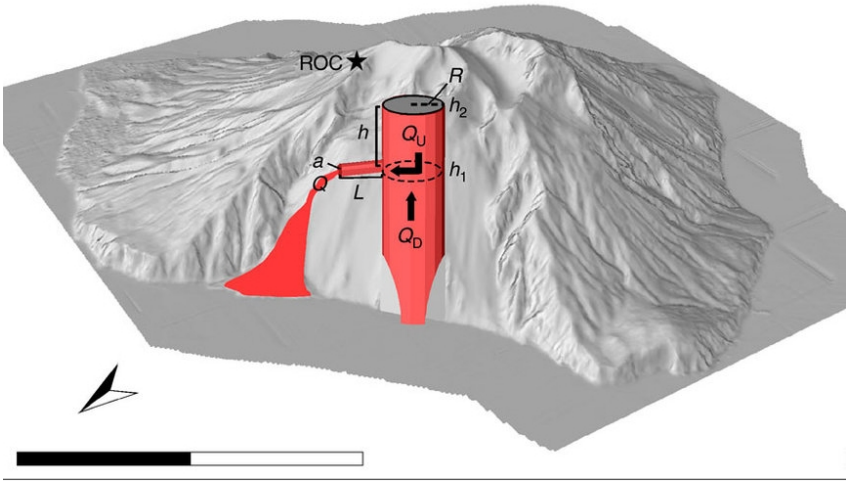

Figure 5.5: Shaded relief 3D model of Stromboli volcano as seen from the North, with a sketch of the shallow reservoir model. Scale bar, is 2 km long. Letters refers to parameter as explained in text (From Ripepe et al. 2015 [91], modified).

vent elevation. According to these equation, the effusion rate $Q_E$from the vent can be expressed by the formula:

$$Q_E(t) = \pi a^2 u(t) = (1-\Phi)\frac{\pi a^4}{8\eta L}\rho g h(t), \tag{5.2}$$

As lava drains from the effusive vent, the level of magma inside the upper reservoir h will decrease to the minimum represented by the vent elevation. This discharge can be buffered by the eventual input rate Q_D from the deeper feeding system Q_D, such as the total effusive rate Q_T is expressed as $Q_T = Q_E + Q_D$. Gravity-driven magma discharge dynamics explain the initially high discharge rates observed during eruptive crises and the rapid decay. A longer duration of the effusive phase can be easily obtained with a deep input $Q_D > 0$. By fitting the effusion rate curve obtained from satellite based thermal imagery is also possible to calculate the expected ground deformation using the computed magma level $h(t)$ change. Assuming a simple cylindrically-shaped source [10], tilt can be calculated as:

$$\tau(t) = G\frac{R^2}{\mu}\Delta P(t) \tag{5.3}$$

where μ is the rigidity, R is the radius of reservoir, and G is:

$$G = \frac{x}{2(h_2-h_1}\left[\left(\frac{3h_2^2}{r_2^5}-\frac{2\nu}{3r_2^3}\right)(h_2-h_1)+\left(\frac{h_2}{r_2^3}-\frac{h_1}{r_1^3}\right)-(2\nu-1)\left(\frac{1}{r_2(r_2+h_2)}-\frac{1}{r_1(r_1+h_1)}\right)\right] \tag{5.4}$$

with $r_i = \sqrt{x^2+h_i^2}$, x is the distance from the axis of the cylindrical conduit, ν is the Poisson's ratio, h_2 is the level of magma and h_1 the elevation of the vent [75]. Using these equations, the magma discharge rate can be related with the contraction of the volcano edifice recorded by ground tilt (Fig. 5.6). The model provides, under simple assumptions, a straightforward and efficient way to compare and correlate

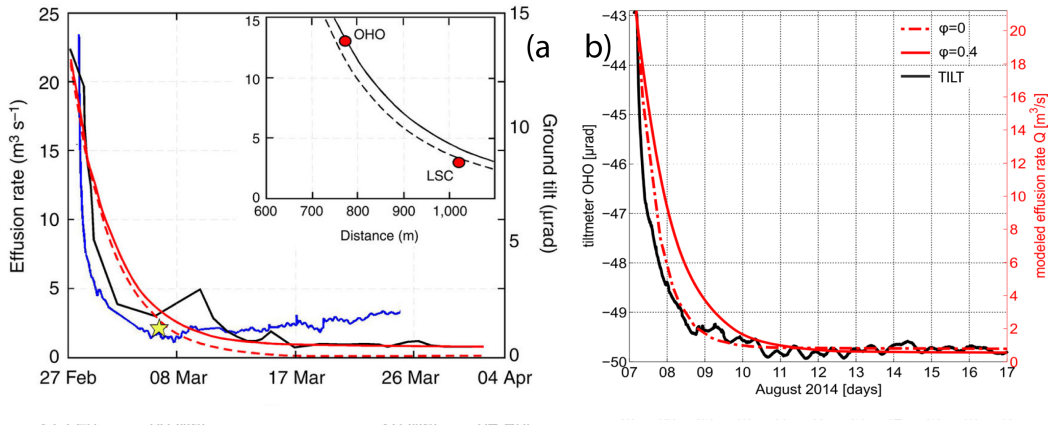

Figure 5.6: (a) Comparison between magma effusion rate (black), modeled effusion rate (red) and ground tilt (blue) for the 2007 eruption. Continuous and dashed red lined are calculated with vesicularity =0 or =0.4, respectively. In the inset fitting between observed tilt amplitudes at OHO and LSC stations and modeled is reported. (From: Ripepe et al. 2015, modified [91]). (b) Comparison of ground tilt (black) and modeled effusive rate (red) with veicularity = 0 (dashed) and =0.4 (continuous), for the 2014 eruption (From: Valade et al. 2016, modified [111]).

effusion rate, ground deformations and other geophysical parameters such as the VLP source position with the process of drainage of the shallow magmatic system. The perfect fitting between observations and model prediction allows to retrieve quantitative information on effusive rate and pressure drop caused by magma level decrease inside the upper conduits starting from reliable ground deformation data.

5.2.3.2 Application to the 2014 effusive eruption

The Gravity-driven model proposed by *Ripepe et al.* (2015) was also used by *Valade et al.* (2016) [111] to interpret and model the geophysical data-set of the effusive phase of the 2014 eruption. In figure 5.6b, the fit between modeled effusion rate and ground tilt is shown. Also in this case the model provided good fitting between predicted and estimated effusive rate. To explain the 107 days long eruption, a deep input, varying over time from an initial value to 0.8 to a final value of 0.3 m^3/s was also considered. The at least two-months-long increase of activity preceding the onset of the effusive phase is consistent with a gradual increase of the deep input rate. The increment, also responsible for the repeated overflow activity on June-July 2014, finally triggered the opening of the main effusive vent and the following shallow system drainage. Apparently the deep input gradually decreased after the onset of the eruption eventually recovering the steady 0.3 m^3/s rate.

5.2.3.3 model implications

The magma drainage model by gravity load appears to dominate the effusive dynamics and changes our perspective from deep to shallow magma dynamics as the controlling factor for effusive eruptions [91]. Apart for Stromboli case, the model was also succesfully applied to Kilauea volcano [80], Nyamulagira volcano [24] and

Bardarbunga volcano [25, ?]. Although the model cannot certain be applied to every case, still provide a powerful instrument for investigating several effusive scenarios, with particular emphasis on Stromboli lava flows. Based on our data-set, in fact, the opening of a lower effusive vent on the *Sciara del Fuoco* has been stated as the most typical scenario for major effusive crises at Stromboli. Despite the fact that model uses a deep input to guarantee the long-lasting effusive activity, it is worth noting that the deep input rate was quite small when compared with the peak value of the recorded effusion rates and, in any case, in the same order of magnitude of that observed during typical Strombolian explosive activity (0.3 m^3/s [3]). Moreover, the maximum modeled values (0.85 m^3/s [91]) are consistent with the increased activity preceding the effusive onset and lower of those sometimes observed during minor overflows. This suggests that the input from deep, which perhaps may act as a trigger for the opening of the lateral effusive vent, is not directly responsible for the effusive activity. In fact, over the last 12 years (2003-2015), several phases of high Strombolian activity not followed by major effusive crises have been recorded.

5.3 Overflows

A full list of the overflow events recorded between December 2010 and July 2014 is presented in table 5.3. The events occurred before December 2010, marked in figure 5.1 with light-orange-colored lines, are not discussed and analyzed in this work. Due to the intra-crateric nature of those, in fact, was not possible to clearly observe those events with the LGS Integrated Network thermal cameras of ROC station. 5.1). According to *Calvari et al.*, 2014 [13], the intra-crateric overflows of 2008-2010 were mainly related to the activity of the Central (CE) crater, with a couple of episodes from North-East (NE) crater and South-West (SW) area. During the analyzed period (Dec. 2010 - 2016) 35 overflows have occurred. This number refers to events clearly distinct, while the eventual phases of reprise of an already ongoing overflow are not counted. This approach has some limitations. As an example, the first event in table 5.3 (Dec. 11, 2010 to Dec. 14, 2010), is considered as a single event, while is probably composed by different distinct episodes. In this period, the very harsh meteo conditions prevented from a clear overview of the phenomena. However, based on the available data-set, the 2011 - 2015 period was characterized by a relative stability of the overflow source position. Two distinct phases can be distinguished. In 2011 - 2012 period, the main vent producing overflows was the newly built hornitos-like cone situated in the SW area of the crater terrace. This hornito (SWh) was formed by continuous growth of a vent opened on the internal side of the crater terrace rim. Since December 2012 the overflows events "moved" to NE side of the crater area becoming a prerogative of NE vents.

5.3.1 Overflow events overview

A list of 35 overflows is reported in table 5.3. In the following paragraphs, the overflow events will be distinguished in three main groups based on simple temporal and positional criteria. A first phase, relative to the activity of the SW crater hornito has been distinguished as temporally and locally limited to the effusive activity of this vent between December 2010 and December 2012. A second phase,

Overflows (Dec. 2010 – Jul. 2014)

	start time		end time		duration	vent	tilt [urad]
1	2010-12-11	12:00:00	2010-12-14	12:00:00	3 d	SW	
2	2011-01-25	08:30:00	2011-01-25	09:30:00	1 h	SW	
3	2011-01-26	20:30:00	2011-01-26	22:00:00	30 m	SW	-0.092
4	2011-08-01	20:00:00	2011-08-02	02:00:00	6 h	NE (base)	
5	2012-07-05	20:30:00	2012-07-05	23:45:00	3 h 15 m	SW	-0.018
6	2012-07-07	23:25:00	2012-07-08	00:45:00	1 h 20 m	SW	-0.059
7	2012-12-03	09:00:00	2012-12-03	15:00:00	6 h	SW	
8	2012-12-18	13:00:00	2012-12-18	17:45:00	4 h 45 m	NE	-0.104
9	2012-12-20	07:00:00	2012-12-20	15:00:00	8 h	NE	
10	2012-12-26	17:45:00	2012-12-26	21:00:00	3 h 15 m	NE	
11	2013-01-11	17:00:00	2013-01-11	21:00:00	4 h	NE	
12	2013-01-12	10:15:00	2013-01-12	15:00:00	4 h 45 m	NE	-0.165
13	2013-01-13	21:00:00	2013-01-14	20:00:00	23 h	NE	
14	2013-02-09	12:55:00	2013-02-09	13:10:00	15 m		
15	2013-02-10	13:20:00	2013-02-10	17:00:00	3 h 40 m	NE (base)	
16	2013-02-11	06:00:00	2013-02-11	06:30:00	30 m	NE (base)	
17	2013-02-11	13:20:00	2013-02-12	04:00:00	19 h 40 m	NE	
18	2013-02-14	11:05:00	2013-02-14	12:15:00	1 h 10 m	NE	
19	2013-02-27	14:00:00	2013-02-27	18:00:00	4 h	NE	-0.035
20	2013-03-13	09:00:00	2013-03-13	17:00:00	8 h	NE	
21	2013-04-10	13:30:00	2013-04-10	18:00:00	4 h 30 m	NE	
22	2013-04-17	14:30:00	2013-04-17	20:30:00	6 h	NE	-0.236
23	2013-04-26	23:00:00	2013-04-27	07:00:00	8 h	NE	
24	2013-04-29	09:40:00	2013-04-29	12:30:00	2h 50 m	NE	
25	2013-05-01	14:50:00	2013-05-01	19:50:00	5 h	NE	
26	2013-05-07	20:30:00	2013-05-07	22:30:00	2 h	NE	-0.068
27	2014-06-22	03:00:00	2014-06-22	15:00:00	12 h	NE	
28	2014-06-29	02:00:00	2014-06-29	11:30:00	8 h 30 m	NE	
29	2014-06-29	19:00:00	2014-06-30	13:00:00	15 h	NE	-0.075
30	2014-06-30	23:00:00	2014-07-01	03:00:00	4 h	NE	
31	2014-07-04	02:00:00	2014-07-04	04:00:00	2 h	NE	-0.078
32	2014-07-04	14:00:00	2014-07-04	16:00:00	2 h	NE	-0.109
33	2014-07-07	03:30:00	2014-07-07	07:30:00	4 h	NE	-0.199
34	2014-07-07	09:00:00	2014-07-07	12:00:00	3 h	NE	-0.086
35	2014-07-15	10:00:00	2014-07-15	12:00:00	2 h	NE	

Table 5.1: List of overflow events recorded between December 11, 2010 and July 15, 2014. Onset date and time, end date and time, duration, effusive vent and associated tilt are reported. Empty fields indicate missing information.

from December 2012 to May 2013, was instead characterized by the effusive activity of the NE crater, mainly on the external side of the *Sciara fel Fuoco*. Finally a last temporally well constrained cluster of effusive events, still from the NE area of the crater terrace, is recorded in June-July 2014. This group of events is considered as separated because these overflows are shortly preceding the the major effusive crisis started on August 2014, and occurred when geophysical parameters already indicate a trend of general increase of explosive activity which finally culminated with the effusive eruption.

5.3.1.1 2010 - 2012: the SW hornito phase

Between September 2010 and November 2011, a new prominent cone was built by repeated explosive and spattering activity on the SW area of the crater terrace. This hornito-looking structure evolved over time starting from a small fracture opened on the internal side of the external rim of the crater terrace at some point between September and October 2010. Since November 2011 this cone dominated the crater terrace morphology for a long time, finally being carved and partly destroyed in 2013 - 2014, after the end of its activity. The activity of this cone was characterized by long-lasting gas dominated emissions, alternating phases of intense degassing accompanied by continuous spattering and short-lived overflows. Because of its marginal position, and its elevation above the external crater rim, the most of effused magma was enplaced on the *Sciara del Fuoco slope*, on the NW side.

The events recorded in this period are characterized by short-lived magma overflows from the vent sitting on top of the small cone with intense spattering and degassing activity.

During this period, a single event separates from the group; a lonely overflow which was not generated by the SW crater but instead from NE area. This event, recorded in Aug. 1-2, 2011, was characterized by the sustained emission of magma from the NE crater rim. The evidence on the ROC thermal camera records (Fig. 5.8) of a relatively hot gas cloud rising from the lower margin of the camera field of view, seems to suggest that magma was perhaps also emitted from a fracture at the base of NE crater, spreading on the underlying *pianoro*. No other visible evidences of this have however been reported.

Apart from the December 2010 activity, the rest of the events lasted from 30 m to 6 hours (Tab. 5.3). A few more, shorter episodes of spattering from SW hornito were recorded in this period. Several of those were associated to small lava effusions which remained confined to the internal part of the crater terrace (as for example on Sep. 6-7 2011; Aug. 20-26, 2011; Aug. 6, 2012 etc.) other references are in *Calvari et al. 2014* [13].

5.3.1.2 2012 - 2013: the NE phase

Since December 18, 2012 the effusive activity shifted to the NE crater, abandoning completely the SW hornito. This second period of minor effusive activity consists on a dense cluster of 18 events, occurred during the 6 months-long window between December 18, 2012 and May 7, 2013 (Tab. 5.3). All the events were generated from the NE crater rim and were emplaced on the uppermost portion of the *Sciara del Fuoco*. For a couple of events, on Feb 10 and 11, 2013, the effusion also occurred

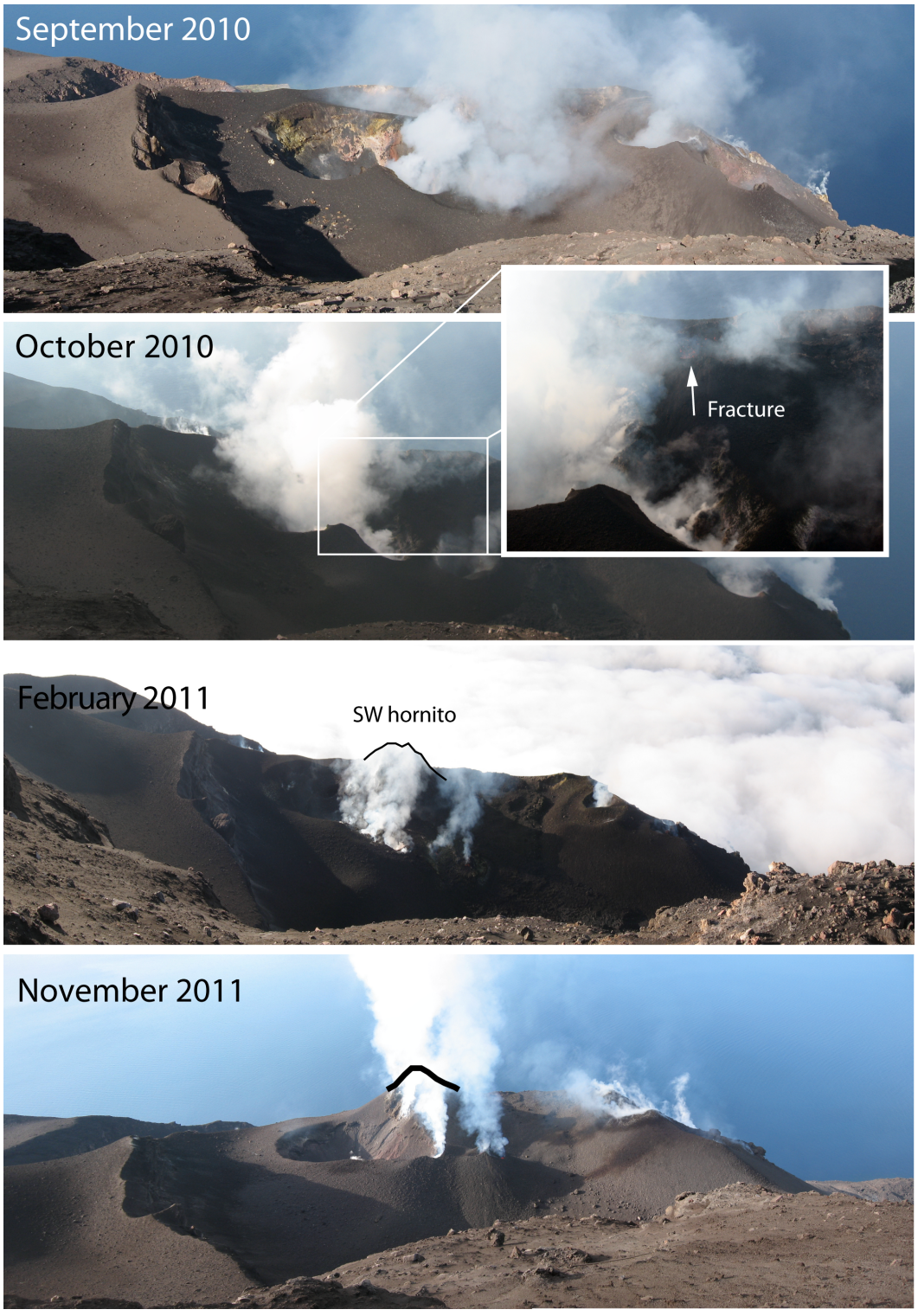

Figure 5.7: Series of pictures of the crater terrace area between September 2010 and November 2011 showing the birth and growth of the SW hornito-looking cone. Pictures are taken from *Pizzo sopra la Fossa* top area, from different point of view. The inset in (b) highlight the position of the crack later forming the structure.

Figure 5.8: Frame-shots from ROC thermal camera showing the evelution of overflow from NE crater rim. The black areas inclosed inside the white magma-covered area are due to sensor saturation, thus representing the hottest part of lava flow. A plume rising from right to left from the base of NE crater is visible on the first frame of the second row.

from the base of NE crater. The events were associated to intense degassing and spattering and have durations spanning from 15 minutes to 8 hours. In some cases a reprise of an ongoing event was observed but mainly these events were characterized by a single pulse of magma effusion.

5.3.1.3 2014: the pre-effusive NE phase

After about one year since the last overflow, nine short-lived overflow episodes were recorded between June 22, 2014 and July 7, 2014 (Tab. 5.3) [111]. All the events, occurred from NE vent, were accompanied by intense spattering activity from the overflowing vent. The first three events (Jun. 22 and Jun 29(2), 2014) show relatively longer durations (12, 8h30m, and 15h, respectively), while the rest of the episodes are shorter (less than 4 hours). At the time of this activity, the crater terrace was configured as shown in figure 5.9, with the easternmost vent practically open on the *Pianoro* side and the other NE vent (NE1 in 5.9) almost sited on the external rim of crater terrace. All the events occurred from NE1 vent and the resulting lava flows extended for several tens of meters on the *Sciara del Fuoco*. These events occurred in a short period of time (about 1 month) and with very similar development.

5.3.2 Geophysical characterization of overflows episodes

Seismic tremor, infrasonic activity, thermal images, and ground deformations recorded during the phases of overflow activity have been analyzed. The analysis of the geophysical data-set associated to overflow activity has been separately performed for the three distinct periods. However, independently from the active vent and the period, all the monitored parameters recorded a very similar pattern, thus suggesting a common dynamic for all the overflow events. The results of the elaborations are here presented together.

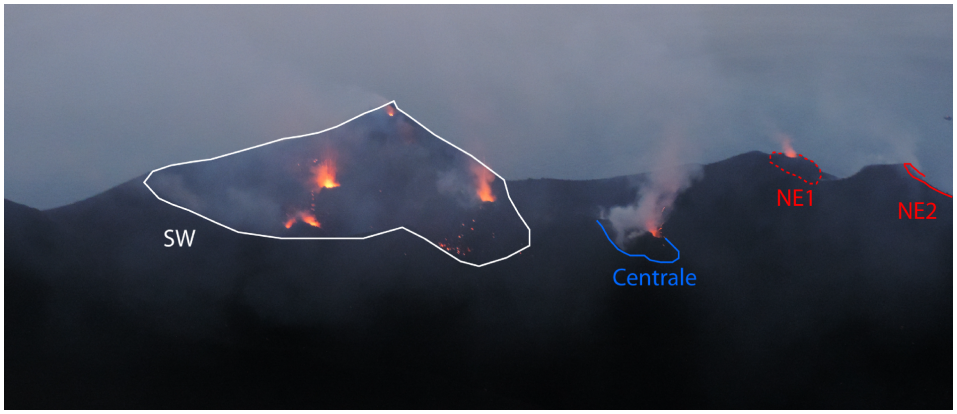

Figure 5.9: Configuration of the crater terrace are in June 2014. The SW (white), Central (blue), and NE (red) crater areas are delimited. The single vents can be distinguished because of the red glowing. The uppermost vent on the SW side is the 2012 hornito. Note how the NE2 vent is partially open on the outside of the crater terrace.

5.3.2.1 Seismic Analysis

Seismic data analysis reveals that overflow events were always accompanied by a rapid and dramatic increase of seismic tremor. The seismic tremor amplitude, abruptly increases to *high* (4×10^{-6} to $8 \times 10^{-6} m/s$) or *very-high* ($> 8 \times 10^{-6} m/s$) values, and maintains this level until the end of effusive activity. In figure 5.10, a sudden increase of tremor level, marked by the widening of the noise level in the seismic raw trace is recorded at 19:45 GMT on Jul. 5, 2012. This increment lasts until 23:59 GMT with a gradual decrease starting at 21:00 GMT. It is worth noting that this phase is preceded by a relatively smaller increase between 15:45 and 18:30 GMT, on the same day. This last phase, reaching *high* values was not accompanied by effusive activity. A second increase is recorded on Jul. 7, 2012 at 23:00 GMT. Also in this case the increment is quite rapid (less than 5 minutes! to reach the maximum amplitude) but the event has a shorter duration ($<$ 2 hours). As evidenced from the presence of transients associated to the regular explosive activity, these phases were not preceded or followed by relevant changes in the Strombolian activity (Fig. 5.10). The seismic chronology of this couple of events has been reported as an example. All the others events shows very similar seismic patterns indicating a strong increase of seismic activity during the effusive phases.
The spectral analysis of seismic traces during the overflow phases does not reveal any significant change in the spectral content with respect to typical spectrograms of seismic tremor recorded at Stromboli (Fig. 5.11). In contrast with what observed during the opening of the effusive vent on Feb. 2007 (Fig. 5.4), in this case seismic evidences of magma migration are detected during overflow events.

5.3.2.2 Infrasonic activity

Infrasonic activity analysis was performed using the data provided by EAR infrasound array. The analysis reveals that all the overflow events were associated to intense degassing activity. The acoustic pressure, related to the puffing, suddenly increases as soon as the seismic tremor starts to increase. This pattern is common

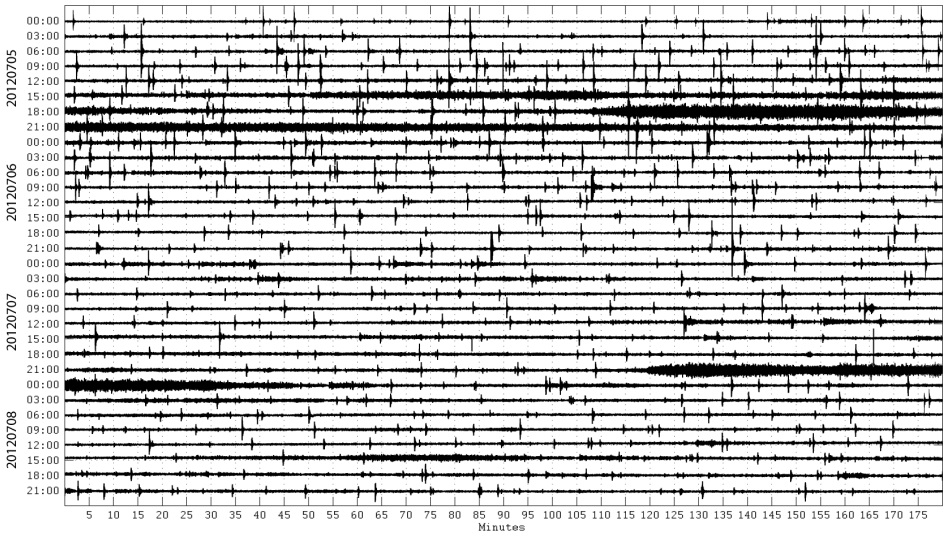

Figure 5.10: Drumplot of 96 hours of record of U/D seismic component at ROC station. Each row is 3 hours long (minutes since row origin time are reported on x axis). Short transients are produced by Strombolian explosive activity while the amplitude of the trace is controlled by seismic tremor component. The phases of high-tremor associated to the overflow occurred on July 5 and July 7, 2012 are marked by the increase of trace thickness.

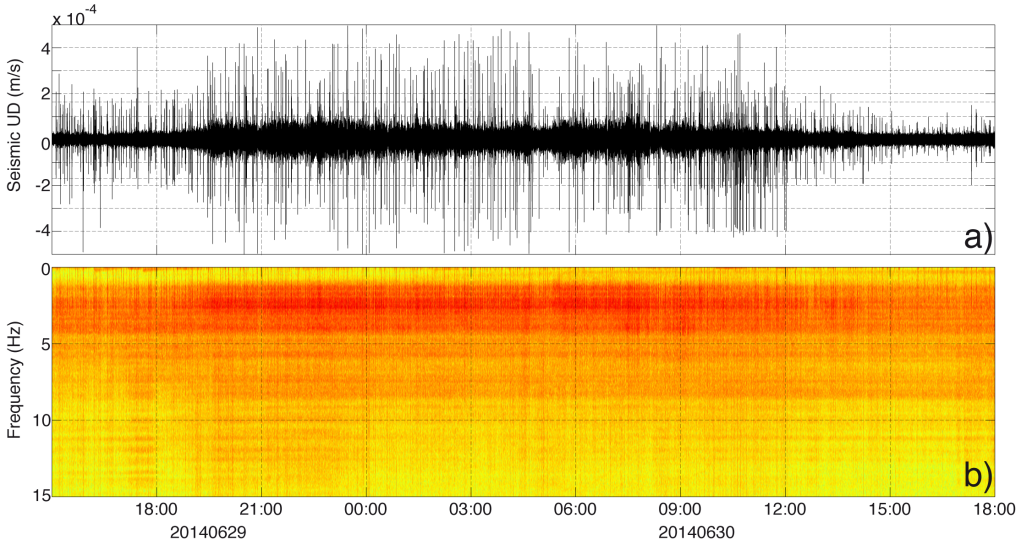

Figure 5.11: Raw seismic trace from ROC station U/D component during the effusive phase of Jun. 29-30, 2004 (up) and related spectrogram in the 0.033 - 15 Hz frequency band (down). No changes of spectral content are evidenced by spectral analysis

over the full data-set and just in a few cases is masked by harsh meteo conditions. In

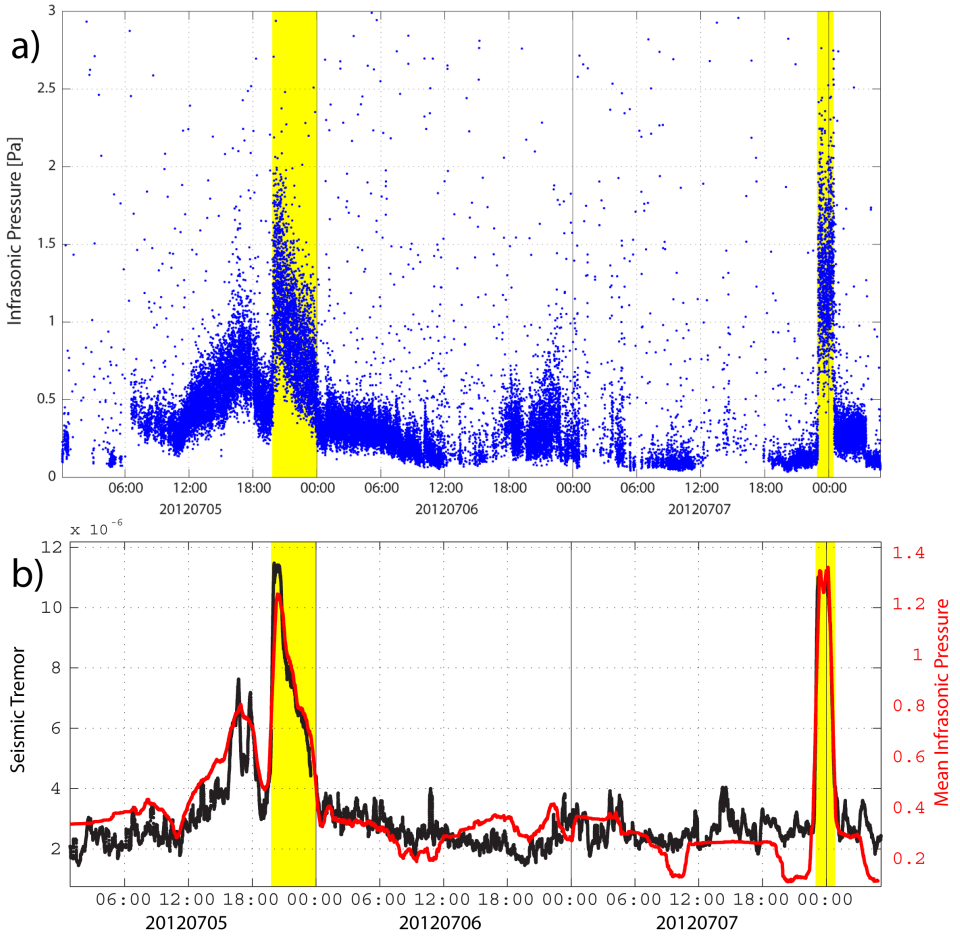

Figure 5.12: a) Infrasound pressures as detected from infrasonic array EAR during. Each dot represent a detection with associated pressure value; b) Comparison between seismic tremor (black) pattern and mean infrasonic pressure amplitude (red) pattern. Yellow patches highlight the periods of overflow activity.

figure 5.12 the pressure of infrasound transients associated to the puffing activity are reported (a), and the averaged amplitude pattern is compared with seismic tremor amplitude (b). The correlation between the two parameters is evident. This correlation, typically observed also during the ordinary Strombolian activity, depends on the coupling of seismic and infrasound sources for degassing processes [94], thus suggesting that the tremor increase is connected with the ongoing degassing activity. The array processing also allows to accurately individuate the source location and tracking the explosive activity from different vents. During the episodes of overflow, the infrasonic degassing shifts towards the vent which is producing the event. This is also consistent with visual observation, indicating sustained spattering activity from the vent producing the overflow. As showed in figure 5.13, this behavior is quite evident from infrasound back-azimuth analysis. During the June-July 2014 interval, represented in figure 5.13, the puffing activity was predominantly located at Central crater (Fig. 5.9). However, concurrently with the overflow episodes, the puffing

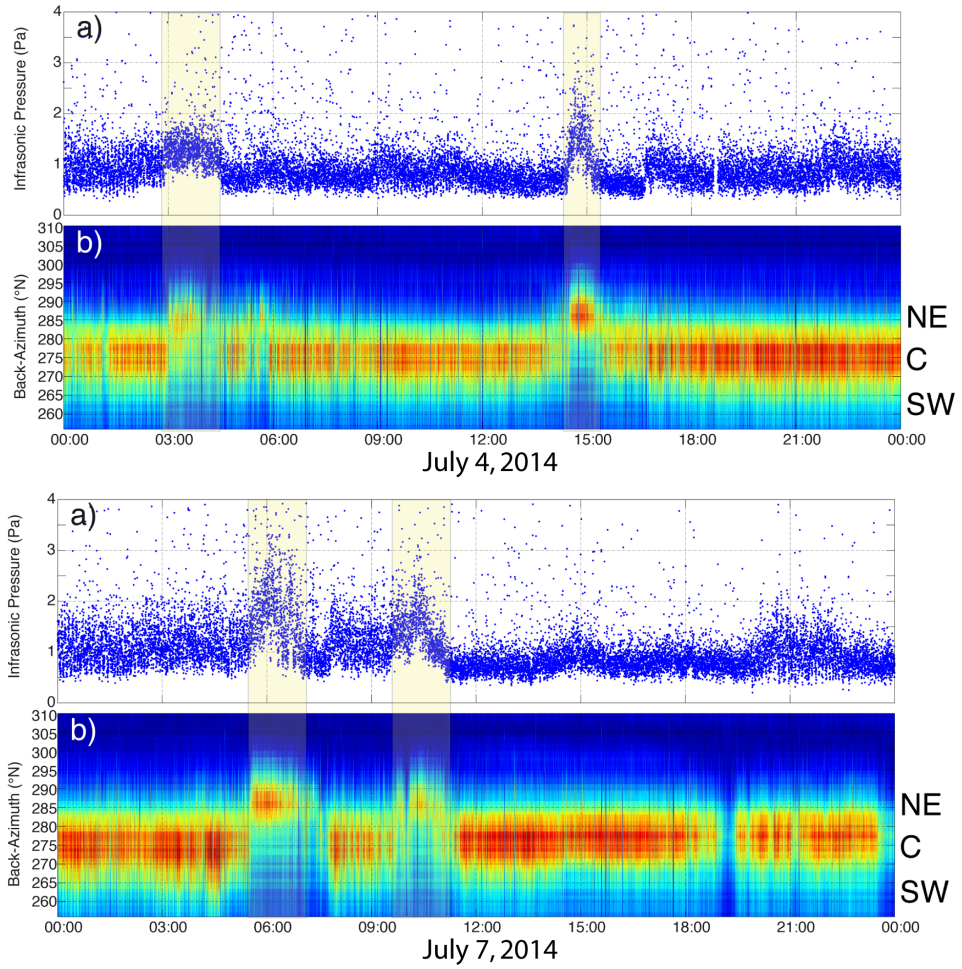

Figure 5.13: Infrasonic pressures (a) and back-azimuth (b) showing the repeated shift of the source position from Central crater to NE crater during overflow episodes occurred in July 4 and July 7, 2014. Light yellow patches highlights the duration of overflows.

activity temporary shifted to the NE crater, from where lava was overflowing. The same pattern of infrasound shift, has been observed during all the remaining events, also during the 2011-2012 and the 2012-2013 phases of overflow activity. In particular, during the Dec. 2010 - Dec. 2012 period, the overflows were mainly produced from the SW crater hornito. Degassing activity was also mostly concentrated at the SW crater. During the effusive phases, activity shifted towards the Central crater. However this apparent shift to the CE was due to the position of the SW hornito, almost in line with Central crater from the point of view of the infrasound array, and rather indicate the shift from the main SW crater to the SW hornito.

5.3.2.3 Thermal imagery

Thermal imagery provides the easiest and straightforward way to observe and follow the development of overflow episodes. The availability of two thermal cameras, one located at ROC station, on the eastern rim of the *Sciara del Fuoco*, and the other at GST site, on the western side of the *Sciara*, allows to cover most of the North-West flank of the volcano. With the only relevant limit of weather conditions, the thermal imagery provides then a reliable monitoring tool, able to observe most of the overflow episodes occurred.
While the camera provides immediate evidences of the ongoing phenomena, the retrieval of quantitative information is instead relatively complicated. The field of view is in fact rather limited and overflows were only partially observed, thus preventing from an estimate of the size.
Camera images, coupled with infrasound-based locations, allowed to precisely constrain the source vent as well as to observe and recognize the relevance of the spattering activity in the generation of overflow episodes. Moreover thermal imagery helps in distinguish between the "active" part of the overflow, when the effusion is dominated by the spattering activity from the "passive" part, when the output decreases and lava flow starts to arrest and cool down. In figure 5.14 a series of thermal images collected from GST camera are reported. Images evidence the spattering activity from the SW hornito and the gradual formation of the overflow, descending about 100 meters down from the crater terrace. As proved by the thermal images, the formation of the overflow is shortly preceded by intense spattering activity, consistently with the analysis of infrasonic and seismic data.

5.3.2.4 Ground deformations

Ground deformation data, provide reliable and useful information during major effusive activity, are rather difficult to extract for minor effusive events. The analysis of tilt data revealed only very small signals correlated to overflow episodes (tab. 5.3). The high sensitivity of the instruments, which allows to record the small transients related to explosive activity, also empower the record of earth-tide related signals [38]. The deformations observed during overflows are often smaller in amplitude than earth tides, often remaining in the noise level of the instruments resulting almost impossible to extract and quantify. However, significant ground deformation associated to several episodes have been detected (tilt column in tab. 5.3). Ground deformations (< 0.25 μrad at OHO) are about two order of magnitude smaller than those recorded for major lava flows (> 10 μrad at OHO). Two different types of

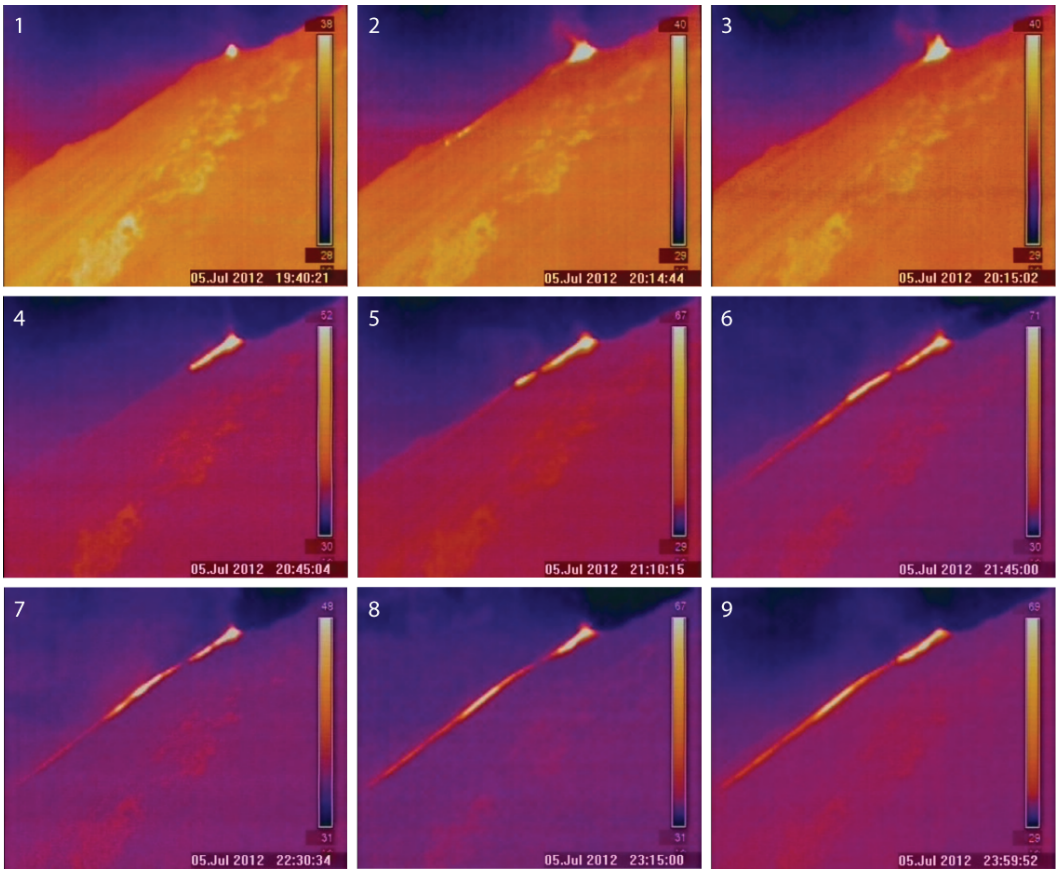

Figure 5.14: Frame shots from GST thermal camera (FLIR A20) pointing towards the crater terrace from the western border of the *Sciara del Fuoco*. Images, taken at different times and with variable inter-times (see timestamp on the frames), allows to track the evolution of the July 5, 2012 overflow. Note the intense spattering activity (from the SW hornito) which starts before the formation of the lava flow. Incandescent blocks rolling down on the slope are visible in frame n.2, indicating that hot magma is accumulating on the crater rim and starts to collapse.

tilt pattern have been recognized. A first pattern, only recorded during the effusive activity of the SW hornito, is characterized by an initial inflation phase followed by a successive, and comparable in amplitude, deflation phase. The full duration of this bell-shaped signal is coincident with the duration of the overflow activity (Fig. 5.15). A second, more common, type of tilt signal is instead represented in

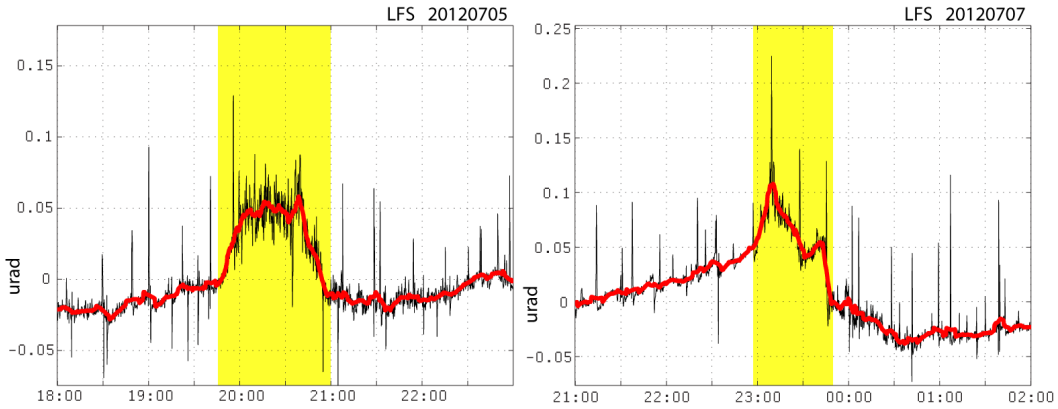

Figure 5.15: Examples of tilt signals recorded at LFS station during the July 5 and July 7, 2012, minor effusive events. Raw data are reported in black and low-pass-filtered in red. Spiky signals in black traces are the VLP component associated to Strombolian activity. Yellow patches highlight the overflow phases.

figure 5.16. In this case, tilt sensor only detected a deflation signal associated to the effusive phase.
This pattern, despite the completely different amplitude, slightly recalls the tilt signal recorded during major effusive crises. In this case, however, the tilt rate is not changing over time following an exponential low, but rather presents a constant slope (Fig. 5.16). Observed ground deformation patterns seem to suggest the presence of

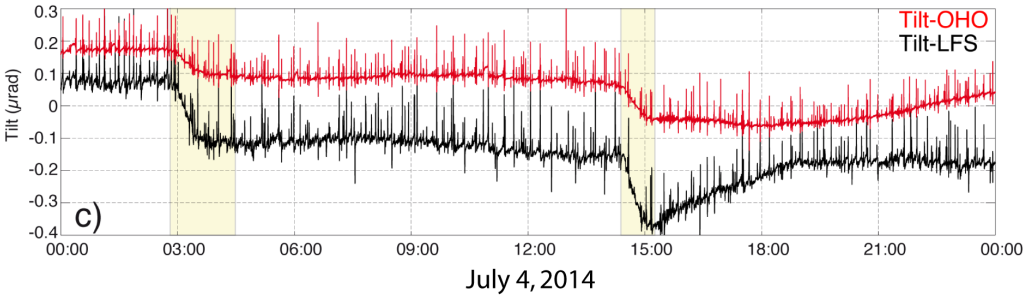

Figure 5.16: One day long tilt record at OHO (red) and LFS (black) stations during the July 4, 2014, minor effusive events (for each station only radial component is plotted). Spiky signals are the VLP component associated to Strombolian activity. Light-yellow patches highlight the overflow phases.

two, slightly different, phenomenologies. When this difference is correlated with the source vent, a possible explanation is found. The effusive activity occurred at the SW hornito. Due to its configuration, with the vent placed several tens of meters above the crater terrace floor, the inflation could be produced by the rise of magma level rise into the shallower conduit, thus producing the observed inflation.

Finally, the linear trend of deflation recorded during the overflow events, indicates that the pressure decrease inside the shallow magmatic system has a linear relation with time, that is, gas and magma release at the surface occur at an almost fixed rate.

5.3.3 Overflows: a geophysical signature

The geophysical parameters, here described using examples extracted from different events, which occurred at different times and from different craters, seems to converge towards a sort of "geophysical signature" of the overflow events. The integration of seismic tremor, infrasonic data, thermal imagery and ground deformation allows to exhaustively characterize these events (at least on the geophysical point of view) and to draw a sort of "geophysical portrait" of a typical overflow event at Stromboli. Moreover, is allows to suggest a theoretical model for these events. As

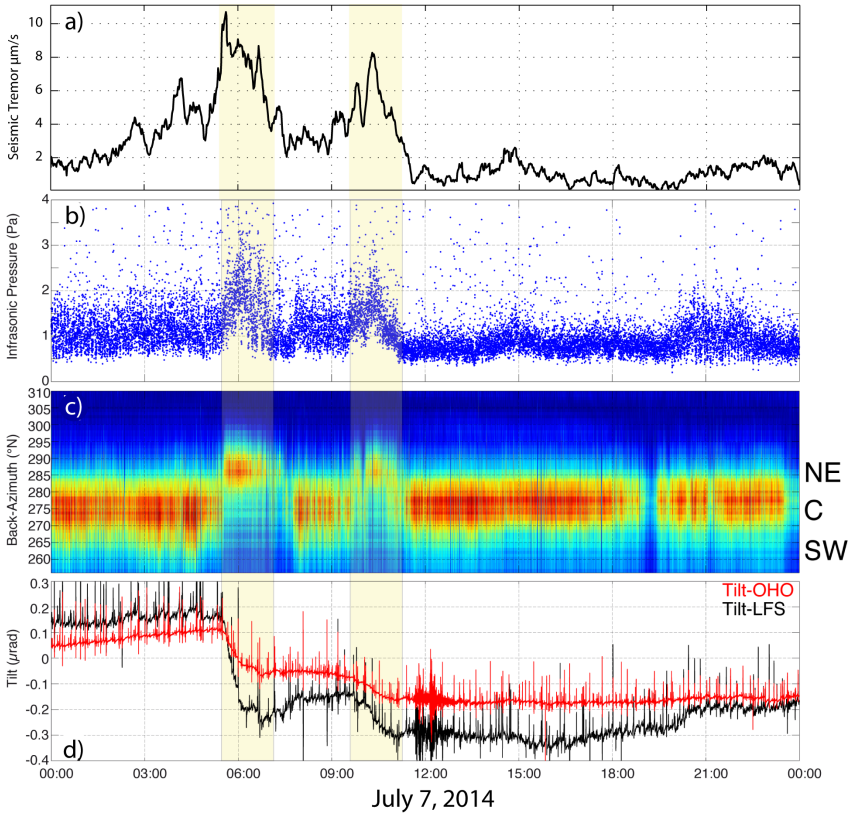

Figure 5.17: Overview of geophysical parameters patterns during a typical overflow event (July 7, 2014). Seismic tremor (a), infrasound acoustic pressure (b), infrasonic back-azimuth (c) and ground tilt (d) are reported. Light yellow colored patches indicate the overflow events. All together these parameters allow to create a sort of geophysical portrait representative of the overflow events.

evidenced in figure 5.17, the overflow event is marked by a substantial and rapid increase of seismic tremor (Fig. 5.17a), associated to an intense degassing activity revealed by infrasound analysis (Fig. 5.17b). The back-azimuth direction of this infrasonic activity (Fig. 5.17c) is consistent with the position of the overflow-

generating vent, and allow to track the sustained spattering activity evidenced in thermal images. Ground deformations recorded during overflow event (Fig. 5.17d), indicate a progressive decompression of the shallow magmatic conduit concurrent with the magma effusion and gas release acted by puffing and spattering. All the geophysical parameters rapidly return to their original values as soon as the event is terminated. The ordinary explosive activity results almost completely unaffected from these events. Appears hence reasonable to interpret these events as the evidence of a rapid increase of gas/magma flux (as indicated by the intense degassing and spattering accompanying the event) which does not interfere with the regular Strombolian activity. This temporary increase of the input rate seems to be generally accommodated by the shallow magmatic system by a simple increase of the level of activity. At the scale of the single event no precursory signal have been identified. No direct relation between the monitored geophysical parameters and the occurrence of the overflow episode can be found in our data-set. However, when observed at a larger temporal scale, the overflow events seems to be associated to conditions of high magma level into the shallow conduits. This is also suggested by the Volcanic Radiative Power (VRP) data provided by MIROVA (Fig. 5.18). The VRP cumu-

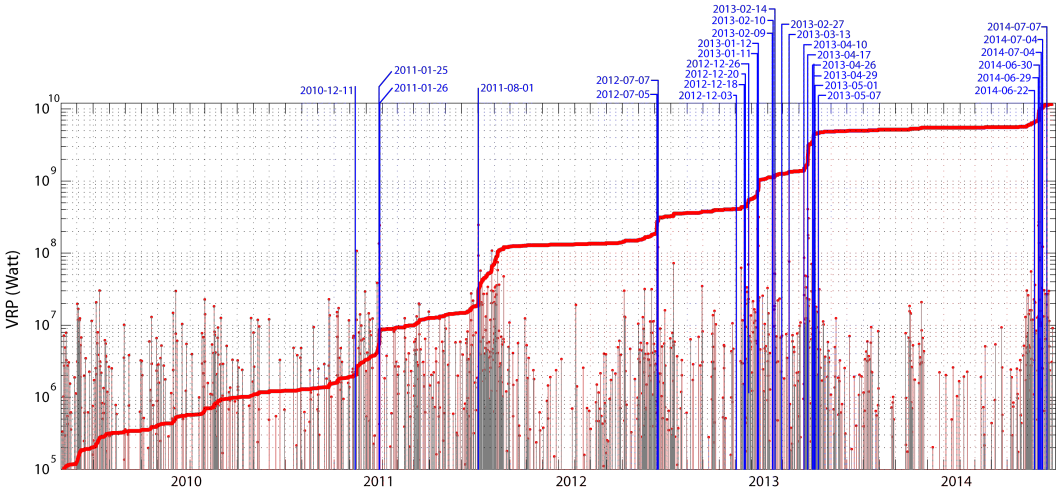

Figure 5.18: Volcanic Radiative Power as single detection (red dots with gray lines) and cumulated (red line). Blue lines mark the occurrence time of overflow events. For each line also the relative date label is reported. Data are from MIROVA system [26]

lative curve in fact shows, at least in several cases, a gentle increase of cumulative VRP, starting weeks to months before the effusive events (Fig. 5.18, July 5 and 7, 2012 events, as an example). A gradual but stable increase of VRP could in fact be correlated with the rise of magma level into the upper conduits. The closer is the magma to the surface, the higher will be the radiative power detected from satellite-based MODIS sensors [28]. Following this consideration is possible to conclude that overflow episodes are more easy to occur during periods of increasing Strombolian activity. The increase of Strombolian activity is in fact reflecting an increase in the gas flux which has follow an increase of input rate from the intermediate magmatic system.

5.3.4 A degassing conduit model for overflow events

While the correlation between high magma level and overflows seems to be relatively obvious, it is worth noting that the recorded episodes appear rather as "active" processes. The over-pressured degassing, recorded by the infrasound array, and driving the observed spattering, is playing in fact a primary role in the vent activity, and the effusive phenomenon appears more as a consequence than a driving force. The impulsive nature of the overflows, developing in a relatively short time, spanning from minutes to hours, but always characterized by an rapid onset, seems to suggests the interpretation of these minor effusive events as the surface manifestation of a deeper process of gas-rich magma degassing. The phase of continuous impulsive degassing, sustaining the spattering activity associated to the overflow resemble,in the due scale, a lava fountaining episode. Following this analogy, the overflow events recorded at Stromboli, are the evidence of pulsatory arrivals of small gas-rich magma batches in the shallow magmatic system, similarly to what is suggested for Major Explosions. In this case, however, the gas is allowed to exsolve and separate from the original magma, thus rising in the upper conduits and manifesting at the surface as short-living, sustained, degassing activity. The degassing activity commonly observed as Stromboli as "puffing" is related to a persistent over-pressurized bubbly flow regime, and is though to be responsible of about 45% of the total gas budget [45]. Position of this activity has been suggested to reflect the position of the main gas bubbly flow channel within the shallow feeding system, which should coincide with the section of the feeding conduit more fluidized by the gas [93]. *Landi et al.* (2011), noticed that whenever puffing is observed to move from the central portion of the crater terrace to lateral vents, an increase of the magmatic temperature is also observed. Since overflow activity was mostly observed from the lateral vents (SW and NE), is reasonable to infer that these effusive episodes are discrete manifestations of a general increase in the input-rate causing the rise of magma level inside the upper conduits, the increase of explosive activity and eventually the sudden degassing of a gas-rich batch producing the observed effusive activity. The fast rise of a stream of bubbles in the shallow conduits produce the rise of the full magma column eventually producing the overflow. As the gas-enriched column degas, the magma level into the conduit gradually decreases finally resulting in the effusive activity complete stop.

5.4 Effusive activity at basaltic volcanoes: the case of Piton de la Fournaise volcano

In this section, the minor effusive events recorded at Stromboli as overflows, are compared with the sustained strombolian and effusive activity recorded at Piton de la Fournaise volcano in October 2015. During the last phases of the 2015 eruption of Piton the la Fournaise eruption , an infrasound array was in fact installed on the volcano to monitor the ongoing activity. The preliminary results of this campaign are here presented as term of comparison for the geophysical parameters recorded at Stromboli during overflow episodes. Despite the different scale and location, the events show in fact similarities and differences which can help to better understand Strombolian effusive events as well as to include the activity of Stromboli in the

more wide context of the basaltic volcanism.

5.4.1 The October 2015 temporary infrasound array deployment

On August 24th 2015, a 67 days long eruptive activity started at Piton de la Fournaise Volcano. During the last phases of the eruption we deployed a portable, small aperture, infrasonic array which allowed us to record unprecedented data from effusive volcanic activity. The array consisted on four, few tens of meters spaced, infrasound pressure sensors and it was installed on the outher rim of the Enclos Foqué, roughly 2.5 km far from the active vent, sited on the southern flank of the Dolomieu cone. The system was almost continuously operating from October, 15th to December, 7th 2015, thus recording the end of the first eruptive phase (Autust 24th - October 17th) as well as the two short-living following phases (from 22 to 24 and from 29 to 31 October, 2015). The infrasound records have been coupled with discrete high-rate (30 Hz) thermal and visible imagery acquisitions located at a short distance from the vent (100-200 m) providing detailed information on the infrasound source dynamics. The comparison with seismic and ground tilt data recorded by the permanent network operated by the Observatoire Volcanologique du Piton de la Fournaise (OVPF), allows for a detailed analysis of the shallow magma dynamics during the effusive activity at Piton de la Fournaise Volcano.

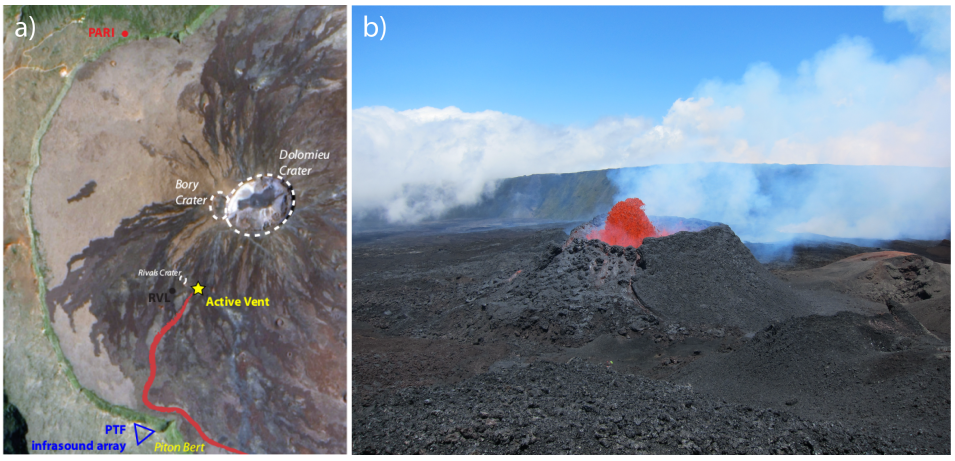

Figure 5.19: a) Map of Piton de la Fournaise summit area with main craters (Dolomieu and Bory), active vent position (yellow star) and PTF temporary infrasound array (red triangle), RVL seismic station (OVPF) and PARI tiltmeter site (OVPF); b) picure of the active vent taken during the October 16, 2015 activity. The infrasound array was located on the caldera rim, just behind the active vent in this picture, about 2.5 km far.

5.4.2 The October 2015 eruptive activity

The August-October 2015 eruption of Piton de la Fournaise volcano started on August 26 with the opening of a new eruptive fissure on the southern flank of the Central cone, inside the Enclos Foqué. The activity gradually shifted towards the lowest end of the fracture, where it lasted until October 18, creating a small cone, about 120 meters large and 50 meters high. At this date, suddenly, the eruptive

activity ceased. After about five days of complete rest, the activity restarted again at the same crater lasting for about 42 hours and then suddenly arrested once more time. Six days after a new reprise was recorded for a duration of 35 hours. After that, the activity ceased completely and the 2015 eruption went over. The eruptive activity was characterized by continuous strombolian-like explosive activity from the cone summit and well alimented lava flow from a separate, lateral vent, at the base of the cone. *Pioli et al.* (2009), suggested that this synchroneity of explosive and effusive activity is a key characteristic of violent strombolian activity typical of water-rich basaltic volcanoes [85]. This style of activity is typically discontinuous and pulsatory, as observed during the conclusive phases of Piton 2015 eruption.

5.4.3 Geophysical data: analysis and results

The PTF infrasound array was first installed on October 15th. After the severe damage caused by a wildfire started by the lava flow on the 24th, it was quickly re-installed on October 25th and was operative until December 9th. The resulting dataset covers the last days of the main effusive phase (phase 1) and the successive two short-living eruptive phases (phase 2 and phase 3). Beside the infrasonic data, also seismic and tilt data were available, provided by the *Observatoire Vulcanologique du Piton de la Fournaise* (OVPF). In figure 5.20 is showed a synoptic view of the full data-set analyzed in this work. The two short-lived eruptive phases occurred on October 22 - 24 and 29 - 31, were very similar in style and development of the activity. Accordingly, geophysical data-set shows also relevant similarities. The activity started with the re-opening of the effusive vent, marked by scattered, small explosive events recorded by infrasound array as discrete transients. This reprise of the activity was also accompanied by a gradual increase of seismic tremor. This initial phase, lasting 1-3 hours was followed by the main explosive and effusive phases, continuing, at almost constant intensity for several hours (35 or 42, respectively for the Oct. 22 - 23 and the Oct. 29 -31 episodes). The infrasound and seismic time-series are showed in figure 5.21. An almost identical pattern was detected during Oct. 22 - 24 event. The processing of infrasonic array data, allows to locate the source and extract the pressure of the transient. Then, an appositely written code, was used to detect and count the number of pulses per minute. The pulsatory nature of the infrasound signal is in fact evident and visible in figure 5.22a (inset). Elaborations show that, after a rapid increase, the rate of explosive events stabilize at a value of about 40 pulses per minute, thus remaining stable until the sudden end of the eruptive phase (Fig. 5.22a). The comparison between infrasound pseudo-energy, computed as the product of number of events per minute and mean amplitude of pressure, and seismic tremor amplitude, shows that the two parameters follow a very similar pattern (Fig. 5.22b). The rapid increase of seismic tremor, number of events and associated pressures at the onset of the eruptive phases, suggest the gradual but fast increase of gas flux. This is consistent with the emergent reprise of the activity observed from cameras and visual observations. The detailed analisys of ground deformation (tilt) data form PARI (Fig. 5.19) borehole station (OVPF), shows that the two eruptive phases are accompanied by a remarkably similar deflation trend. Tilt signal, recording inflation until the onset of the activity, reverts to deflation as the eruption starts. The deflation process follows a linear trend (i.e. constant rate). Surprisingly this

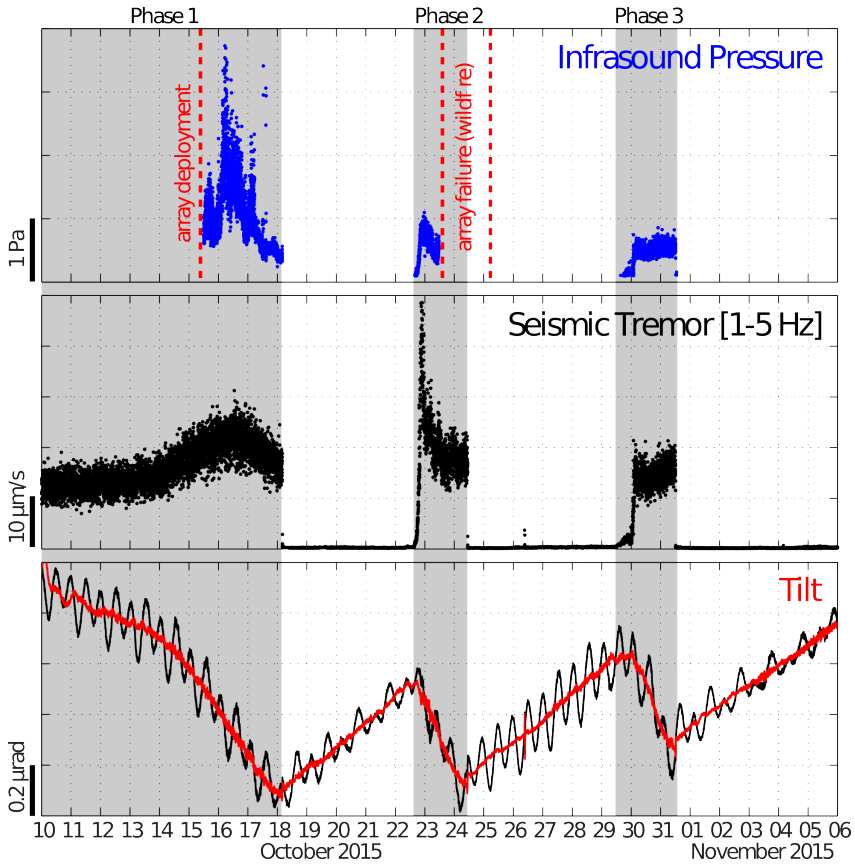

Figure 5.20: Synoptic view of Infrasound data (up), seismic tremor (middle), and ground tilt (low). Ground tilt is plotted bot as raw (black) and cleaned from earth tides signals (red). Seismic and tilt data are a courtesy of *Observatoire Vulcanologique du Piton de la Fournaise* (OVPF). Gray background indicate the eruptive periods. Red dashed lines mark the deployment and the temporary destruction of the PTF infrasound array.

trend is almost identical for the two events (Fig. 5.23b). The same correlation is also maintained during the inflation phases, recorded in the inter-eruptive time (Fig. 5.23a). The constant tilt rate during the inflation phase, evidenced by the linear inflation trend, indicates that the magma recharge during the inter-eruptive interval occurs at a constant rate. The fact that the slope is the same for the two phases suggests that the arrival of new magma in the shallow magmatic system continued at a constant rate over a relatively long time. The constant deflation rate, instead, indicates that magma/gas release at the surface was also almost constant. This is in good agreement with seismic and infrasonic observations, suggesting a rather stable process of gas and magma release.

5.4.4 Comparison with Strombolian overflow episodes

Discarding the obvious differences between Piton de la Fournaise and Stromboli, the comparison is here focused on the geophysical data-set recorded during minor effusive (overflow) events at Stromboli and sustained explosive, and effusive, activity during the terminal phases of 2015 eruption of Piton de la Fournaise volcano. De-

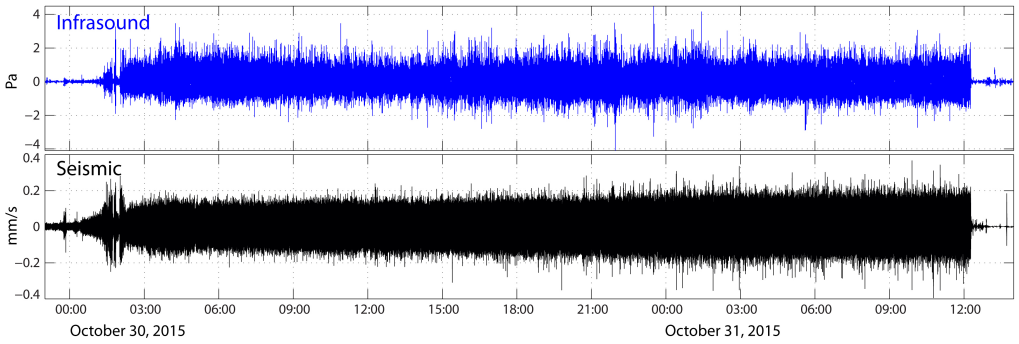

Figure 5.21: Infrasound (blue) and seismic (black) traces from eruptive phase of Oct. 29 - 31, 2015 at Piton de la Fournaise volcano. The gradual increase of seismic velocity and infrasound pressure characterize the initial phase of the explosive-effusive event. Pressures and velocities remain almost stable for the whole duration of the eruptive phase and finally drop suddenly as the activity cease.

spite the different magnitude, the two phenomena show in fact several similarities, as well as relevant differences. Due to its open-conduit conditions, Stromboli volcano often represented the ideal volcanological laboratory. Its persistent Strombolian activity, so generous in providing large data-sets of valuable data in short time, creates, on the other hand, a sort of "noisy background" for the geophysical observations of over-imposed phenomena such as minor overflows. The discontinuous activity recorded at Piton de la Fournaise, by contrast, provides a very quiet environment to investigate the dynamics of these phases of strombolian-effusive activity without the inference of any different source of signals. As evident in figures 5.20 and 5.23(a and b), ground deformation, coupled with infrasound and seismic analysis, provide the evidence that the shallow magmatic system can be thought as "sealed" during the inter-eruptive phases. This observation is in fact consistent with the complete absence of infrasound and seismic signals as well as the continuous inflation trend indicating the presence of a constant magma input. Once the activity starts, the system becomes open and gas and magma release at the surface initiate, producing sustained strombolian explosive activity and degassed magma output from the base of the cone. This behavior is commonly observed on several water-rich basaltic volcanoes, and is interpreted as the evidence of partitioning of gas and liquid fluxes at very shallow depth [85].
The gas release at the vent, alimenting the Strombolian activity, occurs at a stable rate of one event every 1-2 seconds. This rate is substantially the same recorded for the puffing activity at Stromboli [97]. This rate is also typical of the spattering activity accompanying the overflow episodes here analyzed. Furthermore, the linear tilt deflation pattern associated to the fountaining/effusive phase, and astonishingly similar for both phase 2 and 3, closely recalls the deflation signals recorded at Stromboli during the overflow events. The main difference, in this case, is represented by the longer duration and the much larger emitted volumes. Seismic and infrasonic data-set also reveal interesting analogies with Stromboli overflow data. The abrupt increase of seismic tremor, concurrent to the rapid increase of infrasonic activity and associated to the sustained Strombolian activity from the eruptive vent, resembles

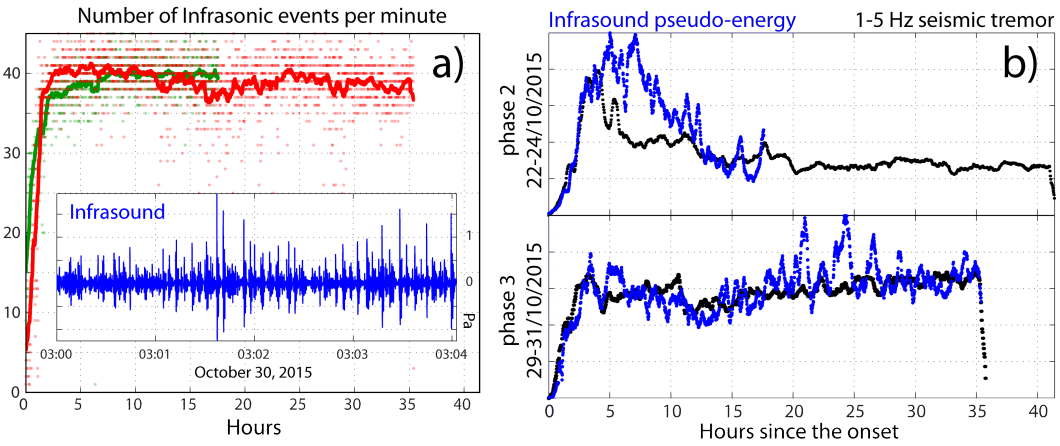

Figure 5.22: a) Number of events per minute during the two explosive-effusive phases of Oct. 22 - 24 (green) and Oct. 29 - 31 (red), 2015. In the inset a 4 minutes long sample of infrasound data trace is plotted to show the impulsive events counted to produce the main graph; b) Comparison between infrasound pseudo-energy (blue) and seimsic tremor (black) during the two eruptive phases. Infrasound pseudo-energy is computed as the product of number of events and mean squared amplitude in one-minute-long windows. Seismic tremor is computed in the 1-5 Hz frequency band.

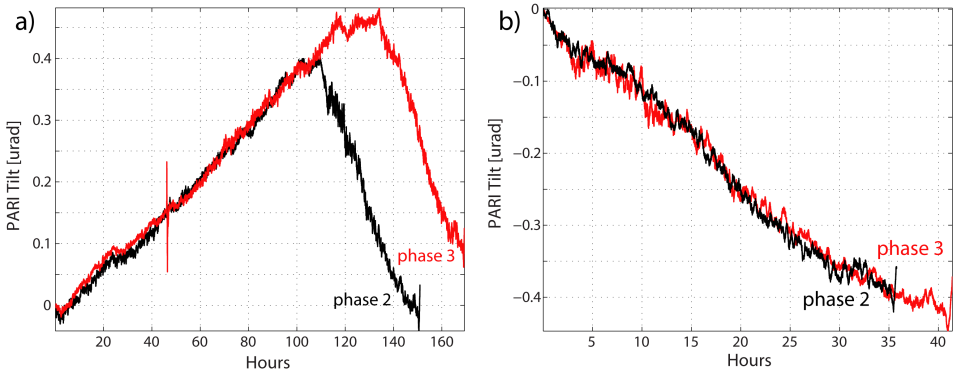

Figure 5.23: Tilt data recorded during the Oct. 22 - 24 (black) and Oct. 29 - 31 (red) eruptive phases. In (a) tilt pattern of inter-eruptive and co-eruptive phase is presented. Time, in hours, start from the end of the precedent activity. Note the almost perfect overlap of the tilt pattern during the inflation phase. In (b) the two deflation trend accompanying the eruptive phases are compared. Also in this case the two pattern almost overlap.

the spattering activity observed at Stromboli.
The comparison between Piton de la Fournaise intermittent activity and Stromboli overflows suggests that the two eruptive manifestations share a similar source process of gas/magma flux release. The sustained spattering of Stromboli during overflow episodes is here suggested to be equivalent to the violent strombolian explosive activity recorded at Piton during the analyzed eruptive phases.

5.5 Notes on the interpretation of ground deformation in open-conduit systems

Ground deformations recorded during volcanic activity are commonly associated to pressure or volume sources, and therefore interpreted as the evidence of magma emplacement, displacement , outplacement, and degassing in the magmatic system [32]. The movement of magmatic fluids inside the volcanic edifice results in surface deformation that can be detected and measured with the appropriate methodologies, thence, the use of inverse modeling, allows to reconstruct the source position and its behavior starting from the collected data.
Open-conduit volcanoes, represent a particular case where the magmatic system is directly connected to the source through a relatively complex feeding system and are not the exception for ground deformation. Nonetheless, in figure 5.3, tilt data, although incomplete, clearly show that the increase of explosive activity, interpreted as the rise of magma level inside the conduits, only produce a negligible signal. While this is apparently counter intuitive, it is important to consider that ground deformations in open conduits systems do not strictly reflect the input rate and deflations are not directly proportional to output rate.
As a very simplified approach, tilt can be though as proportional to the difference between output volume and input volume: $\tau = V_{in} - V_{out}$. In an open-conduit system, under ordinary persistent activity conditions, the sum of these two components is always equal to zero ($V_{in} \simeq V_{out}$). An increase of the deep input will in fact simply result in a comparable increase of the output rate, both in terms of gas or magma. At least in the shallow magmatic system, no major changes are expected unless the change is too fast or too big to be accommodated by the change volcanic activity level. Unless a relevant change in the magma level inside the conduit occurs (such as in case of major lava flow), no particular tilt signal are thence expected to be recorded.
This is completely different from what is commonly observed in closed-conduit system, where during inter-eruptive phases the activity is almost null ($V_{out} \simeq 0$) and the activity is often preceded by an inflation caused by the recharge of the system ($V_{in} > 0$). Then, as soon as the activity starts ($V_{out} > 0$), negative tilt is recorded as far as the output rate is larger of the input rate ($V_{in} < V_{out}$). Therefore, the open-conduit case represent the most difficult situation for the measure and interpretation of the ground deformation data. In such conditions the observed pattern always represent in fact the balancing of the two terms. A change in the input rate will induce, or will not induce, ground deformations depending on the possible change of the volcanic activity to adapt to the new conditions. On the other hand, a detected signal could be the evidence of the change of both the terms. In this frame,

the integration with the other geophysical parameters, which allows to monitoring and quantify the changes of the eruptive activity may provide the key to interpret the presence (or absence) of relevant deformations.

5.6 Conclusions

In this chapter, the two types of effusive activity commonly recorded at Stromboli volcano are analyzed in detail. The correlated geophysical data-set highlight substantial differences between the two phenomena. The lava flow activity, more relevant in terms of emitted volumes and duration, is explained with a gravity-driven magma draining process, due to the opening of a new vent at lower elevation respect to the summit craters. In this scenario, the relevant increase of Strombolian activity that precedes the effusive phase is interpreted as the trigger for the opening of the new vent.
Concerning the short-lived overflows, that have been fully characterized from the geophysical point of view, detailed analysis evidenced the "active" nature of these events. Overflows, differently from major effusive crises, are rather produced by a transient, sustained, degassing activity associated to intense and continuous spattering from the effusive vent. The geophysical evidences indicates that, during this episodes, the shallowest magmatic system is interested by a transient, short-living increased gas flux that sustain the effusive activity. This sudden increase of puffing activity and seismic tremor are produced by this increased flow rate into the upper conduits. The abrupt increase of degassing activity as the overflow starts, and the evidence that this increase is not recorded by a change of the regular explosive activity, which continues unaffected, suggests that there is no genera increase of the magma input-rate. This concentrated degassing is rather thought to be linked to a transient increase in the gas flux that, decoupled from magma, rise into the upper conduits. This sudden and localized variation of the gas flux conditions may reflect the arrival of a small gas-rich magma batch into the shallow magmatic system ans the consecutive gas exsolution and segregation.

Chapter 6

Final remarks

The activity of open-conduit basaltic volcanoes is controlled and modulated by gas/magma flux. In these systems, gas does not accumulate in the shallow magmatic system, but rather escape from the upper conduit, driving the persistent degassing activity. The Integrated geophysical monitoring allows to detect, and measure in real-time, the possible variations of gas flux into the shallowest portion of the magmatic system. At Stromboli, characterized by persistent Strombolian activity, small variations of magma/gas flux are recorded as subtle and gradual changes of monitoring parameters. Occasionally, abrupt and relevant changes are recorded for "anomalous" events, clearly differentiating from the ordinary Strombolian activity by intensity or style. The detailed analysis of these events, namely effusive crises, overflow, paroxysms and major explosions, provides consistent results, resulting in a new step towards the understanding of the plumbing system dynamics and the interaction between deep and shallow portions of it.

For each chapter, the results of the treated arguments have been already presented in detail and discussed in a dedicated section. Here, a summary of the principal conclusions is presented, listed per topic.

Case studies Both field experiments, illustrated in *Chapter 2*, provided interesting and valuable results.
Concerning the high-speed camera experiment, the developed methodology allows to reliably translate luminance images into acoustic pressure traces. The effectiveness of the method has been demonstrated by the comparison with infrasound data. Moreover, looking at the close proximity of the vent, the evidences of super-sonic dynamics during the gas thrust phase have been found.
The radar experimentation provided clear evidences that ground displacement produced by the Strombolian activity can be successfully detected and measured using ground-based fast-sampling radar interferometry techniques. Displacements up to several millimeters, reversing their polarity on the two sides of the exploding vent position, were recorded for every explosive event. The observed pattern of deformation revealed the rapid inflation of the upper part of the conduit followed by a progressive contraction. From the comparison with the thermal imagery is shown that the ground inflation starts a few seconds before the onset of the explosion and culminates just before of it. The contraction phase in instead accompanying the release of gas and fragments from the conduit and consistent with a pressure decrease into the shallowest section of the conduit. However, the more interesting results arise from the comparison of ground deformation- related-measures (seismic VLP displacement and tilt). While seismic VLP displacement and radar-derived displacement waveforms are almost overlapping in the same VLP frequency band, the amplitude of observed deformations differs in terms of amplitude. The radar signals show in fact, a magnitude $\sim$250 times larger than the seismic ones. Even under the hypothesis of a large local effect, such a difference in amplitude could hardly be explained assuming a source position located 200 m below the surface. In this case, in fact, the distance between the source and the vent, or between the source and the seimic sensor will be in the same order of magnitude (200 m vs. 400 m).
Finally, an even more relevant information arises from the observation that the VLP

signals related to the activity of the SW vent are not detected by the radar when illuminating the NE side of the terrace. Only a very local source could produce such a deformation pattern forcing to conclude that the deformation recorded by the radar is produced by a very local source which is almost coincident with the vent position.

Explosive Activity Major explosions and Paroxysms represent the most energetic explosive manifestation of Strombolian activity. When individually observed, explosive dynamics seem to show complexities and over-imposition of multiple events and phenomena, each one contributing to the characteristic geophysical signature of each event. The integration of different geophysical data-set allowed to characterize the event about timing, explosive dynamics and, finally, to extract some inference on the shallow magmatic system and even the source process. Tilt data presented in this work, disclose new insights on this type of events, evidencing how, major and paroxysmal events, share the same inflation pattern. This geophysical evidence unambiguously demonstrate the existence of a common dynamic process, resulting in the observed common pattern of ground deformation. This pattern is scalable in amplitude, and compatible with pressure increase inside the shallow magmatic conduit prior to the explosion. This emergent signal of pressure increase can be detected at least 500 seconds before the explosive onset.

Effusive Activity Two distinct types of effusive activity are observed at Stromboli. The integrated geophysical analysis highlights substantial differences between the two phenomena. The lava flow activity, more relevant in terms of emitted volumes and duration, is explained with a gravity-driven magma draining process, due to the opening of a new vent at lower elevation respect to the summit craters. In this scenario, the relevant increase of Strombolian activity that precedes the effusive phase is interpreted as the trigger for the opening of the new vent.
On the other hand, for the short-lived overflows, the detailed geophysical analysis evidenced the "active" nature of these events. Overflows, differently from major effusive crises, are in fact produced by a transient, sustained, degassing activity associated to intense and continuous spattering from the effusive vent. The geophysical evidences indicates that, during this episodes, the shallowest magmatic system is interested by a transient, short-living increased gas flux that sustain the effusive activity. This sudden increase of puffing activity and seismic tremor are produced by this increased flow rate into the upper conduits.

Appendix A

How to derive tilt from seismometer

Despite the fact that most of the seismometers output is expressed as ground velocity, a seismic sensor is actually sensitive to acceleration. Working on the inertial pendulum design, and hence on the first principle of dynamics: *Corpus omnes perseverare in statu suo quiescendi vel movendi uniformiter in directum, nisi quatenus a viribus impressis cogitur statum illum mutare;*, seismometers use the response of an harmonic oscillator maintained in equilibrium to the external forces. Perturbations of this state depend on the changes of one or more of the forces acting on the system. A common seismometer is constituted by three independent sensors, with sensitive axis aligned along the three directions defining a three-dimensional space. Despite all the three sensors are based on the same principle of damped pendulum, the governing equations subtly but substantially differ between horizontal and vertical components. The differential equations describing the two horizontal component can be written as [41]:

$$\ddot{x}_1 + 2\omega_0 D\dot{x}_1 + \omega_0^2 x = -\ddot{u}_1 + g\tau_2 - \ddot{\tau}_3 l_1 + \ddot{u}_2\theta_1 \tag{A.1}$$

$$\ddot{x}_2 + 2\omega_0 D\dot{x}_2 + \omega_0^2 x = -\ddot{u}_2 + g\tau_1 - \ddot{\tau}_3 l_2 + \ddot{u}_1\theta_2 \tag{A.2}$$

where:
x_i is the horizontal displacement recorded by the seismometer,
ω_0 is the angular frequency of the sensor,
l_i is the length of the pendulum arm,
θ is the rotation angle of pendulum,
D damping,
u the real displacement of ground,
g gravity force,
τ_i rotation around the i axis.

These equations are valid for $\sin\tau_i \approx \tau_i$, a condition which is respected for very small angles. Here the acceleration caused by tilt is proportional to $g\sin\tau$, while for the vertical pendulum it will be $g(1-\cos\tau)$ and $\cos\tau \approx 1 - \frac{\tau^2}{2}$.
Thus the equation for the vertical component will be written as:

$$\ddot{x}_3 + 2\omega_0 D\dot{x}_3 + \omega_0^2 x = -\ddot{u}_3 + \frac{g}{2}\tau_1^2 - \ddot{\tau}_1 l_3 + \ddot{u}_2\theta_3 \tag{A.3}$$

Similarly to the horizontal components, the vertical component is also sensitive to accelerations along the axis ($\ddot{u}$), angular accelerations ($\ddot{\tau}l$), cross axis displacements *cross-axis*($\ddot{u}\theta$), and acceleration due to ground tilt tilt ($g\tau$). Tilt sensitivity, however, is less pronounced for vertical component than for the horizontal. Different designs can reduce or even cancel the effects of non-axial components (which are however negligible for most of the applications), but not tilt. Tilt is in fact negligible, even for very small angles, only on the vertical component.

$$\begin{aligned}
\ddot{x}_1 + 2\omega_0 D\dot{x}_1 + \omega_0^2 x &= -\ddot{u}_1 + g\tau_2 \\
\ddot{x}_2 + 2\omega_0 D\dot{x}_2 + \omega_0^2 x &= -\ddot{u}_2 + g\tau_1 \\
\ddot{x}_3 + 2\omega_0 D\dot{x}_3 + \omega_0^2 x &= -\ddot{u}_3
\end{aligned}$$

Let's now suppose that both, ground displacement and tilt, behave as harmonic oscillations such as: $u = u \circ e^{-i\omega t}$, $\tau = \tau \circ e^{-i\omega t}$; when the seismometer is excited by the external motion, the horizontal component will respond:

$$x(\omega_0^2 - \omega^2 - 2iD\omega_0\omega) = \omega^2 u + g\tau$$

and, splitting the contributions of displacement and tilt:

$$x(\omega) = \frac{w^2 u}{\omega_0^2 - \omega^2 - 2iD\omega_0\omega} + \frac{g\tau}{\omega_0^2 - \omega^2 - 2iD\omega_0\omega},$$

from this, sensitivity of the seismometer to displacement can be easily obtained [101]:

$$|\frac{x}{u}(\omega)| = \frac{\omega^2}{((\omega_0^2 - \omega^2)^2 + (2D\omega_0\omega)^2)^{1/2}},$$

while the sensitivity to tilt is:

$$|\frac{x}{\tau}(\omega)| = \frac{g}{((\omega_0^2 - \omega^2)^2 + (2D\omega_0\omega)^2)^{1/2}},$$

The ratio between the two sensitivities can be expressed as:

$$|\frac{x/\tau}{x/u}| = \frac{g}{\omega^2} \tag{A.4}$$

from which it can be derived:

$$A_T = \frac{g}{\omega^2} A_D. \tag{A.5}$$

This formula allows, if the displacement response function is known, to deduce the tilt response function, under the assumption that also tilt is dependent on the angular frequency [101].

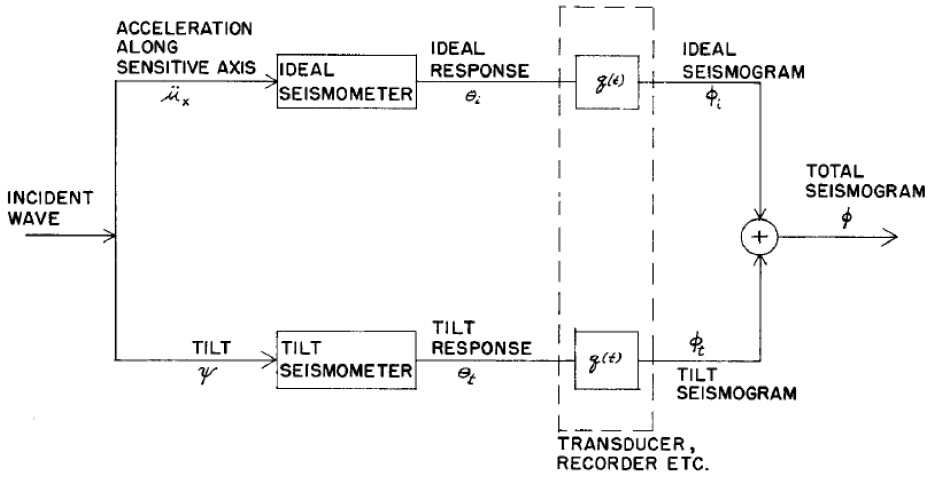

Figure A.1: Block diagram illustrating construction of total seismogram (from Rodgers, 1968 [101]).

From the equations it is obvious how, for the same tilt angle, its effect on the sensor output will change with the changing angular frequency. That is, tilt component will became more and more relevant for periods comparable with the lower corner frequency of the instrument. When the tilt variations occur with a period much longer than the sensor period, the response of the sensor can be considered as simply proportional to the tilt angle. This is more commonly written in the form:

$$\ddot{x}_i = -g\tau \quad , i = 1, 2 \tag{A.6}$$

where the acceleration recorded by the seismometer is considered as directly proportional to the tilt angle scaled by g. This statement can be considered as correct when tilt is not a function of time, i.e. tilt variations occur with a period much longer than the sensor period.

Hence a seismic sensor based on the damped pendulum is theoretically sensitive to tilt. While it is shown that rotations can affect significantly the movement of the mass for the horizontal components, has to be understood which output will produce them. The mass movement is measured by a transducer with an own transfer function, which has to be taken into account to retrieve the transfer function of the instrument itself. For an induction transducer, the output voltage will be proportional to the mass velocity for frequencies above the corner frequency. At lower frequencies tilt cannot be detected. Modern broad-band sensors largely used the force-balance design. This allows to extend the period and enhance the response linearity.
The force acted by the displacement of the mass from its equilibrium position is compensated by an opposite force electrically generated. Basically the mass of the sensor is forced to move as much as possible accordingly with ground. The position of the mass is detected by a capacitive transducer and represents the basic signal of such a sensor. This signal is used to produce the balance force as a feedback. This force is thus proportional to the acceleration experienced by the mass. The same signal, once integrated, represents the velocity output of the sensor, as illustrated in the sketch A.2.

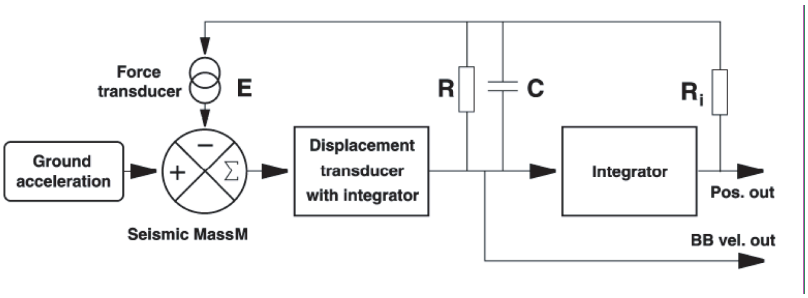

Figure A.2: Conceptual sketch of a force-balance seismometer.

A small DC acceleration, such as the one produced by tilt, will results in a small permanent signal following a linear relationship. If the output signal is not low-pass-filtered, this information will be preserved as a permanent offset.

Static factor to convert millimeters to microradians can be easily calculate from eq. A.5, under the approximation of an ideal seismic sensor. A theoretical factor of 4.4714 μrad/mm can be found using eq. A.5. A more accurate computation can be obtained using the distribution of poles and zeros of the sensor $(p_i, z_i, i = 1, 2, 3)$ using the formula:

$$C_v(\omega) = -0.314 \frac{(i\omega - z_1)(i\omega - z_2)(i\omega - z_3)}{(i\omega - z_1)(i\omega - p_2)(i\omega - p_3)}, \tag{A.7}$$

where $C_v(\omega)$ is the velocity impulse step function [5]. From this equation, accord-

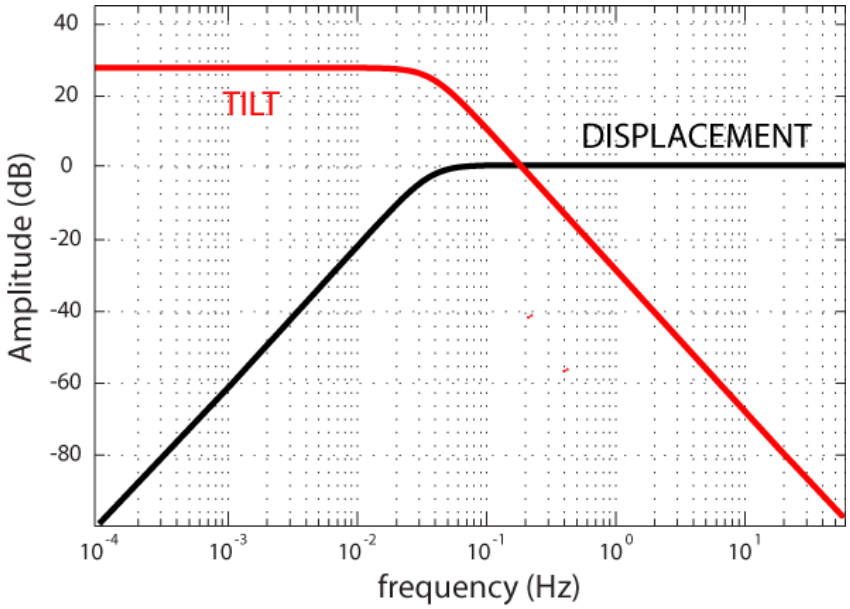

Figure A.3: Theoretical response of a Guralp T40 30s seismometer to displacement and tilt.

ing to the relation already introduced A.4, the theoretical amplitude of the response to a tilt step change can be calculated. As discussed, a constant amplitude response is expected in the frequency range below 0.033 Hz, which is the natural frequency of the CMG-40T 30s seismometer. Using this frequency in equation a value of 4.48 μrad/mm is obtained. This value is almost identical to the one obtained for the ideal seismometer (4.47). This amplitude factor can be used as a transfer constant between the apparent displacement due to tilting and the angle of tilt change [5]. In figure A.3 the theoretical response of a Guralp T40 30s seismometer to displacement and tilt is reported.

Acknowledgments:

This work would not have been possible without:

The close cooperation of the entire LGS group;

The generous support of the scientific and technical personnel of the *Observatoire Volcanologique du Piton de la Fournaise (FR)*;

The fruitful collaboration with *Prof. T. Nishimura* from Geophysics Department of *Tohoku University (JP)*;

The manuscript has been improved by the comments of two reviewers: Prof. D. Legrand *(Universidad Nacional Autónoma de México)* and Prof. S. De Angelis *(University of Liverpool)* and the selfless revision of Prof. G. Napoleone.

To all those who deserve it, but I forgot to thank: thank you!

Bibliography

[1] Agnew, D.C., Strainmeters and Tiltmeters, *Rev. Geophys.*, 24(3), 579-624, 1986.

[2] Allard P., 2010, A CO2-rich gas trigger of explosive paroxysms at Stromboli volcano. Journal fo Volcanology and Geothermal Research, 189, 363-374.

[3] Allard P., Carbonnelle J., Métrich N., Loyer H., and Zettwoog P., 1994, Sulfur output and magma degassing budget of Stromboli Volcano. Nature 368, 326-330.

[4] Aloisi M., Bonforte A., Mattia M., and Puglisi G., 2008, Ground Deformations Related to the Effusive Eruptions of Stromboli: The 2002?2003 Case, in The Stromboli Volcano: An Integrated Study of the 2002-2003 Eruption (eds S. Calvari, S. Inguaggiato, G. Puglisi, M. Ripepe and M. Rosi), American Geophysical Union, Washington, D. C..

[5] Aoyama H., and Oshima H., 2008, Tilt change recorded by broadband seismometer prior to small phreatic explosion of Meakan-dake volcano, Hokkaido, Japan, 35(6):1-7

[6] Barberi, F., Rosi, M., and Sodi, A., 1993, Volcanic hazard assesment at Stromboli based on review of hystorical data. Acta Volcanol. 3, 173-187.

[7] Bertagnini A., Coltelli M., Landi P., Pompilio M., and Rosi M., 1999, Violent explosions yield new insights into dynamics of Stromboli volcano. EOS Trans. AGU 80, 635-636.

[8] Bertagnini A., Métrich N., Francalanci L., Landi P., Tommasini S., and Conticelli S., 2009, Volcanology and Magma Geochemistry of the Present-Day Activity: Constraints aon the Feeding System. in The Stromboli Volcano: An Integrated Study of the 2002-2003 Eruption (eds S. Calvari, S. Inguaggiato, G. Puglisi, M. Ripepe and M. Rosi), American Geophysical Union, Washington

[9] Bertagnini A., Métrich N., Landi P., and Rosi M., 2003, Stromboli volcano (Aeolian Archipelago, Italy): an open window on the deep-feeding system of a steady state basaltic volcano. Journal of Geophysical Research, 108.

[10] Bonaccorso A., and Davis P.M., 1999 Models of ground deformation from vertical volcanic conduits with application to eruptions of Mount St. Helens and Mount Etna. Journal of Geophysical Research 104, 10531-10542.

[11] Burton M., Allard P., Mure' F., and La Spina A., 2007, Magmatic Gas Composition Reveals the Source Depth of Slug-Driven Strombolian Explosive Activity. Science, 317, 227-230.

[12] Burton M., Mader H.M., and Polacci M., 2007, The role of gas percolation in quiescent degassing of persistently active basaltic volcanoes. Earth and Planetary Science Letters, 264, 46-60.

[13] Calvari S., Bonaccorso A., Madonia P., Ner M., Liuzzo M., Salerno G.G., Behncke B., Caltabiano T., Cristaldi A., Giuffrida G., La Spina A., Marotta

E., Ricci T., Spampinato L., 2014, Major eruptive style changes induced by structural modifications of a shallow conduit system: The 2007-2012 Stromboli case. Bulletin of Volcanology, 76(7),1-15.

[14] Calvari S., Lodato L., Steffke A., Cristaldi A., Harris A.J.L., Spampinato L., and Boschi E., 2010, The 2007 Stromboli eruption: Event chronology and effusion rates using thermal infrared data. Journal of Geophysical Research, 115, B04201.

[15] Calvari S., Spampinato L., Bonaccorso A., Oppenheimer C., Rivalta E., and Boschi E., 2011, Lava effusion - A slow fuse for paroxysms at Stromboli volcano, Earth and Planetary Science Letters, 301, 317-333.

[16] Calvari S., Spampinato L., and Lodato L., 2006, The 5 April 2003 vulcanian paroxysmal explosion at Stromboli volcano (Italy) from field observations and thermal data. Journal of Volcanology and Geothermal Research, 140, 160-175.

[17] Casagli N., Tibaldi A., Merri A., Del Ventisette C., Apuani T., Guerri L., Fortuny-Guash J., and Tarchi D.,2009, Deformation of Stromboli volcano (Italy) during the 2007 eruption revealed by radar interferometry, numerical modeling and structural geological field data. Journal of Volcanology and Geothermal Research, 182(3-4), 182-200.

[18] Cashman, K. V., Sturtenvant, B., Papale, P., and Navon O., 2000, Magmatic fragmentation. In: Sigurdsson H et al. (eds) Encyclopedia of volcanoes. Academic Press, San Diego, pp 421-430.

[19] Chouet B., Hamesevicz N., ad McGetchin T.R., 1974, Photoballistics of volcanic jet activity at Stromboli, Italy. Journal of Geophysical Research, 79, 4961-4976.

[20] Chouet B., Dawson P., Ohminato T., Martini M., Saccorotti G., Giudicepietro F., De Luca G., Milana G., and Scarpa R., Source mechanisms of explosions at Stromboli Volcano, Italy, determined from moment-tensor inversions of very-long-period data. Journal of Geophysical Research, 108(B1), 2019.

[21] Colò L., Ripepe M., Baker D. R., and Polacci M., 2010, Magma vesiculation and infrasonic activity at Stromboli open conduit volcano, Earth and Planetary Science Letters, 292, 274?280.

[22] Cooper G.L., 1970, Development and use of a two-axis electrolytic bubble level as a precision vertical reference and tilt indicator, AIAA Paper, 70-949.

[23] Chouet, B., Dawson, P., Ohminato, T., Martini, M., Saccarotti, G., Giudiciepietro, F., De Luca, G., Milana, G., and Scarpa, R., 2003, Source mechanism of explosions at Stromboli Volcano, Italy, determined from moment-tensor inversions of very-long-period data. J. Geophys. Res. 108(B1).

[24] Coppola D., Campion R., Laiolo M., Cuoco E., Balagizi C., Ripepe M., Cigolini C., and Tedesco D., 2016, Birth of a lava lake,: Nyamulagira Volcano 2011-2015. Bulletin of Volcanology, 78(3), 1-13.

[25] Coppola D., Laiolo M., Barsotti C., Jonasdottir E., and Ripepe M., 2016, Effusion rates, volumes and emplacement style using MODIS MIR data: the 2014-15 Holuhraun eruption (Bardarbunga, Iceland) tracked by MIROVA. EGU General Assembly 2016 18 EGU2016-16308.

[26] Coppola D., Laiolo M., Cigolini C., Delle Donne D., and Ripepe M., 2015, Enhanced volcanic hot-spot detection using MODIS IR data: results from MIROVA system. In: Harris A.J.L., De Groeve T., Garel F., and Carn S.A. eds., Detecting, Modelling and Respomding to Effusive Eruptions. Geological Society of London, Special Publication, 426.

[27] Coppola D., Piscopo, D., Laiolo M., Cigolini C., Delle Donne D., and Ripepe M., 2012, Radiative heat power at Stromboli volcano during 2000-2011: Twelve years of MODIS observations. Journal of Volcanology and Geothermal Research, 215:48-60.

[28] Coppola D., Laiolo M., Delle Donne D., Ripepe M., and Cigolini C., 2014, Hot-Spot detection and characterization of Strombolian activity from MODIS infrared data. International Journal of Remote Sensing, 35(9), 3403-3426.

[29] Crocker, J. C., and Grier D. G., 1996, Methods of digital video microscopy for colloidal studies, J. Colloid Interface Sci., 179, 298.

[30] Delle Donne, D., and Ripepe M., 2012, High-frame rate thermal imagery of Strombolian explosions: implications for explosive and infrasonic source dynamics. J. Geophys. Res. Solid Earth, 117, pp. B09206-1-B09206-12

[31] De Fino M., La Volpe L., Falsaperla S., Frazzetta G., Neri G., Francalanci L., Rosi M., and Sbrana A., 1988, The Stromboli eruption of December 6, 1985 - April 25, 1986: Volcanological, petrological and seismological data. Rendiconto della Società Italiana di Mineralogia e Petrologia, 43, 1021-1038.

[32] Dzurisin D., 2007, Volcano Deformation - New geodetic monitoring techniques, Springer.

[33] Falsaperla S., and Schick, R., 1993, Geophysical studies on Stromboli volcano - a review. Acta Volcanologica, 1(7-8), 74-82.

[34] Fee, D., and Matoza R. S., 2013, An overview of volcano infrasound: From hawaiian to plinian, local to global, J. Volcanol. Geotherm. Res., 249, 123?139.

[35] Francalanci L., Davies G.R., Lustenhouwer W., Tommasini S., Mason P.R., and Conticelli S., 2005, Intra-grain Sr isotope evidence for crystal recycling and multiple magma reservoirs in the recent activity of Stromboli volcano, Southern Italy. Journal of Petrology, 46, 1997-2021.

[36] Francalanci L., Tommasini S., and Conticelli S., 2004, The volcanic activity of Stromboli in the 1906-1988 A.D. period: mineralogical, geochemical and isotope data relevant to the understanding of strombolian activity. Journal of Volcanology and Geothermal Research, 131, 179-211.

[37] Francalanci L., Tommasini S., Conticelli S., and Davies G.R., 1999, Sr isotope evidences for short magma residence time for the 2oth century activity of Stromboli volcano, Italy. Earth and Planetary Science Letters, 167, 61-69.

[38] Genco, R., and Ripepe, M., 2010, Inflation-Deflation cycles revealed by tilt and seismic records at Stromboli volcano, Gephysical Research Letters, 37, L12302.

[39] Genco R., Ripepe M., Marchetti E., Bonadonna C. and Biass S., 2014, Acoustic Wavefield and Mach Wave Radiation of Flashing Arcs in Strombolian Explosion Measured by Image Luminance. Geophysical Research Letters, DOI: 10.1002/2014GL061597.

[40] Goto, A., Ripepe M., and Lacanna G., 2014, Wideband acoustic records of the explosive volcanic eruptions at Stromboli: New insights on the explosive process and the acoustic source. Geophysical Research Letters, 41(11):3851-3857

[41] Graizer V.M., 2005, Effect of tilt on strong motion data processing. Soil Dynamics and Earthquake Engineering, 25, 197-204.

[42] Gudmundsson M.T., et al, 2016, Gradual caldera collapse at Bárdarbunga volcano, Iceland, regulated by lateral magma outflow. Science 353 (6296).

[43] Harris, A.J.L., 2013, Thermal Remote Sensing of Active Volcanoes: A User's Manual. Cambridge University Press.

[44] Harris, A. J. L., Delle Donne D., Dehn J., Ripepe M., and Worden A. K., 2013, Volcanic plume and bomb field masses from thermal infrared camera imagery, Earth Planet. Sci. Lett., 365, 77?85.

[45] Harris, A.J.L., and Ripepe, M., 2007, Synergy of multiple geophysical approaches to unravel explosive eruption conduit and source dynamics ? A case study from Stromboli. Chemie der Erde Geochemistry. 67, 1-35.

[46] Harris A.J.L., and Stevenson D.S., 1997, Magma budgets and steady-state activity of Vulcano and Stromboli volcanoes. Geophysical Rsearch Letters, 24, 1034-1046.

[47] Imbo' G., 1931, Parossismo di Stromboli nel settembre 1930. Bullettin Volcanologique, 3(1), 177-185.

[48] James M.R., Lane S.J., and Corder S.B., 2008, Modelling the rapid near-surface expansion of gas slugs in low viscosity magmas. In Lane S.J., Gilbert J.S., (Eds.), Fluid Motions in Volcanic Conduits: A source of Seismic and Acoustic Signals. Vol. 307 of Geological Society Special Publication of The Geological Society, 147-167.

[49] Jaupart C., and Vergniolle S., 1988, Laboratory models of Hawaiian and Strombolian eruptions. Nature, 331, 58-60.

[50] Jaupart C., and Vergniolle S., 1989, The generation and collapse of a foam layer at the roof of a basaltic magma chamber. Journal of Fluids Mechanics, 203, 347-380.

[51] J. B. Johnson, and Ripepe, M., 2011, Volcano infrasound: A review. J. Volcanol. Geothermal Res., 208, pp. 61-69.

[52] Kawaguchi R., and Nishimura T., 2015, Numerical investigation of temporal changes in volcanic deformation caused by a gas slug ascent in the conduit. Journal of Volcanology and Geothermal Research, 302, 1-10.

[53] Kinney, G. F., 1962, Explosive Shocks in Air. Mac Millan, London.

[54] Kirchdörfer M., Analysis and quasistatic FE modeling of long period impulsive events associated with explosions at Stromboli volcano (Italy), *Ann. Geofis.*, 42, 379-390, 1999.

[55] Koutsoukos E.Th., and Melis N.S., 2005, A Horizontal Component Broadband Seismic Sensor Based on an Inverted Pendulum. Bulletin of Seismological Society of America, 95, 2462-2471, 2005.

[56] La Felice S., and Landi P., 2011, The 2009 paroxysmal explosions at Stromboli (Italy): magma mixing and eruption dynamics. Bullettin of Volcanology.

[57] Landi P., Marchetti E., La Felice S., Ripepe M., and Rosi M., 2011, Integrated petrochemical and geophysical data reveals thermal distribution of the feeding conduits at Stromboli volcano, Italy. Geophysical Research Letters, 38,8,1-6.

[58] Levy, S., Velho L., Frery A. C., and Gomes J., 2009, Image Processing for Computer Graphics and Vision. p. 478, Springer Science and Business Media, New York.

[59] Livshits, L. D., and Bolkhovitinov L.G., 1977, Weak shock waves in the eruption column. Nature, 267, 420?422.

[60] Marchetti E., Genco R., and Ripepe M., 2009, Ground deformation and seismicity related to the propagation and drainage of the dyke feeding system during the 2007 effusive eruption at Stromboli volcano (Italy). Journal of Volcanology and Geothermal Research, 182(3-4):155-161

[61] Marchetti, E., and Ripepe, M., 2005, Stability of the seismic source during effusive and explosive activity at stromboli Volcano. Geophys. Res. Lett., 32, L03307.

[62] Marchetti, E., Ripepe M., Delle Donne D., Genco R., Finizola A., and Garaebiti E., 2013, Blast waves from violent explosive activity at Yasur Volcano, Vanuatu. Geophysical Research Letters, 40, 5838?5843.

[63] Marchetti E., Ripepe M., Harris A.J.L., and Delle Donne D., 2009, Tracing the differences between Vulcanian and Strombolian eruptions using infrasonic and thermal radiation energy. Earth and Planetary Science Letters, 279, 273-281.

[64] Marsella M., Proietti C., Sonnessa A., Coltelli M., Tommasi P., and Bernardo E., 2009, The evolution of the Sciara del Fuoco subaerial slope during the 2007 Stromboli eruption: Relation between deformation processes and effusive activity. Journal of Volcanology and Geothermal Research. 182(3-4), 201-213.

[65] Matoza, R. S., Fee D., Garces M. A., Seiner J. M., Ramon P. A., and Hedlin M. A. H., 2009, Infrasonic jet noise from volcanic eruptions. Geophysical Research Letters, 36, L08303

[66] Mattia M., Mattia, Rossi M., Guglielmino F., Aloisi M., and Bock Y., 2004, The shallow plumbing system of Stromboli Island as imaged from 1 Hz instantaneous GPS positions. Geophysical Research Letters, 31(24),1-4.

[67] Medici, E. F., Allen J. S., and Waite G. P., 2014, Modeling shock waves generated by explosive volcanic eruptions. Geophysical Research Letters, 41, 412-421.

[68] Métrich N., Bertagnini A., and Di Muro A., 2010, Conditions of magma storage, degassing and ascent at Stromboli: New insights into the volcano plumbing system with inferences on the eruptive dynamics. Journal of Petrology, 51, 603-626.

[69] Métrich N., Bertagnini A., Landi P., and Rosi M., 2001, Crystallization driven by decompression and water loss at Stromboli volcano (Aeolian Islands, Italy): Journal of Petrology, 42, 1471-1490.

[70] Miller W.F., Geller R.J., and Stein S., 1978, Use of a bubble tiltmeter as a horizontal seismometer, Geophysical Journal of Royal Astronomical Society, 54, 661-668.

[71] Nairn, I. A., 1976, Atmospheric shock waves and condensation clouds from Ngauruhoe explosion eruption. Nature, 259, 190?192.

[72] Neuberg, J., Luckett R., Ripepe M., and Braun T., 1994, Highlights from a seismic broad-band array on Stromboli volcano. Geophysical Research Letters, 21(9),749-752.

[73] Nichols, J. W., and Lele S. K., 2012, Large eddy simulation of crackle noise in supersonic jets. in Center for Turbulence Research Annual Research Briefs (Conf. Proceeding).

[74] Nishimura T., 2006, Ground deformation due to magma ascent with and without degassing, Geophysical Research Letters, 33(23),6-9.

[75] Nishimura T., 2009, Ground deformation caused by magma ascent in an open conduit. Journal of Volcanology and Geothermal Research, 187(3-4),178-192.

[76] Nishimura T., Iguchi M., Hendrasto M., Aoyama H., Yamada T., Ripepe M., and Genco R., 2016, Magnitude?frequency distribution of volcanic explosion earthquakes. Earth, Planets and Space, 68-1, 125.

[77] Oertel H., 1978, Kinematics of Mach waves inside and outside supersonic jets. ISL Report PU 302/78.

[78] Parfitt E.A., 2004, A discussion on the mechanism of explosive basaltic eruptions. Journal of Volcanology and Geothermal Research, 134, 77-107.

[79] Parfitt E.A., and Wilson L., 1995, Explosive volcanic eruptions: IX. The transition between Hawaiian-style lava fountaining and strombolian explosive activity. Geophysical Journal International, 121, 226-232.

[80] Patrick M.R., Anderson K.R., Poland M.P., Orr T., and Swanson D.A., 2015, Lava lake level as a gauge of magma reservoir pressure and eruptive hazard. Geology, 43, 831-834.

[81] Patrick M.R., Harris A.J.L., Ripepe M., Dehn J., Rothery D., and Calvari S., 2006, Strombolian explosive styles and source conditions, insights from thermal (FLIR) video. Bullettin of Volcanology.

[82] Perret A.F., 1912, The flashing arcs: A volcanic phenomenon. American Journal of Sciences, 4, 329?333.

[83] Perret, A.F., 1916, The lava eruption of Stromboli summer?autumn, 1915. American Journal of Science, 42, 436?457.

[84] Pino, N. A., Moretti R., Allard P., and Boschi E., 2011, Seismic precursors of a basaltic paroxysmal explosion track deep gas accumulation and slug upraise. Journal of Geophysical Research: Solid Earth, 116,2,1-13.

[85] Pioli L., Azzopardi B.J., Cashman K.V., 2009, Controls on the explosivity of scoria cone eruptions: Magma segregation at conduit junctions. Journal of Volcanology and Geothermal Research, 186, 407-415.

[86] Pioli L., Pistolesi M., and Rosi M., 2014, Transient explosions at open-vent volcanoes: the case of Stromboli (Italy). Geology, 42(10), 863-866.

[87] Pistolesi M., Delle Donne D., Pioli L., Rosi M., and Ripepe M., 2011, The 15 March 2007 explosive crisis at Stromboli volcano, Italy: Assessing physical parameters through a multidisciplinary approach. Journal of Geophysical Research, 116, B12206.

[88] Ripepe M., 1996, Evidence for gas influence on volcanic seismic signals recorded at Stromboli. Journal of Volcanology and Geothermal Research, 70(3-4):221:233

[89] Ripepe M., and Braun T., 1994, Air-wave phases in strombolian explosion-quake seimsograms: a possible indicator for the magma level? Acta Vulcanologica, 5, 201-206.

[90] Ripepe, M., Ciliberto, S., and Della Schiava, M., 2001, Time constraints for modeling source dynamics of volcanic explosions at Stromboli. J. Geophys. Res., 106, 8713-8727.

[91] Ripepe M., Delle Donne D., Genco R., Maggio G., Pistolesi M., Marchetti E., Lacanna G., Ulivieri G., and Poggi P., 2015, Volcano Seismicity and ground deformation unveil the gravity-driven magma discharge dynamics of a volcanic eruption. Nature Communications.

[92] Ripepe, M., Delle Donne D., Harris A.J.L., Marchetti M., and Ulivieri G., 2008, Dynamics of strombolian activity, in The Stromboli Volcano. An Integrated Study of 2002-2003 Eruption, Geophysical Monography Series, vol. 182, edited by S. Calvari et al., pp. 39?48, AGU, Washington, D. C.

[93] Ripepe M., Delle Donne D., Lacanna G., Marchetti E., and Ulivieri G., 2009, The onset of the 2007 Stromboli effusive eruption recorded by an integrated geophysical network, Journal of Volcanology and Geothermal Research, 182(3-4):131-136.

[94] Ripepe M., and Gordeev E., 1999, Gas bubble dynamics model for shallow volcanic tremor at Stromboli. Journal of Geophysical Research - Solid Earth, 104(B5):10639-10654.

[95] Ripepe M., Harris A.J.L., and Marchetti E., 2005, Coupled thermal oscillations in explosive activity at different craters of Stromboli volcano. Geophysical Research Letters, 32(17).

[96] Ripepe M., and Marchetti E., 2002, Array tracking of infrasonic sources at Stromboli volcano. Geophysical Research Letters, 29(22).

[97] Ripepe M., Marchetti E., and Ulivieri G., 2007, Infrasonic monitoring at Stromboli volcano during the 2003 effusive eruption: Insights on the explosive and degassing process of an open conduit system. Journal of Geophysical Research - Solid Earth, 112(B9).

[98] Ripepe M., Marchetti E., Ulivieri G., Harris A.J.L., Dehn J., Burton M., Caltabiano T., and Salerno G., 2005, Effusive to explosive transition during the 2003 eruption of Stromboli volcano. Geology, 33(5): 341-344-

[99] Ripepe M., Rossi M., Saccorotti G., 1993, Image analysis of the dynamical behaviour at Stromboli, Journal of Volcanology and Geothermal Research, 54, 335-351.

[100] Ripepe M., Poggi P., Marchetti E., 2004, Small aperture infrasonic array monitors activity of Stromboli volcano. Inframatics, 7,1-15.

[101] Rodgers P., 1968, The response of the horizontal pendulum seismometer to Rayleigh and Love waves, tilt, and free oscillations of the earth, Bulletin of Seismological Society of America, 58(5):1385-1406.

[102] Rose W.I., Palma J.L., Delgado Granados H., and Varley N., 2013, Open-vent volcanism and related hazards: Overview. in Rose et al., eds., Understanding Open-Vent Volcanism and Related Hazard. Geological Society of America Special Paper, 498, vii-xiii.

[103] Rosi M., Bertagnini A., Harris A.J.L., Pioli L., Pistolesi M., and Ripepe M., 2006, A case history of paroxysmal explosion at Stromboli: timing and dynamics of the April 5, 2003 event. Earth and Planetary Science Letters, 243(3-4), 594-606.

[104] Rosi M, Pistolesi M., Bertagnini A., Landi P., Pompilio M., and Di Roberto A., 2013, Stromboli volcano, Aeolian Islands (Italy), in Lucchi, F., et al., eds., The Aeolian Islands Volcanoes: Present eruptive activity and hazards. Geological Society of London Memoir 37,473-490.

[105] Scandone, R., and Giacomelli, L., 1998, Vulcanologia. Principi fisici e metodi d'indagine, Napoli, Liguori Editore.

[106] Spampinato L., Calvari S., Harris A.J.L., and Dehn J., 2008, Evolution of the Lava Flow Field by Daily Thermal and Visible Airborne Surveys, in The Stromboli Volcano: An Integrated Study of the 2002-2003 Eruption (eds S. Calvari, S. Inguaggiato, G. Puglisi, M. Ripepe and M. Rosi), American Geophysical Union, Washington, D. C.

[107] Taddeucci J., Scarlato P., Capponi A., Del Bello E., Cimarelli C., Palladino D. M., and Kueppers U., 2012, High-speed imaging of Strombolian explosions: The ejection velocity of pyroclasts. Geophysical Research Letters, 39, L02301,

[108] Tam C. K. W., 2009, Mach wave radiation from high-speed jets. AIAA Journal, 47, 2440?2448.

[109] Tommasi P., Baldi P., Chiocci F.L., Coltelli M., Marsella M., and Romagnoli C., 2008, Slope Failures Induced by the December 2002 Eruption at Stromboli Volcano, in The Stromboli Volcano: An Integrated Study of the 2002-2003 Eruption (eds S. Calvari, S. Inguaggiato, G. Puglisi, M. Ripepe and M. Rosi), American Geophysical Union, Washington.

[110] Ulivieri G., 2008, Dynamic model of the continuous degassing of the shallow magmatic column at Stromboli volcano as inferred by infrasonic data. PhD dissertation, Department of Earth Sciences, University of Firenze, Italy.

[111] Valade S., Lacanna G., Coppola D., Laiolo M., Pistolesi M., Delle Donne D., Genco R., Marchetti E., Ulivieri G., Allocca C., Cigolini C., Nishimura T., Poggi P., and Ripepe M., 2016, Tracking dynamics of magma migration in open-conduit systems. Bullettin of Volcanology.

[112] Vergniolle S., and Brandeis G., 1994, Origin of a sound generated by strombolian explosion. Geophysical Research Letters, Vol. 21, 18, pp.1959-1962.

[113] Vergiolle S., and Brandeis G., 1996, Strombolian explosions: a large bubble breaking at the surface af a lava column as a source of sound. Journal of Geophysical Research, 101(B9), 20433-20447.

[114] Wiens D.A., Pozgay S.H., Shore P.J., Sauter A.W., and White R.A., 2005, Tilt recorded by a portable broadband seismograph: The 2003 eruption of Anatahan Volcano, Mariana Islands, Geophysical Research Letters, 32.

[115] Wielandt E., and T. Forbriger, Near-field seismic displacement and tilt associated with the explosive activity of Stromboli, *Ann. Geofis.*, 42, 407-416, 1999.

[116] Wilson L., 1980, Relationships between pressure, volatile content and ejecta velocity in three types of volcanic explosion. Journal of Volcanology and Geothermal Research, 8, 297-313.

[117] Wilson L., Self S., 1980, Volcanic explosions clouds: density, temperature, and particle content estimates from cloud motion. Journal of Geophysical research, 85(B5),2567-2572.

[118] Wooster, M.J., Shukiv B., and Oertel D., 2003, Fire radiative energy for quantitative study of biomass burning: Derivation from the BIRD experimental satellite and comparison to MODIS fire products. Remote Sensing of Environment, 86,1,83-107.

[119] Yokoo A., and Ishihara K., 2007, Analysis of pressure waves observed in Sakurajima eruption movies. Earth Planets and Space, 59, 177?181.

[120] Yokoo, A., and Taniguchi H., 2004, Application of video image processing to detect volcanic pressure waves: A case study on image archives of Aso Volcano, Japan. Geophysiscal Research Letters, 31, L20604,

[121] Zobin, V.M., 2003, Introduction to volcanic seismology. Developments in Volcanology 6, Elsevier.